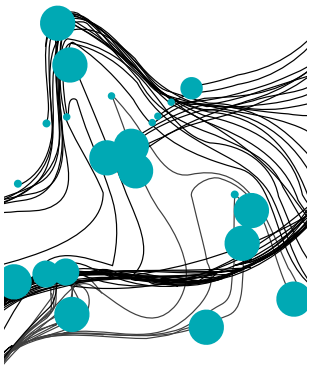

Master Applied Physics
Master Biomedical Engineering

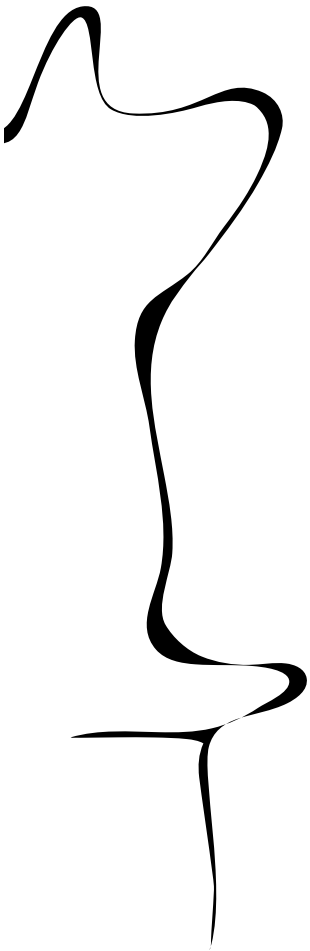

Master Assignment Report

Investigating the Role of 14-3-3 Proteins in Multiple Stages of Multimerization and Aggregation of α-Synuclein

Christel G. Heidema

Graduation Committee:
prof. dr. Mireille M. A. E. Claessens
dr. Christian Blum
prof. dr. Michel Versluis
Gobert Heesink MSc

May 2024 - July 2025

Nanobiophysics
Faculty of TNW
University of Twente

Contents

Abstract

Parkinson's disease, a neurodegenerative disorder, is associated with the aggregation of the intrinsically disordered protein α-synuclein (αS). A family of proteins known as 14-3-3 chaperones, which are part of the cellular protein quality control system, have shown an inhibiting role in aggregation of αS. However, the way in which these chaperones interact with αS remains poorly understood.

This study investigates both the early multimerization stages of α-synuclein and the later fibrillar stages of αS aggregation, focusing on interactions with 14-3-3 at these different stages. Using Microscale Thermophoresis (MST) measurements, this study demonstrates that αS multimerizes in early stage through a cooperative mechanism. This study revealed that electrostatic interactions and hydrogen bonds play a crucial role in early αS multimerization. The τ, γ, and σ isoforms of 14-3-3 all affect this early αS multimerization, overall resulting in a decrease in cooperativity. This may indicate the formation of mixed multimers of αS and 14-3-3 through a non-cooperative process. These mixed multimers do not form amyloid fibrils and compete with the formation of fibrils from αS-only multimers. Using the techniques Microscale Thermophoresis (MST) and Fluorescence Correlation Spectroscopy (FCS), indications for interaction between αS 30-mers and 14-3-3τ were found. In combination with the MST results of early multimerization, this indicates that 14-3-3τ does not interact with a specific αS multimer or size, but rather exhibits a more general interaction. Additionally, colocalization in confocal imaging and MST experiment suggest that 14-3-3τ binds to αS fibrils.

These insights enhance the understanding of how 14-3-3 proteins modulate αS aggregation and may support the development of new therapeutic approaches for Parkinson's disease.

Keywords: α-synuclein aggregation, amyloid fibrils, 14-3-3 chaperones, confocal imaging, cooperativity, early multimerization, fluorescence correlation spectroscopy, microscale thermophoresis, nucleation-elongation, α-synuclein oligomers, protein-protein interactions, widefield fluorescence microscopy

Chapter 1

Introduction

Neurodegenerative diseases are increasing in incidence [1]. There are several neurodegenerative diseases which are associated with aggregation of amyloidogenic proteins. One of them is Parkinson's disease [2]. In this disease, the protein α-synuclein (αS) plays an important role. This protein is an intrinsically disordered protein (IDP), which means it lacks a fixed three-dimensional structure in solution. Mutations, aging or other environmental factors may lead to the misfolding and aggregation of fibrils of this protein [3]. After the formation of the first aggregates, the aggregates themselves will catalyze further aggregation. This aggregation behavior will propagate across cells [4][5]. The aggregation will cause a cascade of toxic events, such as disrupted synaptic-vesicle trafficking, impaired mitochondrial function, and the disruption of multiple endoplasmic reticulum (ER) functions [5]. Ultimately, this leads to cell death resulting in symptoms of the disease.
When proteins are expressed, various processes ensure that the proteins are folded correctly and remain in their properly folded state. These processes are governed by chaperone proteins [6]. The system of chaperone proteins is collectively referred to as the Protein Quality Control (PQC) system. It supports correct protein folding and prevents aggregate formation of misfolded proteins.
It is well known that certain chaperone proteins delay or prevent harmful protein aggregation. This may also be the case for the IDP αS in Parkinson's disease. However, the mechanistic details remain poorly understood.
This project investigates the mechanisms by which chaperones interact with αS proteins and prevent aggregate formation, using reconstituted systems. The focus lies on the aggregation of α-synuclein (αS) in Parkinson's disease (PD), applying techniques such as microscale thermophoresis (MST) and fluorescence correlation spectroscopy (FCS) to observe multimerization events. Recent findings at the Nanobiophysics (NBP) research group have shown that the chaperone 14-3-3τ changes the first steps in α-synuclein aggregation, the multimerization of α-synuclein [7]. This research will be extended to different isoforms of 14-3-3. Next to that, interactions between various forms of αS-forms (monomers, oligomers, and fibrils) and 14-3-3-τ will be explored. This approach aims to provide deeper insight in how 14-3-3 chaperones interact with aggregating proteins and the physical mechanisms by which they influence, delay or counteract the aggregation process.

1.1 Research Goals

The main objective of this research is to gain insight in the interaction between 14-3-3 chaperones and the αS protein, and the potential roles these interactions play in preventing aggregate formation. This objective is supported by the following sub-goals:

1. **Gaining insight in the early-phase αS multimerization process.** Knowing the characteristics of the αS multimerization process is essential in order to determine how 14-3-3 can influence this process.

2. **Investigating the molecular basis of αS multimerization (i.e., type of interactions involved).** Identifying the molecular interactions involved in αS multimerization is important for understanding how 14-3-3 chaperones interact with αS.

3. **Examining how the 14-3-3 chaperone affects the early stages of αS aggregation, the multimerization of αS synuclein.** It is important to determine at which stage(s) 14-3-3 interacts with αS. Specifically, understanding whether 14-3-3 plays a role in early multimerization could reveal how it helps prevent the formation of toxic fibrils.

4. **Studying the interaction between 14-3-3τ and αS oligomers (e.g., 30-mers).** Investigating whether 14-3-3 interacts with αS oligomers is important for understanding the stage-specific roles of the chaperone.

5. **Investigating the interaction between 14-3-3τ and αS fibrils.** It is of relevance to know whether 14-3-3τ interacts with fibrils to determine whether 14-3-3 chaperones can affect fibrils.

6. **Exploring the self-multimerization behavior of 14-3-3τ.** The self-multimerization of 14-3-3 tau could impact the interactions described in sub-goals 3, 4, and 5. Understanding this behavior is essential for the correct interpretation of the experimental outcomes.

Chapter 2

Background and Theory

2.1 α-Synuclein Protein

αS is a highly abundant neuronal protein that is particularly concentrated in presynaptic nerve terminals [8]. It is especially enriched in the hippocampus, neocortex, thalamus, striatum and cerebellum compared to other brain regions. Misfolded oligomers and larger aggregates of alpha-synuclein accumulate in several neurodegenerative disorders collectively known as synucleinopathies. Despite their clinical significance, the mechanisms by which alpha-synuclein contributes to neurodegeneration are still not fully understood. In addition, the earliest stages of αS aggregation and the mechanisms that prevent aggregation are still not fully known [9]. Furthermore, the physiological role of αS within cells remains a topic of ongoing investigation. For example, roles of αS are found in neurotransmitter release and synaptic plasticity, vesicle trafficking, dopamine synthesis and transport, and lipid transport. To provide a deeper understanding of the αS protein, this section outlines background information on the structure, multimerization mechanism, and aggregation of αS.

2.1.1 Structure

The αS protein has a length of 140 amino acids and carries a net negative charge, classifying it as an acidic protein. In solution, it behaves as an intrinsically disordered protein (IDP), meaning it lacks a stable structure under physiological conditions. Its conformation is partially dependent on its surroundings. For instance, αS is unfolded when in the cytosol and has an α-helical structure when bound to phospholipids [10]. This environment-dependent behavior suggests that αS serves different functional roles in various parts of the cell. In particular, αS plays a role in promoting membrane curvature, which aids in synaptic trafficking and vesicle budding [11].

The αS protein can be divided into three domains.
Firstly, there is the positively charged N-terminal domain (residues 1-60), which consists of a lipid-binding α-helix. This domain has 7 series of 11-amino-acid repeats, which play an important role in interactions between αS and lipids by inducing a helical structure in αS and consequently reducing the change of forming β-structures. This domain is associated with membrane binding [12].
Secondly, the central domain (residues 61-95), known as the amyloid-binding domain (NAC), is highly hydrophobic and capable of forming cross β-structures. Therefore, this domain is associated with protein aggregation and fibril formation[10].
Lastly, there is the C-terminal acidic tail (residues 96-140). This part of the protein chain

can adapt a random coil structure in certain environments due to its low hydrophobicity and relatively high negative net charge. This domain is rich in proline residues, which contribute to the flexibility of the protein chain [12].
It is believed that interactions between the C-terminal domain and the NAC domain hinder aggregation [10]. This effect is likely due to the charge properties of the C-terminal domain, as the addition of Al^{3+} ions, which bind to this region, can promote aggregation. Additionally, the negatively charged residues of the C-terminal domain can interact with the positively charged residues of the N-terminal domain in certain surroundings. In this way a closed αS conformational state is formed. These long-range interactions are thought to inhibit the spontaneous oligomerization and aggregation of αS [13][14].
Furthermore, the role of phosphorylation of serine residue 129 remains a topic of ongoing debate [15]. Some studies report that phosphorylation of serine residue 129 can cause an acceleration in neuronal cell death[16][17], while other studies suggest that it can have an inhibiting role on αS fibril formation and seeded aggregation[18][19].

2.1.2 Aggregation of α-Synuclein

αS aggregation into amyloid fibrils is associated with loss of its normal function and is implicated in neurodegenerative diseases. These fibrils deposit primarily in the human brain. αS normally has high expression levels in regions such as the neocortex, hippocampus, substantia nigra, thalamus, and cerebellum. Under pathological conditions, it accumulates and aggregates into fibrils that form Lewy bodies (LBs) [10]. αS monomers can assemble into multimers. Some of these multimers form a critical nucleus for amyloid formation, resulting in amyloid fibril formation [7]. This process is summarized in figure 2.1. The fibril structures are self-assembled protein structures. αS forms a cross-β structure, where extended β-sheets are aligned along the length of the fibril and individual β-strands are oriented perpendicular to the fibril axis [20]. When these fibrils are formed, they will catalyze further aggregation. In this way, it initiates a toxic cascade.

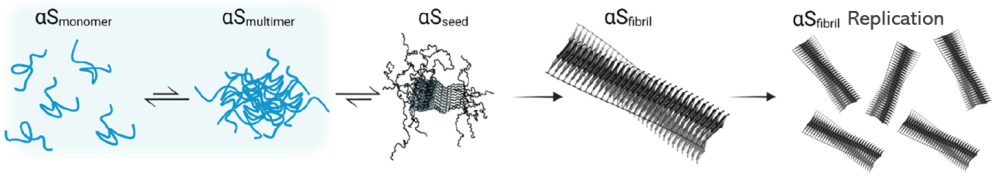

FIGURE 2.1: Schematic of αS fibril formation. Adapted from [7].

2.1.3 Nucleation-Elongation Mechanism

The nucleation-elongation chain growth mechanism plays a significant role in the multimerization of αS. Recent research at NBP has shown that αS starts forming dynamic multimers at a particular critical concentration [7]. The nucleation-elongation mechanism is especially relevant in the context of supramolecular assemblies and polymers that are supramolecularly structured. In polymer chemistry, commonly known mechanisms for chain growth include step-growth, addition, and living polymerization. Nucleation-elongation represents an alternative mode of chain growth, distinct from these classical mechanisms.
This mechanism not only plays a role in amyloid aggregation but is also responsible for the formation of multimers from monomers in the earliest stages. Since the early stage of multimerization is a key point of interest in this study, the mechanism is discussed from

this perspective. The reaction begins with a energetically unfavored event, the nucleation. Once nucleation occurs, small oligomers such as dimers and trimers are formed. From there, the process proceeds to the elongation phase, which is an energetically favored step [21] (figure 2.2).

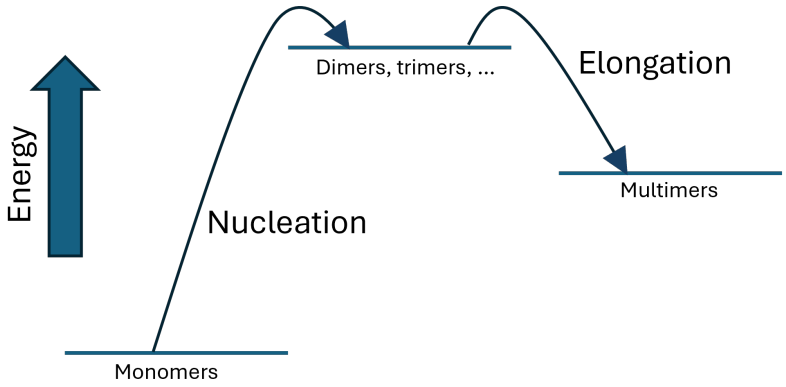

FIGURE 2.2: Schematic depicting the energy landscape associated with multimerization through the nucleation-elongation mechanism. This diagram illustrates how single monomers form oligomers, which can further evolve into multimers, highlighting the energy levels during the early stages of the multimerization process.

When the elongation step is significantly more favorable than the nucleation step, the process is referred to as cooperative. The level of cooperativity can be described using a cooperativity factor σ, which is described as $\sigma = K_N/K$, where K_N is called the equilibrium constant for nucleus formation (in early multimerization), and K is the equilibrium constant of any monomer addition step. When only a single step is involved, N is 2. If $\sigma \ll 1$, meaning $K_N \ll K$, the process is highly cooperative, whereas if $\sigma \sim 1$, the process is non-cooperative. In such cooperative processes, there exists a critical concentration (c_c) above which only the multimer concentrations increases, while the monomer concentration remains constant at a value of $c_c = K^{-1}$. This critical concentration, assuming a single nucleation step, can be described using a nucleation self-assembly model [21]:

$$c_t = (1-\sigma)[A] + \frac{\sigma[A]}{(1-K[A])^2} \tag{2.1}$$

Here, K is c_c^{-1}, c_t is the initial total monomer concentration, and [A] represents the total monomer concentration.
To better understand the difference between cooperative and non-cooperative processes, a plot of the ratio between the total monomer concentration and the initial total monomer concentration, $[A]/c_t$, as a function of Kc_t can be used. Kc_t is chosen instead of c_t in order to generalize the model. The monomer fraction can be interpreted relatively. It represents the distribution between two equilibrium states. Figure 2.3 shows an example plot for $[A]/c_t$ as a function of Kc_t, highlighting two degrees of cooperativity. In the highly cooperative case, $[A]/c_t$ remains constant until it drops at a well-defined critical concentration. In contrast, the less cooperative case shows a more gradual decrease in $[A]/c_t$ lacking a distinct critical concentration. The curve is smoother and has a less steep slope.

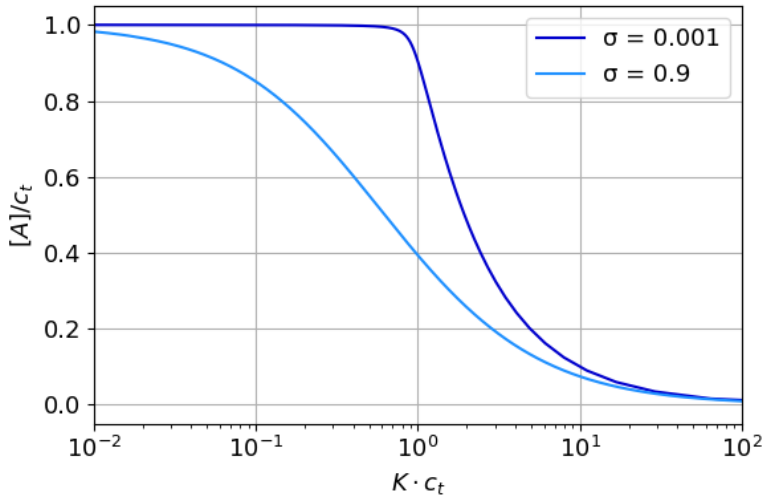

FIGURE 2.3: Plot of $[A]/c_t$ as a function of Kc_t according to the nucleation-elongation model for two values of σ. The value of $\sigma = 0.001$ corresponds to a highly cooperative process, whereas $\sigma = 0.9$ indicates no cooperativity.

2.2 Protein Quality Control (PQC) System

Not only αS is at constant risk of misfolding and aggregating, but many other proteins are. To prevent this, various processes ensure that proteins fold correctly and remain in their properly folded state [22]. This entire system of processes is referred to as the Protein Quality Control (PQC) system. A large part of these processes is governed by chaperone proteins. Some chaperone systems are known for their interaction with αS, such as the HSP70 chaperone system and the 14-3-3 chaperone family.

2.2.1 HSP70 Chaperone System

This system can disaggregate amyloid fibrils. However, during the disaggregation process, fibril fragments can be released. These fibril fragments may act as critical nuclei, promoting further aggregation in amyloid fibrils. In this way, the opposite of the desired effect can occur. Additionally, HSP70 requires a significant amount of ATP to disaggregate fibrils [23], indicating disaggregation is an energetically disfavored process, whereas aggregation is energetically favored, leading to the formation of new fibrils. For these reasons, this chaperone system is probably not intended as primary mechanism for preventing aggregation, but rather serves as a backup strategy [24].

2.2.2 14-3-3 Proteins

Since the HSP70 system functions more a backup mechanism, there is likely another mechanism that acts during the early stages of multimerization, one that does not lead to amyloid fibril formation and is more energetically favorable. The 14-3-3 protein family is suspected to have this function. The 14-3-3 protein family consists of seven human isoforms, which are β, γ, ε, τ, η, σ, and ζ [25]. These proteins are highly conserved and serve as important regulatory proteins that help control many processes in the cell by interacting with a large variety of other proteins [26].

14-3-3 proteins form both homo- and heterodimers and recognize phosphorylated motifs in flexible regions of their target proteins using a conserved amphipathic binding groove [26]. However, interactions that are not phosphorylation-dependent have also been observed [27]. The last two α-helices on the C-terminal additionally contribute in interactions [25]. Important interaction partners of 14-3-3 are related to neurodegenerative diseases, like Alzheimer disease and Creutzfeldt-Jakob Disease [28].
Reduced expression of 14-3-3 is often associated with the harmful protein aggregation that is a characteristic of various neurodegenerative diseases. 14-3-3 proteins have also been found in various aggregates associated with these diseases and it has been shown that 14-3-3 proteins can prevent aggregation in vitro, like shown for [29] and [30]. This points to a chaperone-like role for 14-3-3 chaperones in the prevention of protein aggregation [26].
An interesting example of such a chaperone-like role is the impact of 14-3-3τ on early formation of nanoscale αS condensates. Instead of forming αS-only condensates through a cooperative mechanism, αS and 14-3-3τ form mixed condensates through a non-cooperative mechanism. The shift from a cooperative to a non-cooperative mechanism result in the formation of more condensates, but they are smaller in size. The formation of these co-condensates competes with the formation of αS-only condensates, thereby reducing the likelihood of αS forming amyloid fibrils. The proposed multimerization mechanism in the presence of 14-3-3τ is summarized in figure 2.4.

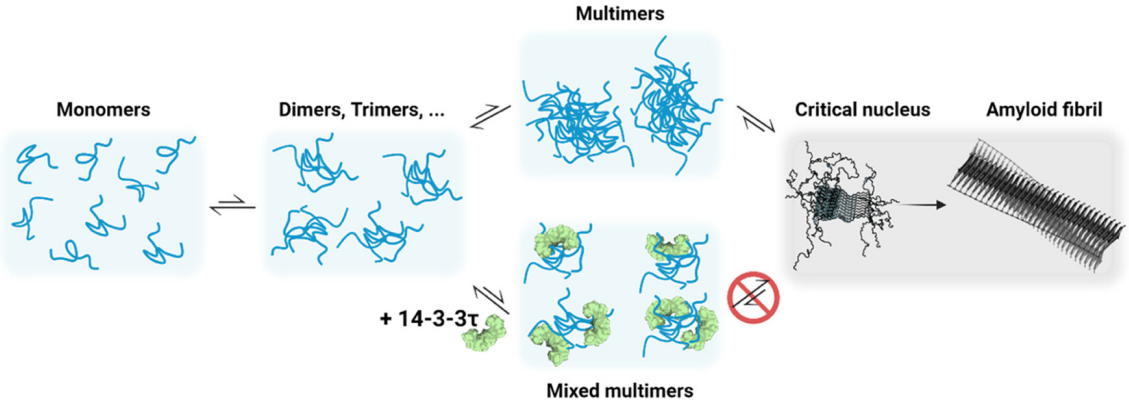

FIGURE 2.4: Schematic of αS fibril formation in the presence of the 14-3-3τ chaperone. Note that mixed multimers do not form into critical nulei. Figure from [7].

More generally, it is hypothesized that the effects of chaperones on protein aggregation are determined by the energy barriers between the monomeric and aggregated forms of the proteins, and by how chaperones can create alternative pathways with different energy barriers. Chaperones can form co-aggregates when the reduction in their chemical potential within the co-aggregate, compared to the monomeric state, exceeds the increase in chemical potential of the co-aggregates relative to peptide-only aggregates. In other words, the chaperone is "unhappy" on its own. In this way, co-aggregate formation can suppress homomolecular aggregate formation [31]. In the case of 14-3-3, it is not known whether this chaperone behaves as an "unhappy" chaperone, but its behavior may possibly be explained in this way.

2.3 Techniques

2.3.1 Microscale Thermophoresis (MST)

Microscale Thermophoresis (MST) is a perturbation-based technique. An equilibrium of interacting species (such as monomer-to-multimer interactions or ligand-target binding) is perturbed by introducing a heated region, produced by an IR laser diode [32]. The target molecules are fluorescently labeled, and their fluorescence signal is tracked over time following the perturbation. Signal recording starts under unperturbed conditions. After a few seconds, the IR laser is switched on. Fluorescence intensity typically drops, levels and raises again during the recovery phase when the IR laser is turned off. The resulting fluorescence signal over time is normalized and is called F_{norm}. Typically, the fluorescence intensity response before laser activation is compared to the intensity at a specific time point or interval after laser activation. This difference is referred to as ΔF_{norm} and is usually expressed in ‰. An example of a fluorescence intensity response is given in Figure 2.5 (top).

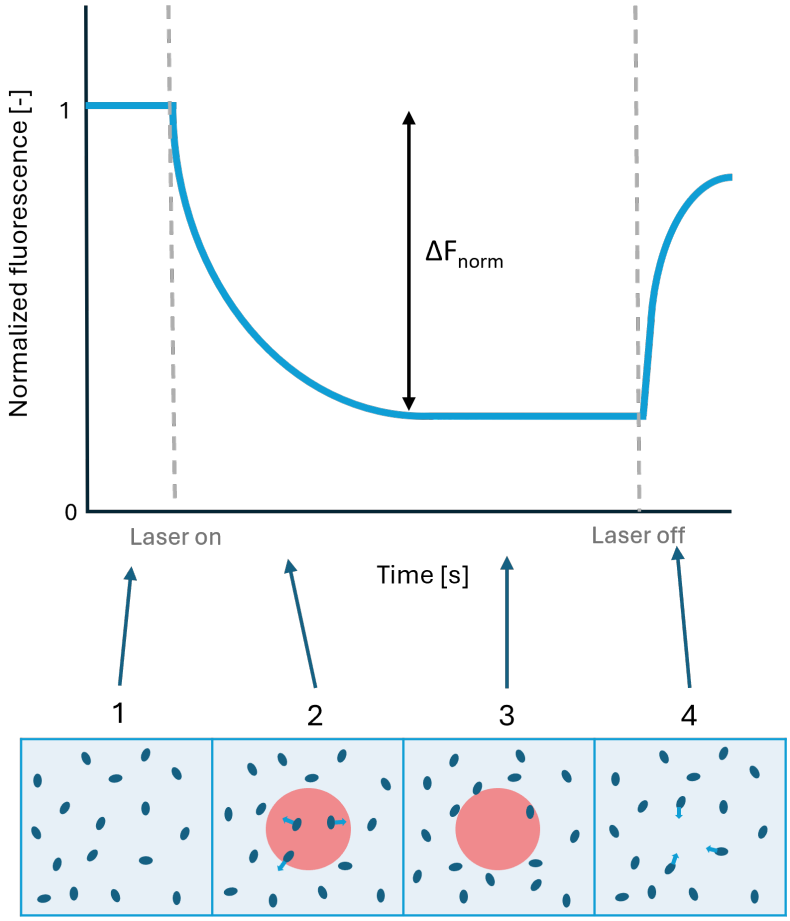

FIGURE 2.5: Example of a typical MST curve (top) with corresponding movement of particles as response on a temperature gradient (bottom).

There are several effects induced by a temperature gradient. Immediately after turning on the laser, a T-jump occurs, which is a short time interval during which the laser heats the sample and forms a temperature profile (on a sub-second timescale). The temperature rise in this phase occurs much faster than molecular diffusion. Therefore, during the T-jump,

the observed response is primarily influenced by the dye's intrinsic temperature sensitivity and only minimally influenced by thermal diffusion. The expected decrease in absolute fluorescence is given by $\frac{\partial F_A}{\partial T}$, which denotes the rate of change in fluorescence with respect to temperature [32]. The temperature sensitivity of the dye depends on the molecule(s) to which it is bound. This can result in an altered response when a labeled ligand molecule is bound to a target molecule.
After the introduction of a temperature gradient, the movement of particles is changed due to thermal diffusion. An example is shown in figure 2.5 (bottom). This temperature-dependent motion is characterized by the thermal diffusion coefficient D_T. In a dynamic equilibrium, thermal diffusion is balanced by mass diffusion, described by the diffusion coefficient D. The ratio of these two characterizes the behavior of the sample in a dynamic equilibrium [32], during which the fluorescence intensity remains constant (figure 2.5). This ratio, $S_T = \frac{D_T}{D}$, is called the Soret coefficient, and has a high sensitivity for small differences at the molecular surface. It can be described as [33]:

$$S_T = \frac{A}{kT}(-\Delta s_{hyd}(T) + \frac{\beta\sigma_{eff}^2}{4\varepsilon\varepsilon_0} \cdot \lambda_{DH}) \tag{2.2}$$

Here, A is the particle surface area, $\Delta s_{hyd}(T)$ is the surface entropy, σ_{eff} is the net charge, ε_0 is the vacuum permittivity, ε is the dielectric coefficient, and λ_{DH} is the Debye length. An essential aspect of the thermophoretic effect is the creation of an electrochemical gradient by all molecules present in the sample (such as ions and buffer components) within which the behavior of the fluorescently labeled molecules is observed [34]. Different particles have different Soret coefficients, and this difference is what allows us to distinguish between bound and unbound ligands. These differences result in different F_{norm} values, which are measured with MST. MST is typically used to study protein-ligand interactions. However, the method is also well-suited for measuring multimerization. This is particularly useful for studying early stages of αS aggregation and potential interference of chaperone proteins such as 14-3-3.
By performing repeated measurements of ΔF_{norm} value for varying protein concentrations, a binding curve can be obtained. An example of a binding curve for multimerization is given in figure 2.6. This binding curve shows two plateaus; the initial plateau corresponds to a state with monomers only, while the second plateau represents a state in which both monomers and multimers are present.

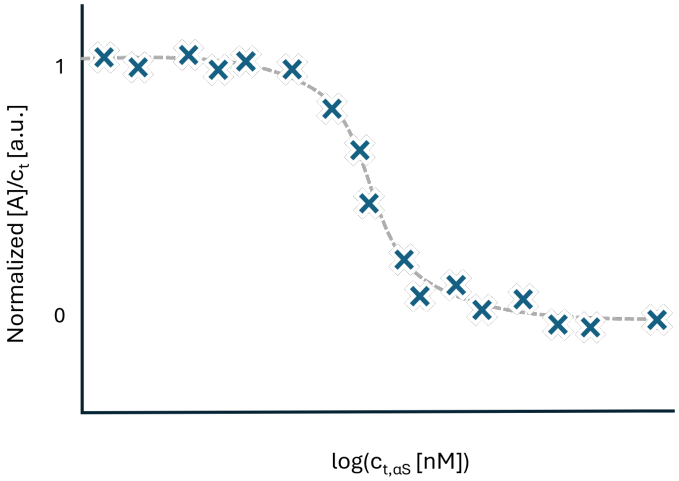

FIGURE 2.6: Example of a MST multimerization curve where F_{norm} is shown for different particle concentrations. Here, there are two states. For low concentrations there are no interactions, but there are interactions for higher concentrations.

2.3.2 Fluorescence Correlation Spectroscopy (FCS)

Fluorescence Correlation Spectroscopy (FCS) is a technique for determining the diffusion, mobility, concentration, and interactions of biomolecules. The method is based on fluctuations in fluorescence intensity over time within a confocal volume. Particles can move due to Brownian motion or follow a Poisson process in the case of a chemical reaction [35]. When the concentration of fluorescently labeled molecules in solution is high, many labeled molecules will diffuse in and out of the confocal volume over a given period. As a result, the fluorescence intensity, shows continuous lower amplitude variations and appears more noisy-like. In contrast, when the concentration of fluorescently labeled molecules is low, meaning only a few labeled molecules are present in the confocal volume at any given time, the fluorescence signal becomes more defined and less noisy. The difference between high and low concentrations in FCS signals is illustrated in figure 2.7. For instance, when the signal rises from a minimum to a peak, it indicates a fluorescent molecule entering the confocal volume. When the signal drops, the particle is leaving. In this way, the fluorescence intensity fluctuates around an average value.

The fluorescence fluctuations measured in FCS are stochastic but exhibit temporal correlation. As a result, individual signal fluctuations cannot be directly interpreted. This requires statistical analysis [35].
For dynamic processes, the autocorrelation of the fluctuating signal can be calculated (equation 2.3), and an autocorrelation curve can be obtained.

$$G(\tau) = \frac{\langle F(t)F(t+\tau)\rangle}{\langle F(t)\rangle^2} \tag{2.3}$$

For a single particle, an example is shown in figure 2.8 . From this curve, the concentration of the labeled molecules, represented by the amplitude of the autocorrelation function, can be determined. Additionally, the diffusion constant can be extracted by determining the correlation time (τ_D). This relates to the diffusion constant by $\tau_D = \frac{\omega_0^2}{4D}$, where ω_0 is the lateral radius of the confocal volume [36]. The concentration of labeled molecules and diffusion constant are obtained by fitting the best FCS model to the data.

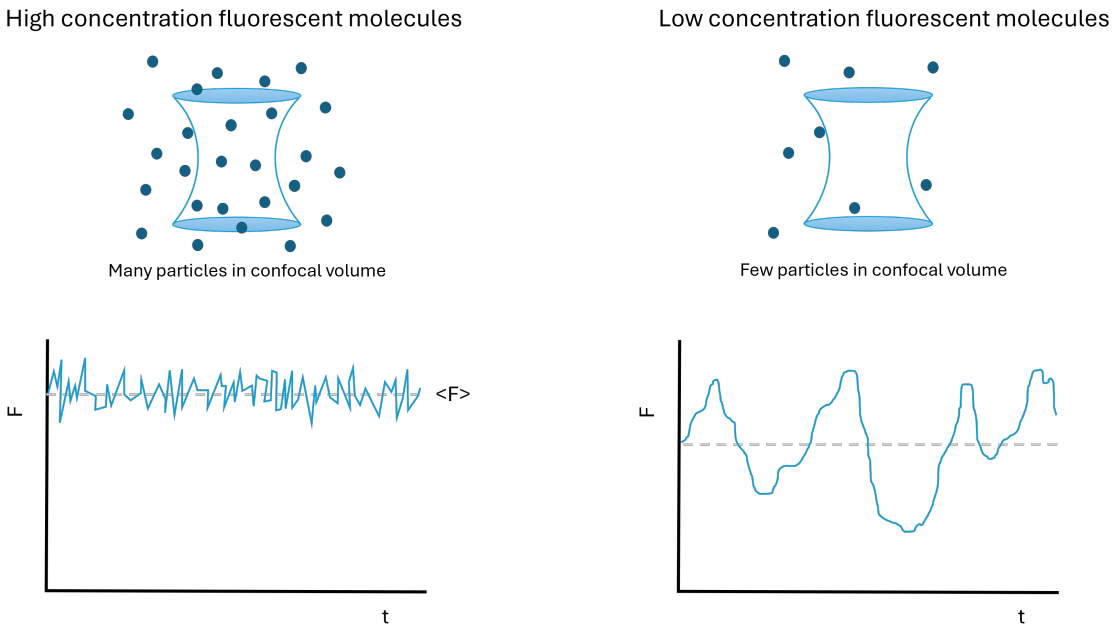

FIGURE 2.7: Figure showing time-correlated FCS signals for samples with high and low concentrations of fluorescent molecules.

When multiple diffusing species are present, the autocorrelation curve will not look as smooth as in figure 2.8. For instance, in the case of two diffusing species, the curve may resemble the one shown in figure 2.9. The data can still be fitted using an FCS model that accounts for multiple species. In this way, the concentration and diffusion coefficient of each species can still be derived. Additionally, fitting models can incorporate effects such as triplet state transitions, conformational dynamics, and protonation.

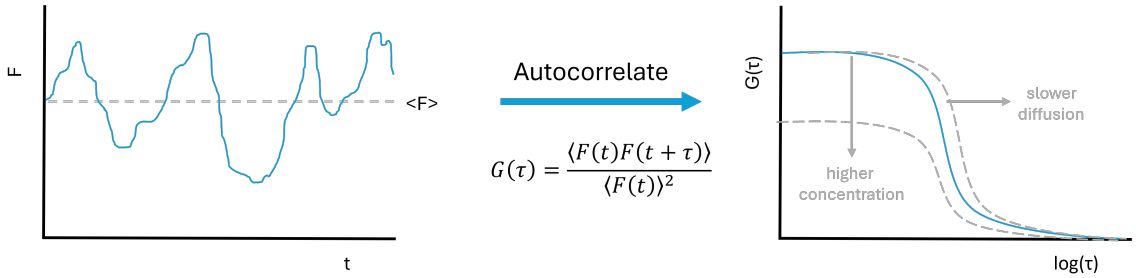

FIGURE 2.8: Data processing of an FCS fluorescence signal, resulting in an autocorrelation curve. On the left, the fluorescence intensity, F, over time is shown, with the average fluorescence intensity, $\langle F \rangle$, indicated by a dashed line. The autocorrelation of this signal is calculated using the equation in the middle of the figure, resulting in the autocorrelation curve, $G(\tau)$, shown on the right. For slower-diffusing species, this curve shifts to the right, and for higher concentration samples, the amplitude of the autocorrelation function decreases.

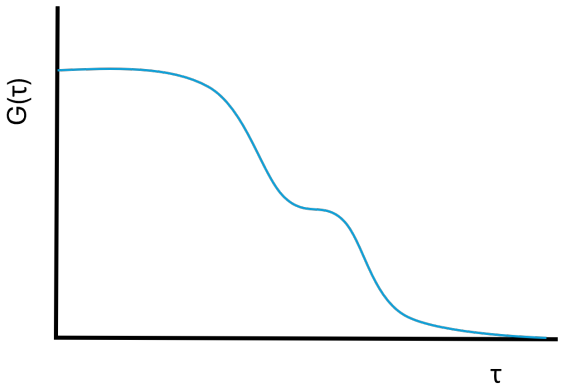

FIGURE 2.9: Example of an autocorrelation curve for two diffusing species.

Chapter 3

Methods

3.1 Protein Production

Esherichia coli BL21 (DE3) cells were used for αS expression. Recombinant human wild-type (WT) and αS-A140C were expressed using the pT7-7 expression system. The protocols for expression and purification are described in more detail in [37]. 14-3-3 was expressed using the protocol described in [38].
After purification, the proteins (in a 10 mM Tris with a pH of 7.4) were aliquoted and flash frozen. They were stored in a freezer at -80°C. The samples were thawed as needed for experiments. αS-140C samples were supplemented with 1 mM DTT (dithiothreitol).

3.2 Protein Labeling

For the experiments performed, part of the proteins used were labeled with Alexa fluor (AF) dyes. For α-synuclein labeling, the mutant αS-A140C was labeled with AF488, AF568, or AF594 (Thermo Fisher Scientific), depending on the experiment. Labeling was carried out using the manufacturer's protocol, which involves a maleimide-thiol reaction. For 14-3-3 labeling, the primary amines of the protein were targeted using either AF568 or AF647 dyes functionalized with NHS-esters. Labeling was performed using the manufacturer's protocol (Thermo Fisher Scientific).
Protein-dye conjugates were purified to remove unbound dye. This was done using a Zebaspin desalting column (7 kDa MWCO, Thermo Fisher Scientific). An RCF of 1000 and a spinning time of 2 minutes were used. After purification, concentrations of dye and protein were determined using UV-vis absorption (NanoDrop, Thermo Fisher Scientific). The protein concentration can be calculated by using the following equation [39]:

$$C_{protein} = \frac{A_{protein} - CF_{dye} \cdot A_{dye}}{\varepsilon_{protein}} \tag{3.1}$$

With $C_{protein}$ the protein concentration, $A_{protein}$ the absorbance at the characteristic wavelength of the protein (279 nm for αS, and 280 nm for 14-3-3), CF_{dye} the correction factor accounting for the dye's absorbance at the characteristic wavelength of the protein, A_{dye} the absorption coefficient at the dye's maximum wavelength, and $\varepsilon_{protein}$ the molar extinction coefficient of the protein at its characteristic wavelength. Using dye and protein concentrations, the degree of labeling (DOL) can be calculated. It is defined as $DOL = \frac{C_{dye}}{C_{protein}}$, assuming that all dye is bound to protein and that a maximum of one dye molecule is attached to each protein molecule.

After labeling, the proteins were aliquoted and flash frozen. They were stored in a freezer at -80°C. The samples were thawed from the freezer as needed for experiments.

3.3 α-Synuclein 30-mer Formation

αS 30-mers were formed following the protocol described below. The protocol is based on the protocol in [40]. A 2 mL sample with an αS concentration of around 250 μM in 10 mM Tris, $pH = 7.4$ was dried in a vacuum evaporator. The dried sample was dissolved using MilliQ water to obtain >1 mM αS. αS was incubated at 1 mM monomer concentration for 18 h at 23°C while shaking at 300 rpm. This was followed by a 2 h incubation at 37°C without shaking. The αS 30-mers were then purified using a size-exclusion column (Superdex 200 Increase 10/300 GL, Sigma-Aldrich, UK). 30-mers (and other oligomers) were collected using a fraction collector (F9-R, GE HealthCare). The concentration of 30-mers and the DOL were determined using an UV-vis spectrophotometer (UV-2600, Shimadzu) and using equation 3.1. Concentrations were 1.1 μM αS (αS monomer equivalent) and 0.24 μM (AF568 monomer equivalent), resulting in a DOL of 6.6 dye molecules per αS 30-mer. It is assumed that all αS is present in the form of 30-mers.

3.4 Fibril Formation

αS-WT monomers were incubated in a buffer with high salt concentrations (50 mM Tris-HCl, 150 mM KCl, pH = 7.4). αS monomer concentrations were 100 μM and the total volume was 1250 μL. The sample was placed in an Eppendorf Thermomixer and shaken for about 5 months at 37°C and 600 rpm.

3.5 Microscale Thermophoresis (MST)

3.5.1 Measurements

Measurements were performed using the Monolith NT.115 instrument (NanoTemper). Protein samples were measured in a buffer containing 10 mM Tris, 10 mM NaCl, 0.1 mM EDTA buffer with a pH of 7.4. Excitation was achieved using either a green LED (557 nm) or blue LED (493 nm), depending on the fluorophore used. The LED power was adjusted so that the fluorescence intensity was approximately 1000 a.u.
In the Monolith instrument, a sample tray can be placed that can contain up to 16 capillaries. The temperature was set to 37 °C. To fill the capillaries (Monolith, MO-K022), both the capillaries and sample tubes were hold horizontally, and the tip of each capillary was placed into the sample, allowing the capillary to fill by capillary forces. Care was taken to avoid trapping air bubbles. After filling, the sample tray was placed into the Monolith instrument.
For measurements of αS multimerization in the presence of 14-3-3, as well as measurements involving the addition of NaCl or 1,6-hexanediol, a control measurement was performed using only αS. This control was used to check for possible abnormalities in the WT multimerization and was prepared with the same αS dilution series as in the corresponding measurement.

3.5.2 Analysis

The MST response is determined by calculating the difference between the normalized fluorescence intensity before laser activation and while activated. This response is referred to as ΔF_{norm}. The time point at which the laser is activated, is defined as $t = 0$ s. Fluorescence intensity from $t = -1$ to 0 s is compared to that from $t = 5$ to 30 s. MST responses were measured at two different IR laser powers: 60% and 80%. The results from these measurements were averaged. Standard deviations were determined by comparing $t = -1$ to 0 s with different time regimes: early ($t = 5$ to 6 s), mid ($t = 12$ to 13 s), and late ($t = 29$ to 30 s) [7]. Standard deviations are shown as error bars in the graphs of the Results sections.
Raw data processing was done in the MO.Affinity Analysis software by NanoTemper. For samples containing more than one protein species, interaction curves were fitted using the K_d or Hill model available in the software. The K_d model describes molecular interaction assuming 1:1 binding stoichiometry. The model is based on the law of mass action. The Hill model is used in cases without 1:1 binding stoichiometry or cooperative interactions.
For experiments investigating the multimerization of a single protein species, data were analyzed using a custom-made Python script. ΔF_{norm} values were normalized based on the initial and final plateaus to obtain an MST response between 0 and 1. These normalized values are referred to as the normalized apparent monomer fraction, where 1 indicates a state with only monomers and 0 indicates a state containing both monomers and multimers. The ΔF_{norm} corresponding to the 0 to 1 range of the normalized apparent monomer fraction can be calculated for each multimerization curve.
The normalized data were fitted using the self-assembly model described in equation 2.1. To determine the best fit, multiple fits using combinations of different σ and c_c were calculated and compared to the data. The combination yielding the smallest error was considered the best fit. To minimize fitting errors due to large outliers, the fitting was performed in two stages. In the first stage, the model was fitted to all data points. In the second stage, the data point at low c_t with the largest error was marked as outlier and not taken into account, and the model was fitted again. Plots of the data with the fitted self-assembly model were generated. An example for such a plot is shown in figure 3.1.

Additionally, error plots for the fitting errors as a function of σ and c_c were created. An example for such an error plot is given in figure 3.2 Errors for each combination of σ (ranging from 10^{-4} to 10^2) and c_c (ranging from 10 to 10^5) were calculated using the following formula:

$$Error = \sqrt{\sum_{i=1}^{n} (Y_{data,i} - Y_{model,i})^2} \tag{3.2}$$

Here, $Y_{data,i}$ is the normalized apparent monomer fraction corresponding to the i^{th} concentration in the measurement series, and $Y_{model,i}$ is the fitted normalized apparent monomer fraction corresponding to this concentration. As can be observed in figure 3.2, the errors are visualized using a color map. In the error plots, the best fit is indicated by a red dot.The contours represent the error regions, corresponding to 0.5% and 3% relative errors. The inner contour shows where $Error = Error_{min} + 0.005 \cdot (Error_{max} - Error_{min})$ and the outer contour shows where $Error = Error_{min} + 0.03 \cdot (Error_{max} - Error_{min})$. Here, $Error_{min}$ and $Error_{max}$ are the minimum and maximum error of the fit for the combinations used of σ and c_c, respectively.

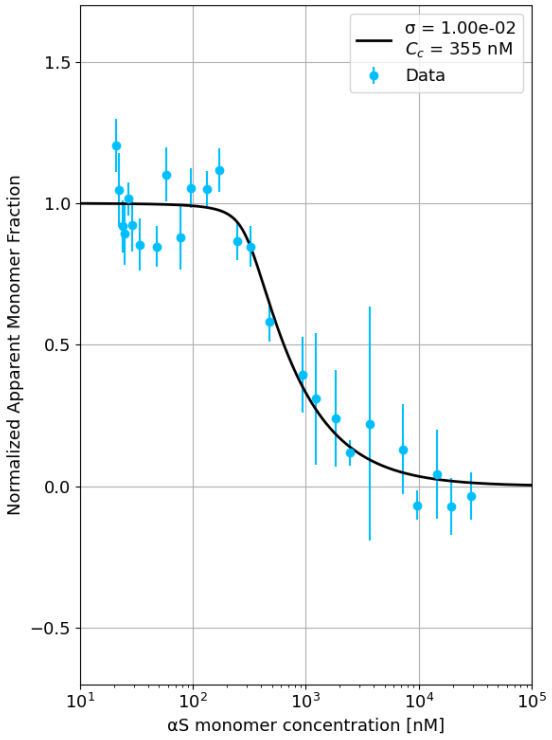

FIGURE 3.1: Example of MST data fitted to the nucleation self-assembly model.

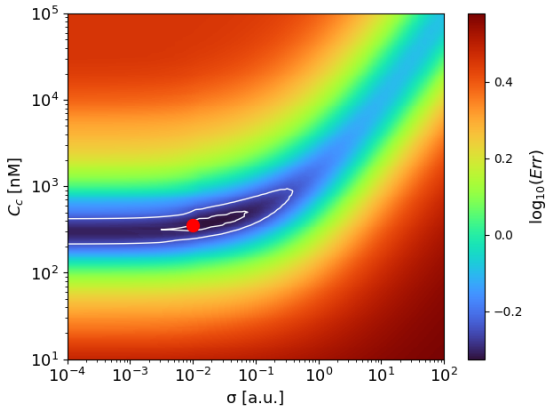

FIGURE 3.2: Example of an error plot for fitting errors of the nucleation self-assembly model.

3.6 Widefield Fluorescence Microscopy

The widefield images were captured using a Nikon Ti Eclipse inverted microscope with a Plan ADO 10x / 0.45 Dry PFS objective (Nikon, Japan). Samples contained varying concentrations of αS labeled with AF488 in 10 mM TRIS, 10 mM NaCl, 0.1 mM EDTA (pH = 7.4). Capillaries were filled with sample solution and fixed on a microscopy slide using lacquer. Excitation was performed using a FITC excitation filter (465 - 495 nm) for AF488. The experiments were conducted with the capillaries used in MST (Monolith, MO-K022) as well as with smaller rectangular cross-section capillaries (Rectangle Boro Tubing, 0.02 X 0.20 mm, 5002-050, CM Scientific).

3.7 Confocal Imaging

Confocal imaging was performed using a commercially available confocal microscope (PQ-MT200). Depending on the sample, the most suitable laser was chosen (401, 560, or 636 nm). Lasers operated at pulse rates of 20 MHz. Laser light was directed toward the microscope's objective (Olympus, UPLSAPO60XW 1.2 NA) by a dichroic mirror (Di03-R405/488/561/635-tc-25x36, Semrock). Emission light was collected by the same objective and directed through the dichroic mirror and an optional notch filter (560 nm in the case of 560 nm excitation) to a 100 μm pinhole. Additional filters were placed in front of the detectors depending on the sample. Thioflavin T (ThT) emission was detected after reflection by an H560 dichroic mirror and filtering with a 447/60 band-pass filter. AF568 emission was imaged after reflection by a T635 dichroic mirror and filtering with a 620/60 band-pass filter. AF647 emission was detected after transmission through an H560 and a T635 dichroic mirror, and filtering with either a 680/75 or a 670/70 band-pass filter (imaging of 14-3-3τ in combination with αS 30-mers).
Samples were pipetted onto a clean glass microscope slide. The glass-sample interface was set as focal plane for imaging.
For confocal imaging of fibrils, the fibrils were stained with Thioflavin T (ThT) using a ratio of 10:1 ThT molecules to αS monomer equivalents. A 401 nm laser (PicoQuant) was used for excitation.

3.8 Fluorescence Correlation Spectroscopy

FCS measurements were performed using a commercially available confocal microscope (PQ-MT200). Depending on the fluorophores used, the most suitable laser was selected (560 nm laser for AF568 excitation and 636 for AF647 excitation). Lasers operated at pulse rates of 10 MHz with a laser power of 4k a.u., corresponding to an optical power of 9 μW. Laser light was directed toward the microscope's objective (Olympus, UPLSAPO60XW 1.2 NA) by a dichroic mirror (Di03-R405/488/561/635-tc-25x36, Semrock). The objective focused the light in a diffraction-limited volume known as the detection volume. The size of this detection volume was determined using a dye with a known diffusion coefficient. The objective was focused $\sim$20 μM above the cover slip glass containing the sample. Emission light was collected by the same objective and directed through the dichroic mirror and a 560 nm notch filter to a 100 μm pinhole.
For AF568 detection, the light was reflected by a T635 dichroic and filtered by a 561LP filter before reaching the detector and a 560 notch filter was used. For AF647 detection, the light was transmitted by the T635 dichroic and filtered by a 690/70 band-pass filter before reaching the detector.
Samples were pipetted onto a clean cover glass. For FCS experiments involving αS, the microscopy cover glasses were saturated prior to use with 20 μL 5 μM αS-WT to prevent sticking of the sample to the cover glass. After saturation, the cover slip was rinsed three times with buffer, and the measurement sample was then pipetted onto the cover slip.

Fluorescence fluctuations in the sample volume were recorded. The autocorrelation curve was calculated for lag times up to 1000 ms. The curve was fitted using an extended triplet (3D) model available in the SymphoTime64 software (PicoQuant), which included one triplet state and one or two diffusing species, depending on the sample.
The model fitted in the SymphoTime64 software is described as follows: For M populations of fluorescent particles, each having a diffusion time of τ_{Di} and brightness Q_i, where the fraction the the particle number is described by F_i, the fitted model of the autocorrelation

curve, $G(\tau)$ is described by [41]:

$$G(\tau) = \frac{\sum_{i=1}^{M} (Q_i)^2 F_i g_i(\tau)}{N(\sum_{i=1}^{M} Q_i F_i)^2} \tag{3.3}$$

With in case of no triplet state, $g_i(\tau)$ is given by:

$$g_i(\tau) = \frac{1}{1 + (\tau/\tau_{Di})} \sqrt{\frac{1}{1 + (\tau/\tau_{Di})(\omega_0/\omega_z)^2}} \tag{3.4}$$

And in case of triplet state(s), $g_i(\tau)$ is given by:

$$g_i(\tau) = [1 - \tau + \tau e^{\frac{-\tau}{\tau_\tau}}] \frac{1}{N(1-\tau)} \frac{1}{1 + (\tau/\tau_{Di})} \sqrt{\frac{1}{1 + (\tau/\tau_{Di})(\omega_0/\omega_z)^2}} \tag{3.5}$$

Here, τ_D is the average residence time of the fluorescent particles in the detection volume, $N(t)$ the number of particles in the detection volume, and τ_τ the characteristic time-scale of the triplet state transition. The ratio ω_z/ω_0 is called the structure parameter and described the shape of the detection volume, and the diffusion time of particle i is given by:

$$D_i = \frac{\omega_0^2}{4\tau_{Di}} \tag{3.6}$$

Chapter 4

Studying α-Synuclein Multimerization in MST

Early stages of aggregation are challenging to study, but are likely rather important in protein quality control. MST has been shown to be a useful method for studying these early events, namely through the fluorescence response of a labeled protein following the introduction of a temperature gradient. This response results from some factors, including diffusion and the temperature sensitivity of the dye. For the multimerization curve of αS, it is expected to observe something like the curve obtained by [7], as similar experiments are performed here. However, studying αS multimerization in MST is not straightforward; certain aspects need testing or optimization to achieve better results. Some of these optimizations were carried out at the start of the project, while others were implemented along the way. This chapter outlines these optimizations and ends with the resulting typical binding curve of αS multimerization, obtained using a global fit of multiple MST measurements.

4.1 Establishing a Suitable Dye-Labeling Strategy

4.1.1 Testing different Fluorophores

Labeled αS was tested with different Alexa Fluorophores in order to find the one most compatible with MST. The most important property of the αS-dye complex is a low affinity for the capillary glass, in other words: low stickiness. This is important to maintain a homogeneous distribution of the labeled αS in the capillary, otherwise a false positive binding- or multimerization curve can be obtained [32]. The used capillaries have a circular cross-section. Assuming a homogeneous distribution of the fluorophore in the capillary, a scan of fluorescence counts in the direction perpendicular to the capillary length would result in a Gaussian shape. When this is not the case, the dye is likely sticking to the capillary wall [42].
Furthermore, on one hand, sufficient fluorescence is needed for an accurate read-out. On the other hand, the concentration of the labeled protein should be as low as possible, because in the case of multimerization, this defines the lower limit of the curve. Therefore, a fluorophore with high brightness is most advantageous.

Three potentially suitable fluorophores were initially selected; AF488, AF568, and AF594. αS-A140C was labeled with these dyes, following the protocols described in the Methods section. The labeling position is located at the end of the C-terminal domain, which lies

outside the NAC-region, which is involved in monomer-monomer binding during multimerization. By labeling the end of the C-terminal, the label is expected not to interfere with multimerization.
Labeled proteins were diluted; final concentrations will be mentioned later. Capillaries were filled with these samples and put in the Monolith instrument at 37°C. Measurements of fluorescence counts were performed with the scanning direction perpendicular to the capillary length. Excitation was done using the blue LED for AF488 and using the green LED for AF568 and AF594.
In figure 4.1(A), the normalized capillary scans are shown for the different AF labeled αS. The capillary scans for the three dyes deviate significantly with respect to a Gaussian, which indicates sticking of the dye to the capillary surface.
The fluorescence intensity at the capillary center is 1000 a.u for AF488 (75 nM dye and 65% LED power), 300 a.u for AF568 (40 nM dye and 95 % LED power), and 400 a.u. for AF594(40 nM dye and 95 % LED power). Taking into account LED power and concentration, AF488 has the highest fluorescence intensity of the dyes tested. The differences in intensities are likely due to different excitation efficiencies, as only two LEDs are available for excitation, which may not provide the optimal excitation wavelength for each fluorophore. For AF568 and AF594, the fluorescence intensity only reaches 300 or 400 a.u. at the maximum LED power, where ideally a fluorescence intensity of 1000 a.u. is desired. This indicates that the dye concentration should be increased. However, this increases the lower limit of protein concentrations that could be measured.

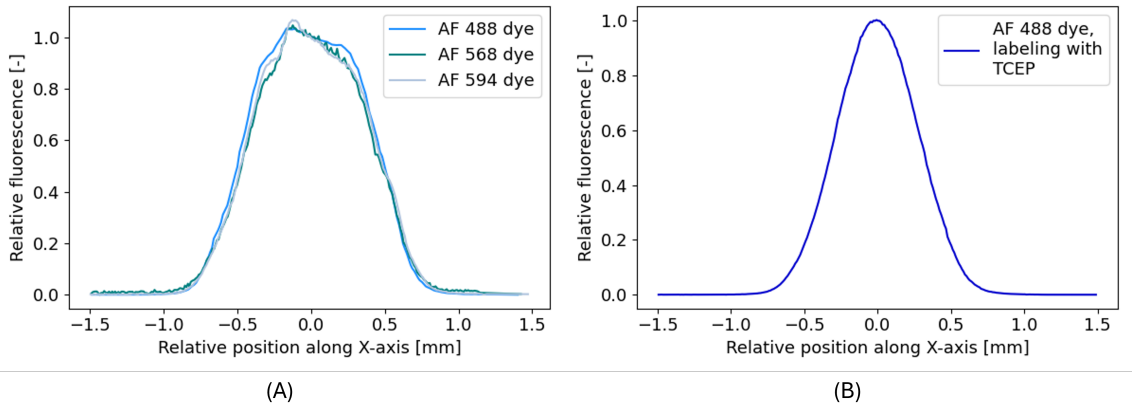

FIGURE 4.1: Normalized capillary scans measured of αS labeled with different Alexa Fluorophores using the Monolith instrument. The y-axis represents the relative fluorescence intensity and the x-axis the relative position across the capillary cross-section, perpendicular to the capillary length. In (A) the capillary shapes for the sticky dyes are shown, and in (B) the capillary shape for the non-sticky one is shown (Gaussian shape).

4.1.2 Addition of TCEP during Labeling

Unfortunately, all three dyes show stickiness, and are therefore not suitable for MST. At NBP, it was previously observed that the presence of the reducing agent tris(2-caroxyethyl)phosphine (TCEP) during labeling could have a role in preventing stickiness. Therefore, it was attempted to change the labeling protocol with TCEP present in a concentration of 10 mM during labeling of αS-A140C. This adapted labeling protocol is used for AF488, as this dye shows the highest fluorescence intensity for the available excitation and emission sets

in the Monolith instrument. After incubation, excess label and TCEP were removed using a Zebaspin desalting column (7 kDa MWCO, Thermo Fisher Scientific) twice.
Measuring the capillary shape of this dye in the Monolith instrument gave a Gaussian shape (figure 4.1(B)), indicating no stickiness [32]. This is ideal for MST measurements. The fluorescence intensity obtained in the center of the capillary was 1000 a.u. for 20 nM dye and 65 % LED power, or 500 a.u. fluorescence intensity for 13 nM dye and 95% LED power. This fluorescence intensity is suitable for MST measurements, indicating that even at these low protein concentrations, MST measurements can still be performed. The fluorescence intensity increased compared to αS labeled with AF488 without TCEP during labeling. This is likely due to sticking of the fluorophore to the capillary walls in the case without TCEP. Intensities are measured at the center of the capillaries, meaning that when the labeled protein sticks to the capillary wall, less labeled protein remains in solution, giving a lower fluorescence intensity at the center of the capillary.
Based on these results, αS-A140C-AF488 with TCEP added during labeling is the best available option for MST experiments. Labeling with AF568 and AF594 in the presence of TCEP could also be attempted, as this might reduce the stickiness of these dye-protein complexes. However, since a successful approach was found using AF488, it was decided to proceed with that dye. Moreover, based on the observed intensity differences between AF488 with and without TCEP added during labeling, it is not expected that AF568 and AF594 would yield higher fluorescence intensities than AF488.

4.1.3 Visualizing Dye Stickiness

To deeper investigate the sticking behavior of the dyes, widefield fluorescence microscopy of capillaries filled with labeled αS-A140C was conducted. Samples of αS-AF488, with and without TCEP added during labeling, at two different concentrations (7nM and 20 nM) were used. These concentrations are selected, because these concentrations of αS-AF dye were used during MST experiments. Furthermore, samples were measured in both types of capillaries mentioned in the general Widefield Fluorescence Microscopy Methods section. When using the Monolith capillaries (with a circular cross-section), it is not possible to bring them in focus. However, this is possible with the Rectangle Boro Tubing, and therefore this tubes were also tested. The resulting widefield microscopy images are shown in figures 4.2, 4.3, and 4.4.
For figure 4.2, the Monolith capillaries are used. Due to their cylindrical shape and relatively large dimensions, it is not possible to bring the capillaries in focus. However, this image still gives an indication for the fluorescence intensity distribution across the capillaries. For capillaries 1 and 2 (from the top, ones labeled without TCEP), the edges of the capillaries are clearly visible, showing a higher fluorescence intensity than the center of the capillaries. In contrast, for capillaries 3 and 4 (ones labeled with TCEP), the fluorescence intensity is highest at the center of the capillaries and decreases toward the edges. Overall, the 20 nM dye samples show higher overall fluorescence intensity than the 7 nM ones.

In figure 4.3, Rectangle Boro Tubing is used. In capillaries 1 and 2, the fluorescence intensity is highest at the ends from which the capillary was filled. Moving to the other end, the intensity decreases. For capillaries 3 and 4, the fluorescence intensity is spread more evenly across the capillary length. As a result, the end on the right-hand side of capillary 4 is the most clearly pronounced of all capillaries in this figure. For capillary 4, the fluorescence intensity is also highest at the end from which the capillary is filled, but not as high as for capillary 2. This can be explained by the filling procedure of the capillaries, in which the end of the capillary is placed in the sample. When some sample liquid with dye remains on the outside of the end of the capillary, the end can appear

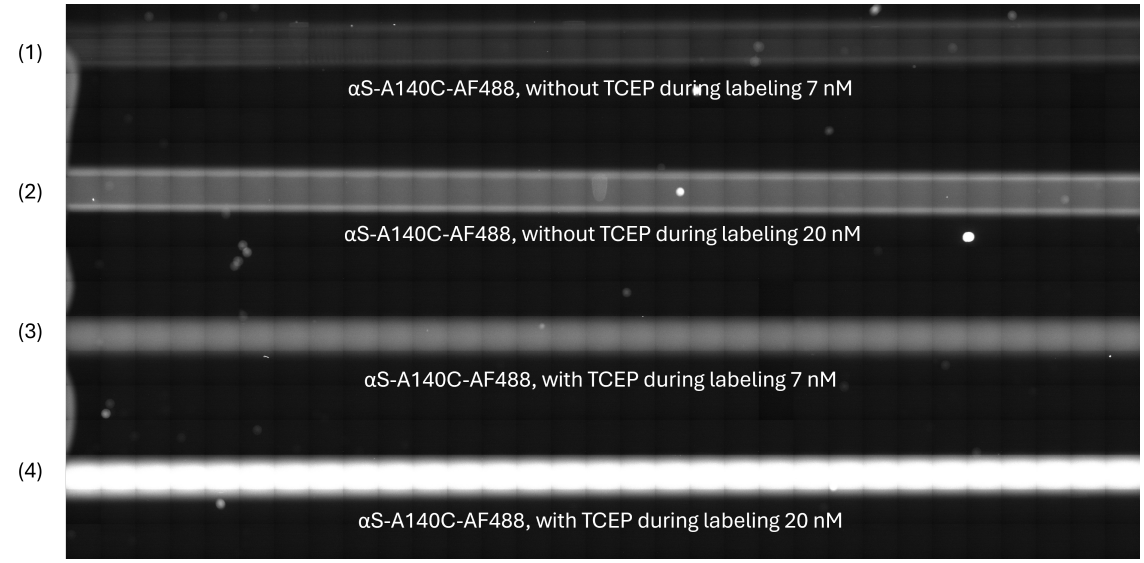

FIGURE 4.2: Widefield fluorescence microscopy image of Monolith capillaries, filled with samples of αS-A140C-AF488, with and without TCEP during labeling, in concentrations of 7 and 20 nM.

brighter.

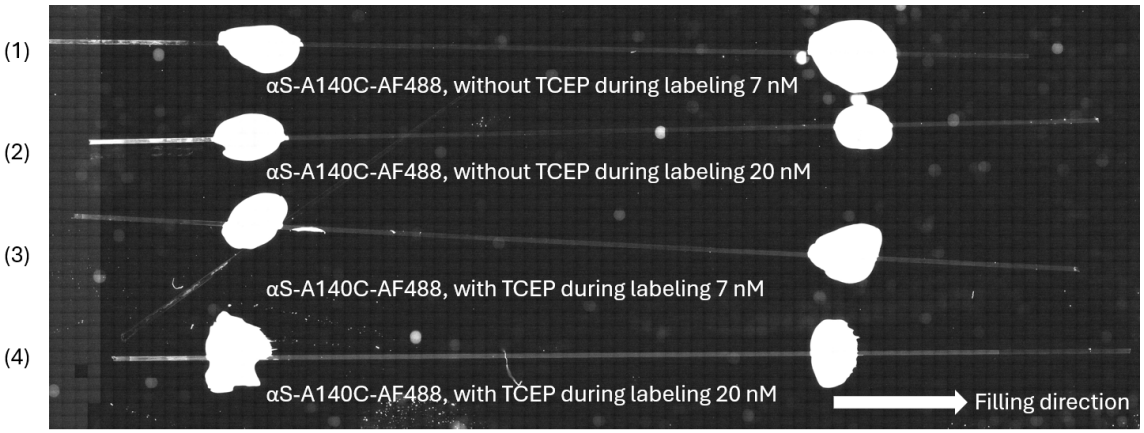

FIGURE 4.3: Widefield fluorescence microscopy image of Rectangle Boro Tubing capillaries, filled with samples of αS-A140C-AF488, with and without TCEP during labeling, in concentrations of 7 and 20 nM. The eight bright blobs in the figure correspond to the lacquer used to fixate the capillaries.

Figure 4.4 shows close-ups of the capillary ends (from which the capillaries are filled) from figure 4.3. These images more clearly highlight the differences in fluorescence intensity at the ends.

Based on the widefield fluorescence microscopy images, differences in sticking can be observed when comparing αS-A140C labeled with AF488 with and without TCEP added during labeling. When TCEP is not added, the higher fluorescence intensity at the capillary edges in figure 4.2 indicates sticking, as performing 2D imaging in the y-direction, the capillary edge region includes relatively more glass-sample interface. This results in a higher fluorescence intensity at the capillary edges when the labeled αS is sticky. In contrast, when labeling is performed with TCEP, the intensity increases more at the capil-

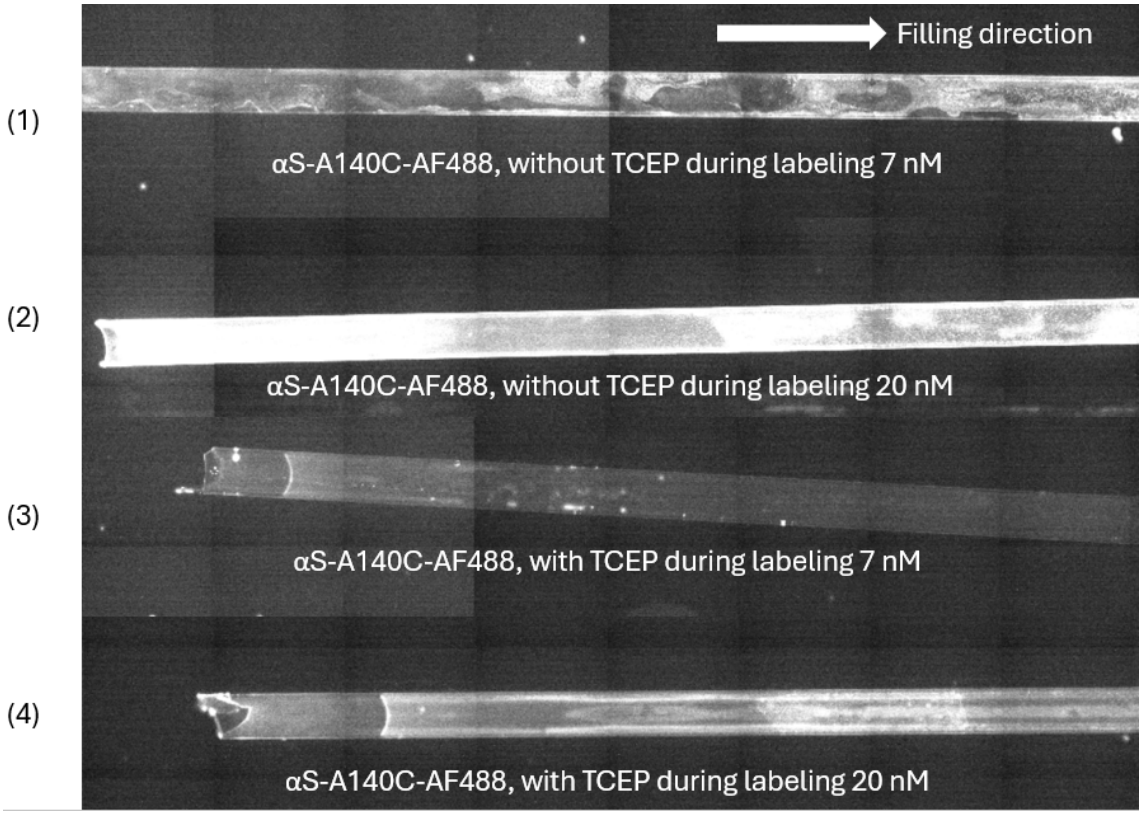

FIGURE 4.4: Close-up of the widefield fluorescence microscopy image at the capillary end of Rectangle Boro Tubing capillaries, filled with samples of αS-A140C-AF488, with and without TCEP during labeling, in concentrations of 7 and 20 nM.

lary center, indicating no to minimal sticking. Figures 4.3 and 4.4 show higher fluorescent intensities in the capillary ends for the case where no TCEP is added during labeling. This indicates that during filling, the AF-488 sticks and reduces the AF488 concentration in solution, resulting in a decreased AF488 concentration along the capillary length. This also indicates that the sticking process is rapid, as it immediately occurs during filling. Furthermore, during filling, the capillary end is placed in the sample solution, creating an additional liquid-glass interface where sticking can occur, resulting at a higher fluorescence intensity at the capillary end. This is also visible for capillary 4, although lower than that of capillary 2 with the same dye concentration. Therefore, it is expected that for capillary 4, this effect is mainly caused by the filling procedure.

4.1.4 Conclusion

Of the dyes tested, labeling αS-A140C with AF488 with TCEP added during labeling is the most suitable option. This with dye labeled αS did not stick to the capillary walls and showed the highest fluorescence intensity in the Monolith instrument. The other αS-dye combinations tested showed stickiness based on their capillary scans (figure 4.1(A)), resulting in a very inhomogeneous dye distribution, which is even visible as a decrease in fluorescence intensity along the longitudinal axis of the capillaries. Therefore, these αS-dye combinations are not suitable for MST experiments.

4.2 Enhancing Curve Resolution: From 16- to 32-Point Multimerization Curves

4.2.1 Fitting 16-Point Multimerization Curves

For this study, it is important to get reliable fits of MST data for correct interpretation of the data. Initial measurements contained 16-points, because this is the amount of capillaries the Monolith can measure in one run. MST measurement results with 16-points could look like as shown in figure 4.5. Here, two fits of the nucleation self-assembly model are shown; one with high cooperativity ($\sigma = 0.001$), and one with no cooperativity ($\sigma = 1$). Both fits could describe the data, and it is hard to tell which fit is better. The main issue is that data density is limiting the curve reliability, a problem that could easily be solved by increasing the number of data points.

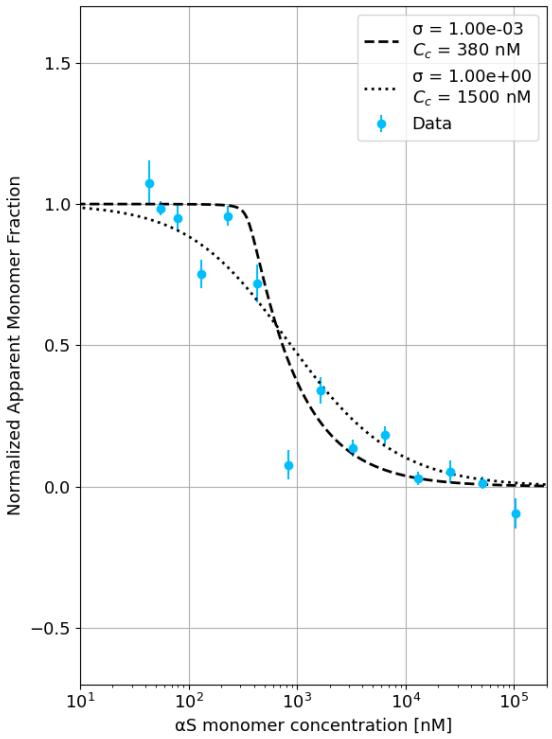

FIGURE 4.5: Example of a 16-point MST measurement. In this figure, the nucleation self-assembly model is fitted for two different cooperativity factors, σ.

4.2.2 Increasing Data Density

To increase data density, it is proposed to extend the measurement with an extra MST run to increase the number of concentrations measured per experiment from 16 to 32. The added concentrations are particularly valuable in the transition region from monomers to a mix of monomers and multimers, where relatively few data points span this range. More data in this region enhances the accuracy of the fit.
In addition to the standard 16-point MST dilution series, an additional sample dilution series with intermediate concentrations was prepared using the original series as basis. The first dilution series was measured with MST first, followed by the second dilution series.

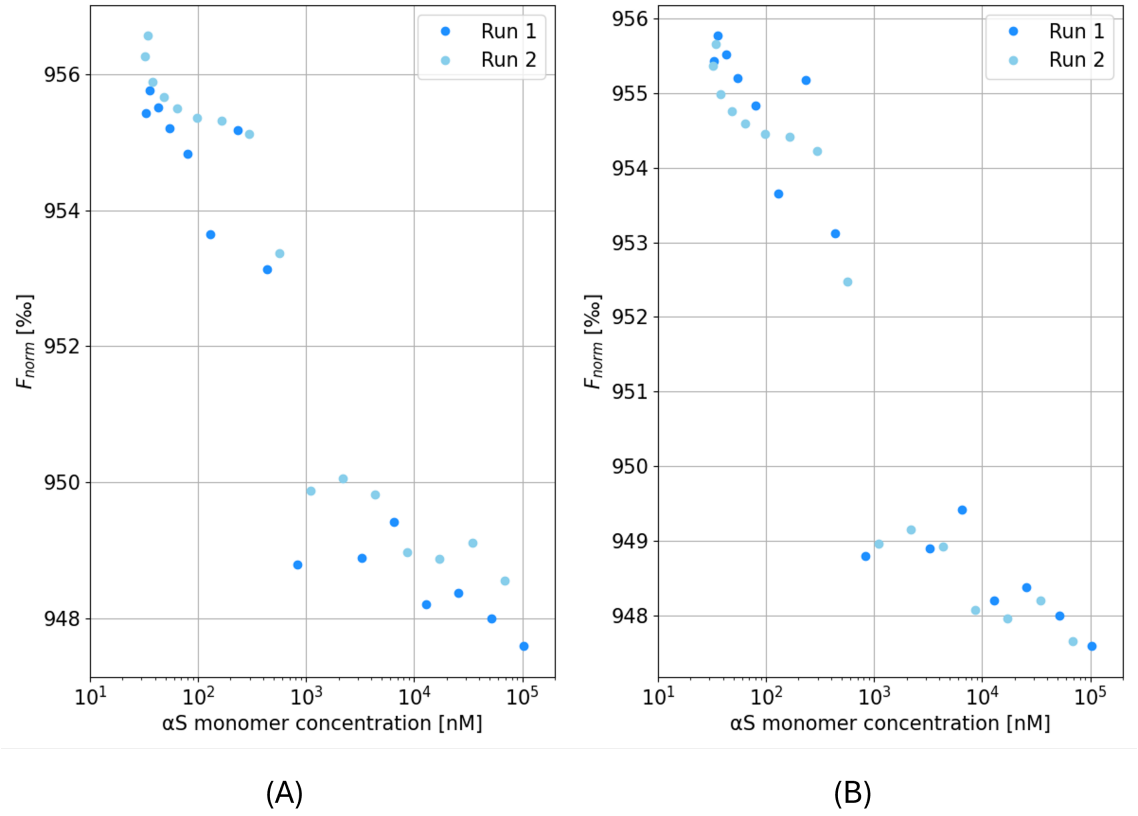

FIGURE 4.6: Example of a MST measurement at 60% IR laser power. (A) Shows two MST runs before any correction is applied. Between these runs, an offset can be observed. (B) Shows the same measurement with a correction of F_{norm} values, based on the averages of both runs.

During measurements, a small offset in ΔF_{norm} values between these two MST runs was noticed. An example of a measurement is shown in figure 4.6(A). For this example, almost all data points of the second run have larger ΔF_{norm} values than that of the first run. This indicates an offset in ΔF_{norm}. These offsets can be corrected for by calculating the average of both runs. Based on these averages, data for the second run was shifted in such a way that the average equals that of the first run. The result of this correction is shown in figure 4.6(B), which shows an improvement in the merging of two data sets. After the correction, the data of both runs were merged and processed as usual (described in Chapter 3.5.2). Performing ΔF_{norm} offset corrections is not an uncommon practice and is also mentioned in [43].

4.2.3 Using Overlapping Concentrations for ΔF_{norm} Corrections

There is another way to improve the merging of two MST runs to get a more reliable fit. As described in the previous section, the ΔF_{norm} offset correction is based on the average values of the total concentration series. However, the average of the concentrations measured in the first run is slightly lower than that in the first run. This can result in a small discrepancy in ΔF_{norm} correction. Next to that, the runs can not be compared directly, because the samples are different in each case. Therefore, the proposed solution is to use a 32-point MST that includes certain concentrations measured in both runs, so called "over-

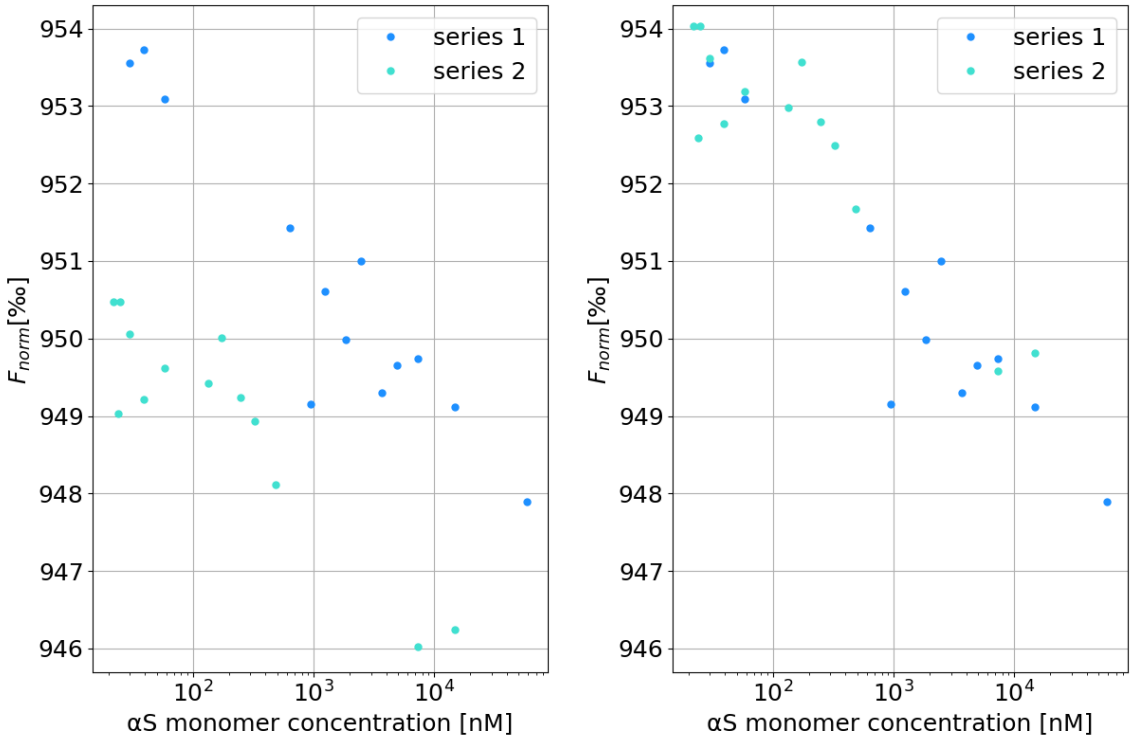

(A) Before correction.

(B) After correction.

FIGURE 4.7: Example of an experiment for which correction of ΔF_{norm} values had a great impact. Results shown are the average result of 60% and 80% MST laser power.

lapping concentrations", to allow for more reliable cross-comparison and correction.
For the correction based on overlapping concentrations, concentrations that are generally in the middle of the multimerization plateaus are chosen, as these concentrations have the most stable MST responses. Three concentrations are selected from each of the initial and final plateaus. For each plateau, the average value ΔF_{norm} is calculated separately. These two averages are then combined to obtain a single average ΔF_{norm} value per MST run. Based on these values, a correction is performed by shifting the data for the second run in such a way that the plateau average equals that of the first run. Data for both runs were merged and processed as usual (described in Chapter 3.5.2).

An extreme example of a correction based on overlapping concentrations is shown in figure 4.7. This figure shows that the correction of the offsets in ΔF_{norm} is effective. The data have been merged in such a way that overlapping concentrations now exhibit similar ΔF_{norm} values. This improvement makes it possible to perform a reliable fit of the nucleation self-assembly model, which was not feasible prior to the correction. The overlapping concentrations make sure that both MST runs are complementary.
This way of correcting values is developed during course of this study, and is therefore not applied for all MST measurements. MST measurements without overlapping concentrations will still be corrected using overall averages. It is also important to note that the accuracy of the correction decreases if MST traces need to be excluded (e.g., due to for example bubble formation in capillaries). When traces from overlapping concentrations are

excluded, the correction is based on fewer concentrations, resulting in reduced accuracy. The question remains why ΔF_{norm} values can differ so much between the runs. There is no straightforward answer to this question, but may be searched in small fluctuations in laser intensity, detector sensitivity or sample position between the different runs.

4.3 Addressing Outliers: Evaporation and Bubble Formation

A considerable number of outliers were observed in the ΔF_{norm} values. Observations of the capillaries after measurements showed some evaporation at the capillary ends and bubble formation in the capillaries. This section investigates whether these processes contribute to the number of outliers in the data.

4.3.1 Evaporation

During MST measurements, the temperature in the Monolith instrument is set to 37°C. During measurement (taking approximately 30 min), the sample may evaporate at the ends of the capillaries. To assess the actual impact of evaporation on the measurement data and determine whether corrections are needed, the following experiment was performed:

A dilution series was prepared with concentrations ranging from $\sim$ 100 μM of αS-WT and below. Each sample contained 20 nM αS-AF488. MST measurements were performed of this dilution series using the blue LED for excitation. The MST measurement was repeated after one hour and two hours, without removing the sample tray from the Monolith instrument. For these measurements at t = 1 h and t = 2 h, the number of fluorescence counts (F_{counts}) of the capillaries and the F_{norm} values of the MST traces were compared with that of the measurement at t = 0 h, giving ΔF_{counts} and ΔF_{norm}. In case of a significant effect of evaporation, it is expected that the fluorescence counts (F_{counts}) in the detection volume increases, as the concentration of fluorescent particles increases due to evaporation of the water in the sample.
The differences in F_{counts} and F_{norm} values, relative to the initial measurement at t = 0, were plotted for each total αS concentration measured. Additionally, the differences in F_{counts} were plotted as a function of F_{norm} values to examine their relationship. Results for 60% and 80% MST laser power are averaged in the plots.

The number of fluorescence counts (F_{counts}) was measured, and the difference compared to $t = 0$ is plotted in figure 4.8. This figure shows that the results of the measurements at t = 1 hour and t = 2 hours lie around the values at t = 0 hours with an average decrease in ΔF_{counts} of -0.12% and -0.16% (compared to F_{counts} at t = 0) for t = 1 hour and t = 2 hour, respectively. Most deviations (in absolute values) are between 0 and 1 % with a medians of 0.36% and 0.54% for t = 1 h and t = 2 h, respectively. The deviations with respect to t = 0 do not seem to be concentration dependent, as ΔF_{counts} is randomly distributed around zero. The mean values and their standard deviations for F_{counts} are as follows: 991 ± 46 counts, 990 ± 42 counts, 990 ± 46 counts for t = 0 h, t = 1 h, and t = 2 h, respectively.
Figure 4.8 shows no clear relation between the fluorescence counts, F_{counts}, and the amount of time after which a measurement is performed, indicating no significant effect of evaporation on particle concentrations. This conclusion is supported by the random spread of points around $\Delta F_{counts} = 0\%$ relative to t = 0 h. Furthermore, the mean values and their variation (represented by the standard deviation) are very similar. Additionally, the

deviations compared to the measurement at t = 0 h do also not seem time-dependent. In summary, this graph does not show a clear effect of evaporation on the composition of the sample during MST measurements.

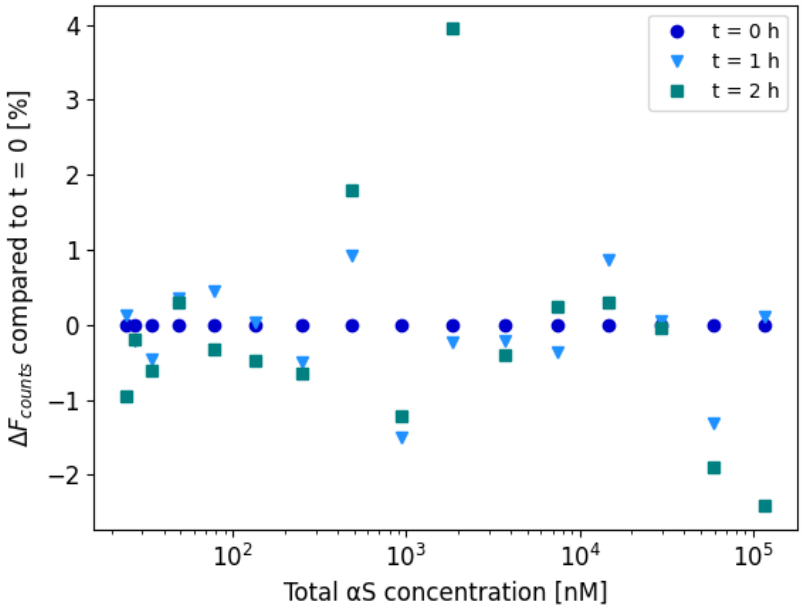

FIGURE 4.8: Difference in fluorescence counts (ΔF_{counts}) compared to t = 0 for t= 0, 1, and 2 hours. Differences are plotted for each measured αS concentration.

The ΔF_{norm} values could also give an indication of the effect of evaporation on the measurement results, and are plotted in figure 4.9. This figure shows that most F_{norm} values for t = 1 h and t = 2 h are below those of t = 0 h. Average values are -0.63‰ and -0.48‰ for t = 1 h and t = 2 h, respectively. The mean values and their standard deviations of F_{norm} are given by 947.7 ± 2.6, 947.0 ± 2.5 and 947.2 ± 2.4 for t = 0 h, t = 1 h, and t = 2 h, respectively. These results indicate a change in ΔF_{norm} values over time, of which most measurements at t = 1 h and t = 2 h show a decrease in ΔF_{norm}. Making a conclusion based on these results is complicated due to a general difference in average F_{norm} values between different MST runs, a problem encountered earlier. This discrepancy results in ΔF_{norm} values that are not directly comparable, as was attempted in figure 4.9.

To assess the relationship between ΔF_{counts} and ΔF_{norm} over time, ΔF_{counts} is plotted as a function of the corresponding value of ΔF_{norm} in figure 4.10. This plot shows a point cloud that is more or less randomly distributed, and no clear relation between ΔF_{norm} and ΔF_{counts} is observed (taking into account a possible offset in ΔF_{norm} between the different measurements), which is consistent with the expectation that evaporation has no effect on the measurement results.

In conclusion, this experiment demonstrates that there is no clear effect of evaporation on the results obtained in the Monolith instrument, indicating that there is no need to make corrections for evaporation. By visual inspection of the capillaries, some evaporation was visible at the ends of the capillaries, so this is not completely in line with the results obtained in this section. However, small differences in concentrations will probably be

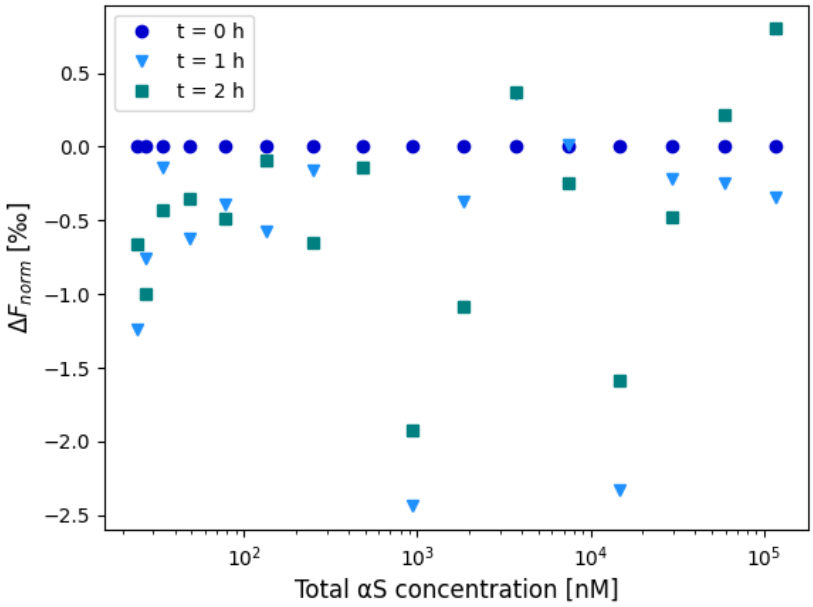

FIGURE 4.9: Difference in F_{norm} values (ΔF_{norm}) compared to t = 0 for t= 0, 1, and 2 hours. Differences are plotted for each measured αS concentration.

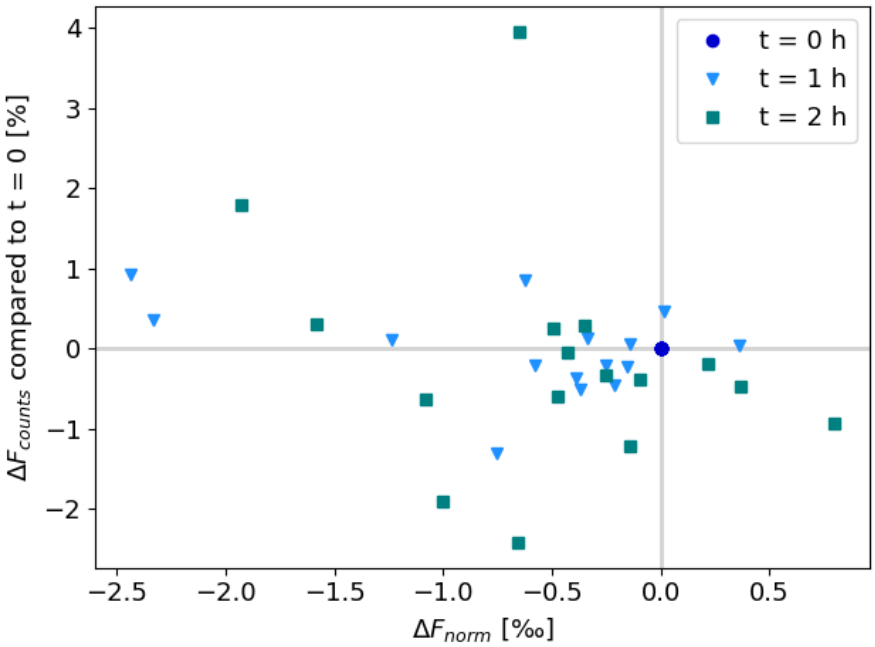

FIGURE 4.10: Relation between the difference in fluorescence counts (ΔF_{counts}) and difference in F_{norm} values (ΔF_{norm}), compared to t = 0 for t= 0, 1, and 2 hours.

minimally visible, as the concentrations are plotted on a logarithmic scale.

4.3.2 Reduction of the Effect of Bubbles

During measurements, it was observed that a significant number of the measurements resulted in "strange" MST traces. These traces showed drops or increases in fluorescence counts, deviating from the typical shape of MST traces observed in the experiments (figure 4.11). Upon inspection of the capillaries after retrieval from the Monolith instrument, bubbles were found in a significant number of capillaries, particularly located in the middle of the capillaries. This makes sense, as the capillaries are aligned horizontally, bubbles tend to move towards the middle. This is problematic, because measurements are performed in the middle. The "strange" MST traces observed are likely caused by bubble formation in the capillaries, which can disturb the measurement results when they are present in the measurement volume [44][45]. However, it is important to note that the "strange" traces may also arise from other factors, such as aggregation, surface interactions, etc. [32]. Nevertheless, this section focuses specifically on bubble formation and the potential improvements that could result from reducing the presence of bubbles in the measurement volume.

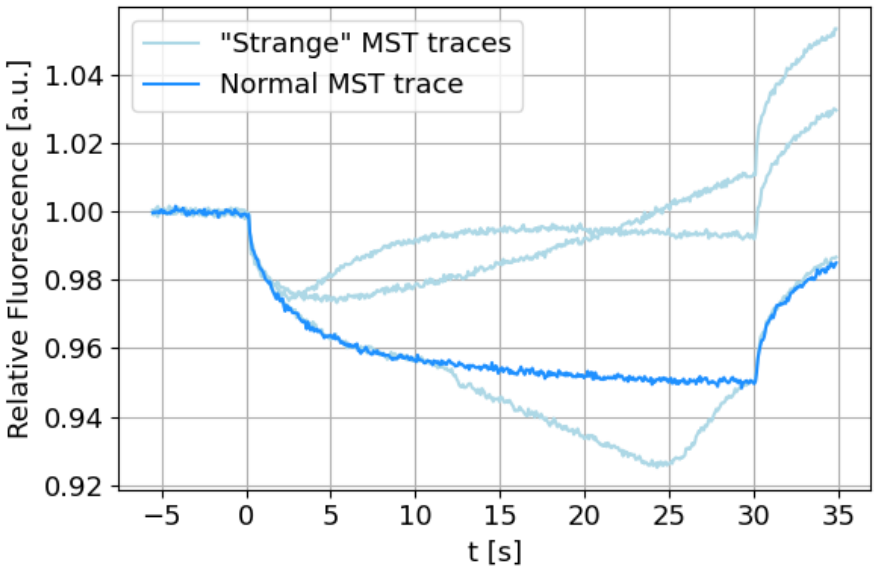

FIGURE 4.11: Difference between a normal MST trace and "strange" MST traces. These traces are examples captured during αS multimerization experiments.

In order to reduce the problem of bubbles in the measurement volume, the capillaries are slightly shifted to one side of the sample tray before placing the tray in the Monolith instrument.

This optimization lacks measurement results to support the alteration. Observations indicated that the location of the bubbles was generally shifted more toward the direction of the capillary shift, rather than being in the measurement volume. As a result, less outliers were observed in the MST traces. Therefore, this optimization seems to be helpful in obtaining more usable MST traces. Consequently, this adaptation was implemented after testing. Additionally, if shifting the capillaries does not improve the results, it also does not cause any harm. Therefore, there is no reason not to implement this adaptation. However, after implementing this adaptation, the "strange" MST traces did not disappear completely. This suggests that other factors may also contribute to the appearance of these

traces.

4.4 Establishing the α-Synuclein Multimerization Curve in MST

4.4.1 Reasoning

The primary goal of this chapter is to optimize studying αS multimerization. Using the insights gained in the previous paragraphs, αS multimerization is studied. Parameters such as the cooperativity factor and critical concentration provide more insight in the characteristics of the multimerization process, making them of particular interest. Here, αS multimerization experiments are conducted, and a fit based on the nucleation self-assembly model is established. This fit serves as a reference control for other measurements performed in the upcoming chapters, where αS multimerization is studied under different conditions. The fit is obtained by performing a global fit on multiple αS WT batches.

4.4.2 Performing the Global Fit

MST measurements (32-points with ΔF_{norm} offset using the overlapping concentrations) were performed on dilution series of three different batches of αS-WT (produced on different moments) in order to get a global dataset, which shows the basic properties of αS multimerization. The highest concentrations αS-WT were $\sim$ 100 μM. Samples had dye concentrations of 13 nM αS-AF488, and the blue LED was used for excitation. For each WT batch individually, the data were processed as described in Chapter 3.5 up to the point of fitting the binding curve. The data from all three WT batches were then merged, and the binding curve was fitted according to the nucleation self-assembly model (equation 2.1), resulting in a global fit. The nucleation self-assembly model was also fitted for each WT batch individually. The errors of the fit can be plotted as a function of the cooperativity factor σ and the critical concentration c_c.
The global fit including data for all three different WT batches is shown in figure 4.12. The global fit provides a good fit to the data from all WT batches together. The fit is optimal for $\sigma = 1.00 \cdot 10^{-2}$ and $c_c = 316$ nM. This low cooperativity factor suggests a cooperative multimerization process. This is in line with earlier results at NBP [7]. From the error plot (figure 4.13), it can be observed that the fit optimum lies in a region with a quite well-defined critical concentration c_c, and a cooperativity factor σ with a larger error margin ranging from approximate 10^{-1} and below. Taking the error regions into account, values of σ and c_c are very comparable to the results obtained in [7].
To perform the global fit, the data were normalized. Normalization to a range from 0 to 1 corresponds to an average difference in ΔF_{norm} of 4.0‰ (4.55‰, 4.04‰, and 3.31‰ for the WT batch 1, 2, and 3, respectively). This value may not say anything on itself for now, but may be valuable in comparing different multimerization curves later on.

4.4.3 Individual WT batches

For each WT batch, MST results can be compared to the global fit. In figure 4.14, the data per WT batch is shown, including the global fit. When comparing the fit to all batches individually, the fit also seems appropriate for each batch, indicating similar multimerization behavior for all batches αS.

In figure 4.15, the error contours for the fits of the nucleation self-assembly model are shown for each WT batch individually. These error regions look very similar and all have

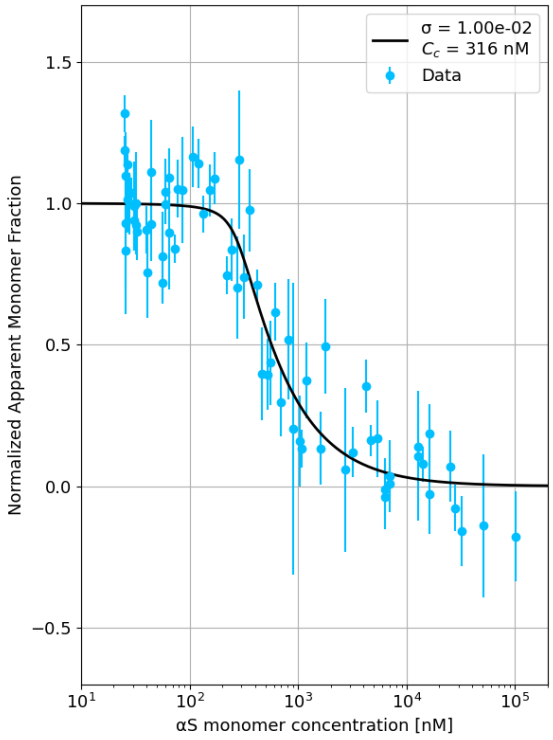

FIGURE 4.12: Global fit for all three αS-WT batches.

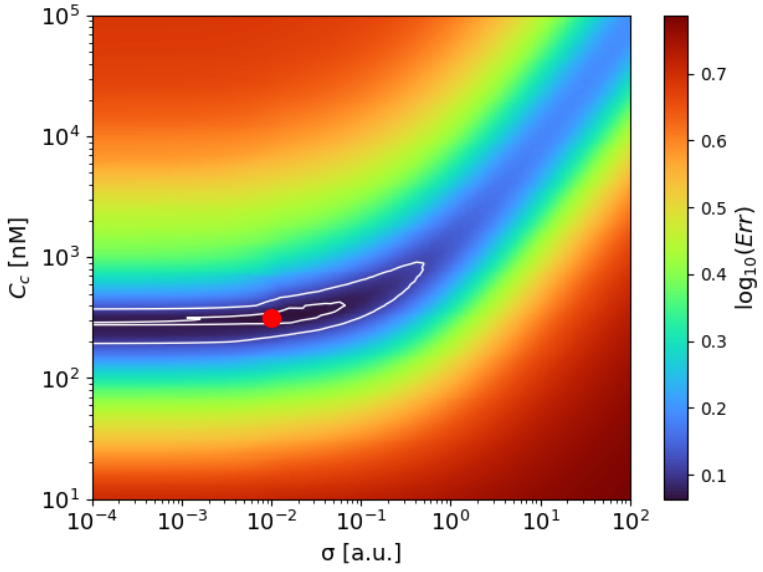

FIGURE 4.13: Error plot for fitting errors of the self-assembly model for the global fit of all three αS-WT batches.

similar ranges in cooperativity factor and critical concentration. Therefore, the global fit is a good description of the data set.

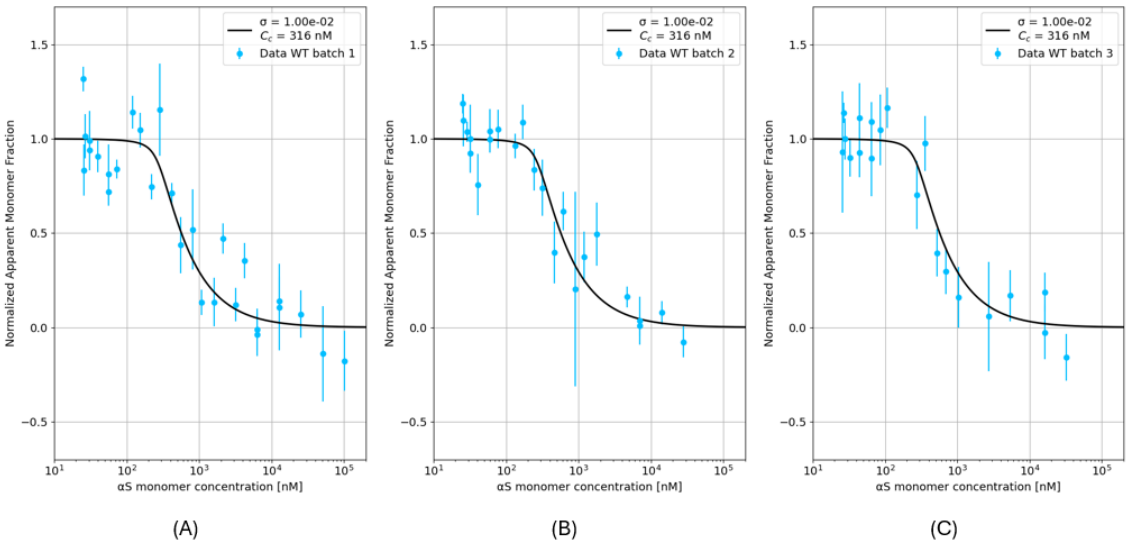

FIGURE 4.14: Data for the WT batches separately, including the global fit for all three αS-WT batches. (A) shows WT batch 1, (B) shows WT batch 2, and (C) shows WT batch 3.

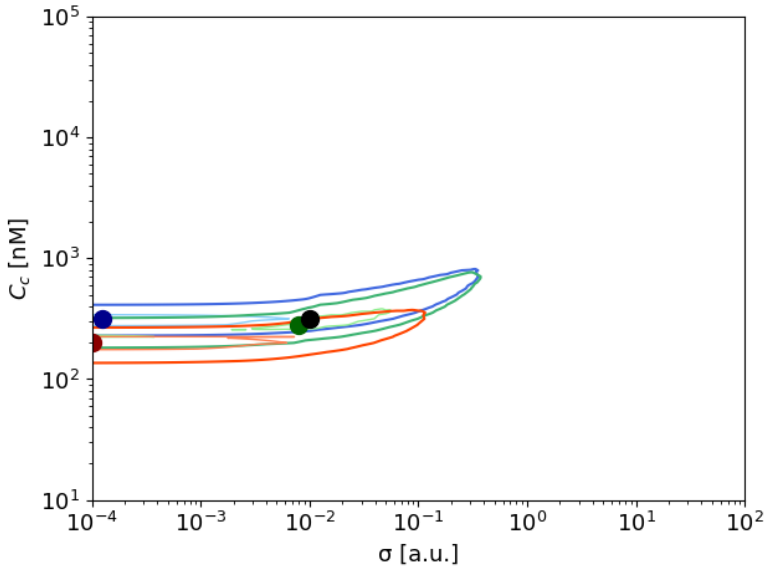

FIGURE 4.15: Plot of the error contours from fitting the nucleation self-assembly model to each WT batch separately. The error contours for WT batch 1 are shown in blue, WT batch 2 in green, and WT batch 3 in red. The contours correspond to a 0.5% and 3% relative error. The lighter-shaded contours indicate the 0.5% relative error, while the darker-shaded contours represents the 3% relative error. The best fits are marked with dots, and the black dot represents the best fit from the global fit.

4.4.4 Conclusion

In this section, a global fit was performed for the multimerization curve of αS using the nucleation self-assembly model. The fit yielded a cooperativity factor of $\sigma = 1.00 \cdot 10^{-2}$

and a critical concentration of $c_c = 316$ nM, indicating a cooperative multimerization mechanism. The fit matched the overall data set well, as well as each individual WT batch.

Chapter 5

The Molecular Basis of α-Synuclein Multimerization

In Chapter 4.4, a cooperative mechanism for the multimerization process of αS was identified. This raises the question on the types of molecular interaction that are involved in this cooperative multimerization. Therefore, it is interesting to look at αS in different environments and identify which types of interactions play a role. Based on the structural properties of αS, certain type of interactions are expected. The charged parts of the αS molecules are expected to participate in electrostatic interactions, while the NAC domain, which is highly hydrophobic, is likely involved in hydrophobic interactions and may also form cross β-structures through intermolecular hydrogen bonds during fibril formation. Additionally, the N-terminal domain can adopt an α-helical structure stabilized by intra-helical hydrogen bonds, which may also play a role in interactions.

5.1 Electrostatic Interactions

It is of interest to determine whether electrostatic interactions play a role in the cooperative behavior of αS multimerization. Therefore, αS multimerization MST experiments were performed in a solution where these interactions are reduced. In order to reduce electrostatic interactions, extra salt (NaCl) was added to the buffer, resulting in total salt concentrations of 125 and 250 mM in the samples. Total αS concentrations were varied from around 100 μM and lower. A 32-point MST was used, with ΔF_{norm} corrections applied without overlapping concentrations, and a dye concentration of 20 nM αS-A140C-AF488 was used. The blue LED was used for excitation. The self-assembly model (equation 2.1) was fitted to the data.

Results are shown in figures 5.1 and 5.2. Based on these figures, no significant difference is observed between the measurement with 125 mM salt added and those without extra salt (global fit of αS-WT in figures 4.12 and 4.13). The best fit is more cooperative. However, the error plots show that the error regions look almost identical. Therefore, it can be concluded that there is not much difference in cooperativity at 125 mM salt.
When inspecting the results for 250 mM salt, a difference is observed between the measurement with 250 mM salt added and without extra salt (global fit of αS-WT in figures 4.12 and 4.13). The best fit is less cooperative. The error plots also show differing error regions, indicating decreased cooperativity at 250 mM salt.
The reduced cooperativity in an environment where electrostatic charges are screened by salt ions indicates that the electrostatic interactions may play a role in the multimerization

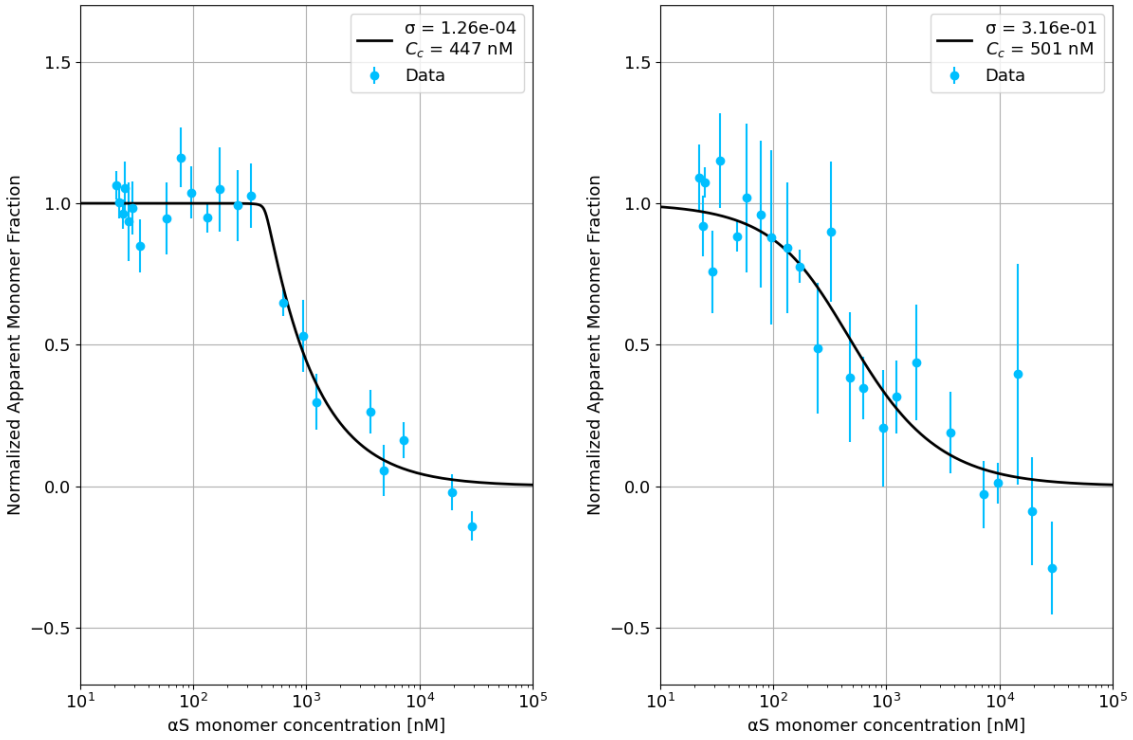

(A) NaCl concentration of 125 mM. (B) NaCl concentration of 250 mM.

FIGURE 5.1: Normalized apparent monomer fractions with a fit of the self-assembly model for salt concentrations of (A) 125 mM and (B) 250 mM.

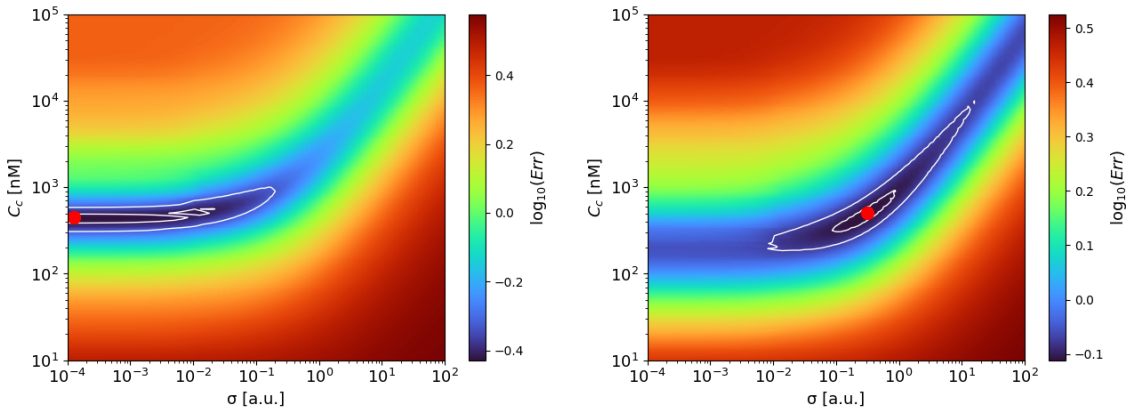

(A) NaCl concentration of 125 mM. (B) NaCl concentration of 250 mM.

FIGURE 5.2: Error plot for fitting errors of the self-assembly model for the fit of αS multimerization with salt concentrations of (A) 125 mM and (B) 250 mM.

of αS. They appear to be responsible for a part of the cooperativity in the multimerization without extra salt added, likely by increasing the energy barrier for multimer nucleation. This could rely on electrostatic repulsion of the net negative charge of the monomer. This consistent with other research where electrostatic interactions induced cooperativity and enhanced the polymerization rate for polypeptide-based macromolecules containing spatially organized α-helices [46].

Comparing salt conditions to cellular osmolarity, an osmolarity of approximately 300 mOsm/L is typical in cells [47], corresponding roughly to a concentration of 150 mM NaCl. The measurement at 125 mM NaCl is performed slightly below these physiological conditions, and no significant effect on cooperativity in αS multimerization was measured. In contrast, the measurement at 250 mM NaCl is performed at a higher osmolarity than in physiological conditions, resulting in a reduction in cooperativity. These findings suggest that under normal cellular conditions, αS multimerization is not strongly influenced by physiological salt concentrations. These results also indicate a transition between 125 mM and 250 mM salt, where the salt concentration starts to affect αS multimerization.

Before fitting, the data were normalized. The range from 0 to 1 of the normalized apparent monomer fraction corresponds to a difference in ΔF_{norm} of 4.2‰ and 2.9‰ for 125 mM and 250 mM salt, respectively. For 125 mM salt, the difference in ΔF_{norm} is very close to that without extra salt (4.0‰ on average). For 250 mM salt, the difference in ΔF_{norm} of 2.9‰ has decreased compared to that without extra salt. The interpretation of this decrease is open to discussion. For instance, a lower number of multimerization events could result in a smaller difference in ΔF_{norm}, as could a reduction in the size of the multimers formed.
The smaller difference in ΔF_{norm} for 250 mM salt could indicate that fewer multimers were formed, or that the multimers were smaller in size. This may suggest that the intermolecular electrostatic bonds normally have a stabilizing effect on multimers, and that their absence leads to either fewer multimers being formed or a reduction in multimer size.

5.2 Hydrophobic Interactions

It is of interest to determine whether hydrophobic interactions play a role in the cooperative behavior. Therefore, αS multimerization experiments in MST were performed in a solution where these interactions are reduced.
In order to reduce the hydrophobic interactions, 1,6-hexanediol was added to the buffer. An αS-WT titration was used with total αS concentrations ranging from around 100 μM and lower. A 32-point MST was used, with ΔF_{norm} corrections applied without using overlapping concentrations, and a dye concentration of 20 nM αS-A140C-AF488. Experiments were performed for 1,6-hexanediol concentrations of 5% v/v and 10% v/v. The self-assembly model (equation 2.1) was fitted to the data.

Results are shown in figures 5.3 and 5.4. Based on these figures, a slight difference is observed between the measurement with 5 % v/v 1,6-hexanediol added and those without (global fit WT in figures 4.12 and 4.13). The best fit is slightly less cooperative than the global fit. The error plot shows a small difference in comparison to that of the WT. However, these differences are still minor, and there is a considerable overlap in the error regions indicated by the contours. Therefore, it can be concluded that there is no significant change in cooperativity for the 5% v/v 1,6-hexanediol case.
Figures 5.3(B) and 5.4(B) show no difference between these measurements and the WT control (figure 4.12). Both show exactly the same optimal cooperativity factor of $1.00 \cdot 10^{-2}$ for the fit and a comparable critical concentration (355 nM in this case versus 316 nM for the WT control). Additionally, the fitting errors are almost identical to those of the WT control (figure 4.13). Therefore, it can be concluded that the addition of 1,6-hexanediol

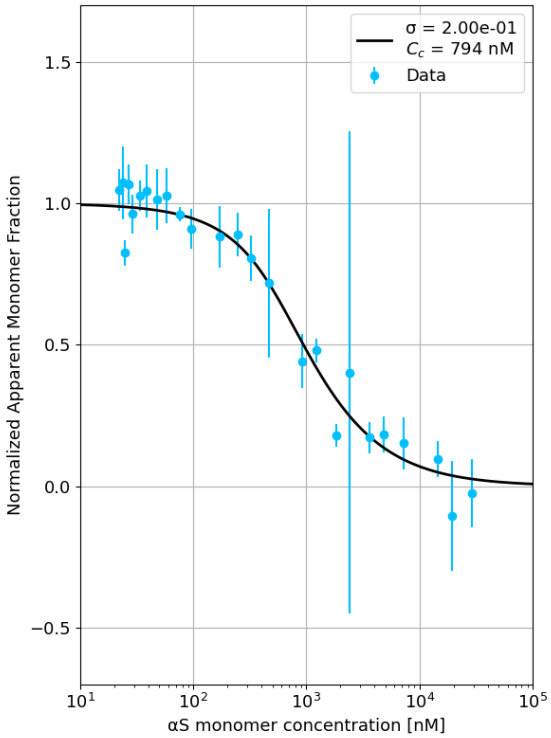

(A) 1,6-hexanediol concentration of 5% v/v.

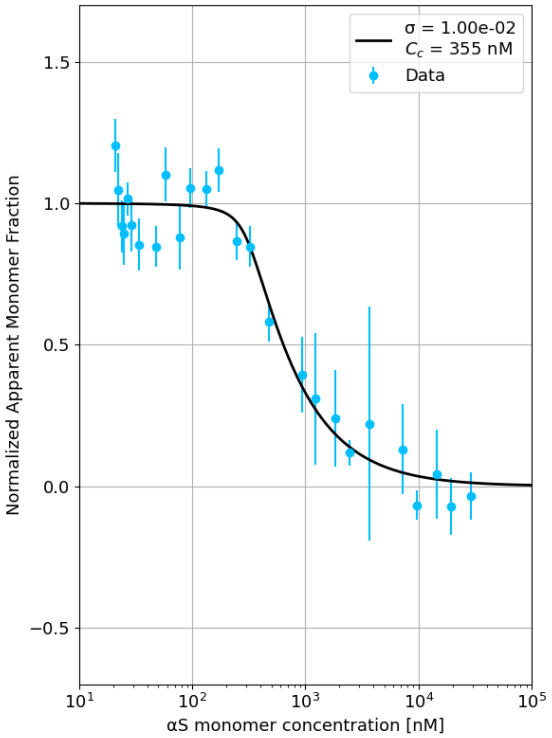

(B) 1,6-hexanediol concentration of 10% v/v.

FIGURE 5.3: Normalized apparent monomer fractions with a fit of the self-assembly model for 1,6-hexanediol concentrations of (A) 5% v/v and (B) 10% v/v.

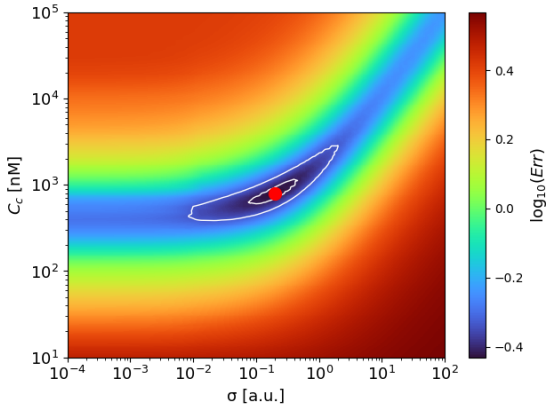

(A) 1,6-hexanediol concentration of 5% v/v.

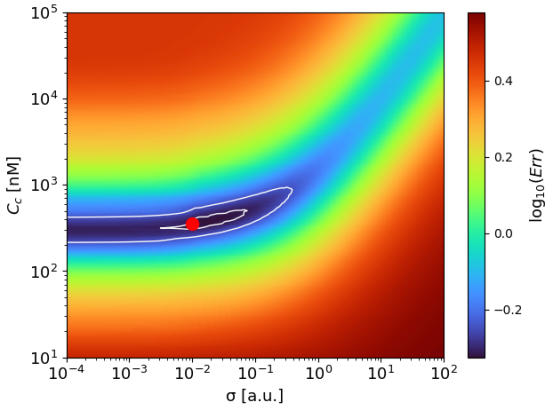

(B) 1,6-hexanediol concentration of 10% v/v.

FIGURE 5.4: Error plot for fitting errors of the self-assembly model for the fit of αS multimerization with 1,6-hexanediol concentrations of (A) 5% v/v and (B) 10% v/v.

has no significant impact on the cooperativity of the αS multimerization process.

The normalized range from 0 to 1 of the normalized apparent monomer fraction corresponds

to a difference in ΔF_{norm} of 4.8‰ and 4.0‰ for 5% v/v and 10% v/v 1,6-hexanediol, respectively. For 5% v/v 1,6-hexanediol, the difference in ΔF_{norm} is slightly higher than the control (4.0‰ on average), but not significantly when comparing it to the WT batches individually. For 10% v/v 1,6-hexanediol, the difference in ΔF_{norm} of 4.0‰ is exactly the same as the average of the WT control measurement.

Based on the hydrophobic nature of the NAC domain and its established role in aggregation, hydrophobic interactions were expected to play an important role in αS multimerization. However, MST experiments showed no significant changes in terms of cooperativity, critical concentration, and difference in ΔF_{norm}. It is important to note that MST measures only a few multimerization characteristics. Therefore, it could be that other multimerization characteristics like the rate of assembly, the extent of multimer formation, or equilibrium of the multimers may have been affected, but were not detectable using this technique.

5.3 Hydrogen Bonds

It is of interest to determine whether H-bonds play a role in the cooperative behavior. Therefore, αS multimerization experiments using MST were performed in a solution where these interactions are reduced. In order to reduce the number of H-bridges formed, guanidine hydrochloride (GuHCl) was added to the buffer. GuHCl is often used for the unfolding of proteins [48] Dissolved GuHCl, with a concentration of 30 mg/mL, was added to the αS-WT stock ($\sim$250 μM). The mixture was incubated for one hour at room temperature and filtered using a Zebaspin (7 kDa MWCO, Thermo Fisher Scientific). After filtration, some GuHCl remained in the sample, but the exact concentration was unknown. Using the filtered αS-WT, a dilution series was prepared for MST, and MST measurements were performed. A 32-point MST is used, with ΔF_{norm} corrections applied without using overlapping concentrations, and a dye concentration of 20 nM αS-A140C-AF488. The blue LED was used for excitation. The self-assembly model (equation 2.1) was fitted to the data.

Results are shown in figures 5.5 and 5.6. Based on these figures, a difference is observed between the measurement with guanidine hydrochloride added and those without (global fit WT in figures 4.12 and 4.13) in terms of cooperativity and critical concentration. The most optimal fit is less cooperative and has a higher critical concentration. When looking at the error plots, the error regions also differ, with error regions pointed more toward the larger cooperativity factors. Therefore, it can be concluded that cooperativity decreases in the presence of GuHCl. This may be explained by the promotion of an alternative multimerization pathway. This could arise from the disruption of intermolecular β-sheet formation, or changes in intramolecular hydrogen bonds. These changes may reduce the energy barrier of the nucleation step, resulting in a lower cooperativity factor.
Before fitting, the data were normalized. The range from 0 to 1 of the normalized apparent monomer fraction corresponds to a difference in ΔF_{norm} of 4.8‰. This difference in ΔF_{norm} has not significantly changed compared to that without GuHCl.
In conclusion, GuHCl reduces cooperativity in αS multimerization, but has no impact on the differences in ΔF_{norm}.

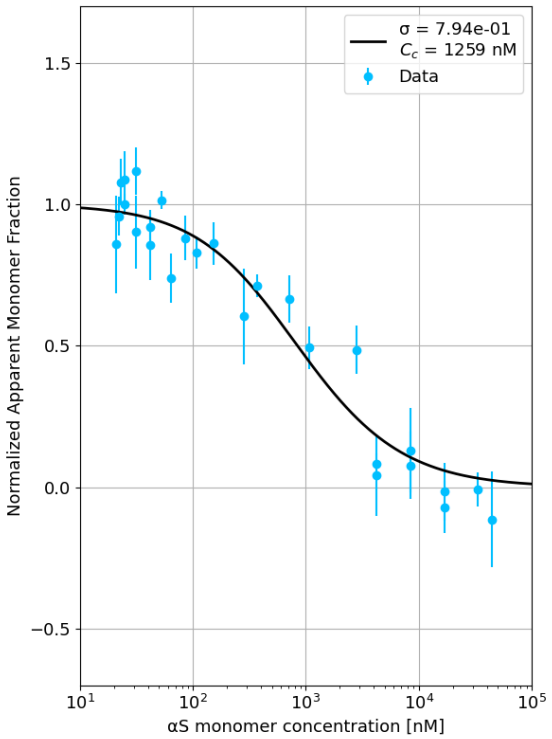

FIGURE 5.5: Normalized apparent monomer fractions of αS multimerization with a fit of the self-assembly model in the presence of GuHCl.

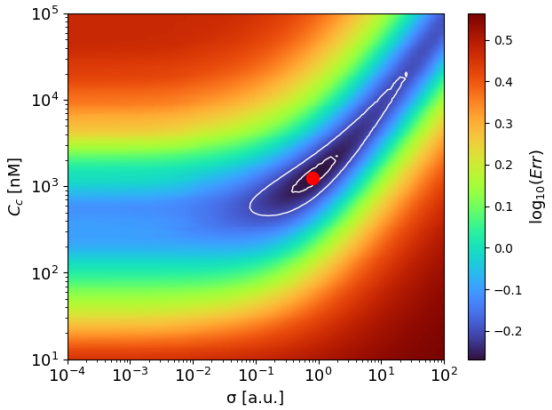

FIGURE 5.6: Error plot for fitting errors of the self-assembly model for the fit of αS multimerization in the presence of GuHCl.

Chapter 6

Effect of the Addition of Different Isoforms of 14-3-3 on the Multimerization of α-Synuclein Monomers

Previously at NBP, a reducing effect on cooperativity was shown upon the addition of 14-3-3τ to multimerizing αS [7]. Therefore, it was decided to investigate this further and test the effect of different concentrations 14-3-3τ on αS multimerization. Next to that, it is of interest to compare different isoforms of 14-3-3 with the τ isoform. This chapter discusses the findings gathered during the thesis project.

6.1 14-3-3τ

MST experiments (32-point, no overlapping concentrations) were performed for αS-WT dilution series were the highest WT concentrations were $\sim$100 μM. Experiments with a 14-3-3τ concentration of 0.67 μM were performed first. Each sample of the dilution series had a αS-A140C-AF488 concentration of 20 nM. The blue LED was used for excitation. The self-assembly model (equation 2.1) was fitted to the data.

Results for a 14-3-3τ concentration of 0.67 μM are shown in figures 6.1(A) and 6.2(A). The differences in ΔF_{norm} corresponding to the normalized apparent monomer fraction is 2.4‰. From this results, it can be concluded that for this 14-3-3τ concentration, there are changes in the multimerization process in terms of a reduced cooperativity and a decrease in the difference in ΔF_{norm}, compared to the WT measurements (figures 4.12 and 4.13). The decrease in difference in ΔF_{norm} may indicate an overall decrease in multimerization events or a decreased size of the multimers, as discussed in previous chapter.

To see the influence of 14-3-3τ concentration, this experiment was repeated with 14-3-3τ concentrations of 2 and 5 μM. Results for these experiments are shown in figures 6.1(B) and (C), and 6.2(B) and (C). The differences in ΔF_{norm} corresponding to the normalized apparent monomer fraction are 1.2‰, and 2.3‰ for 14-3-3τ concentrations of 2 μM, and 5 μM, respectively. For these two concentrations, it can be concluded that there are changes in the multimerization process in terms of cooperativity and the difference in ΔF_{norm}, compared to the WT measurements (figures 4.12 and 4.13).

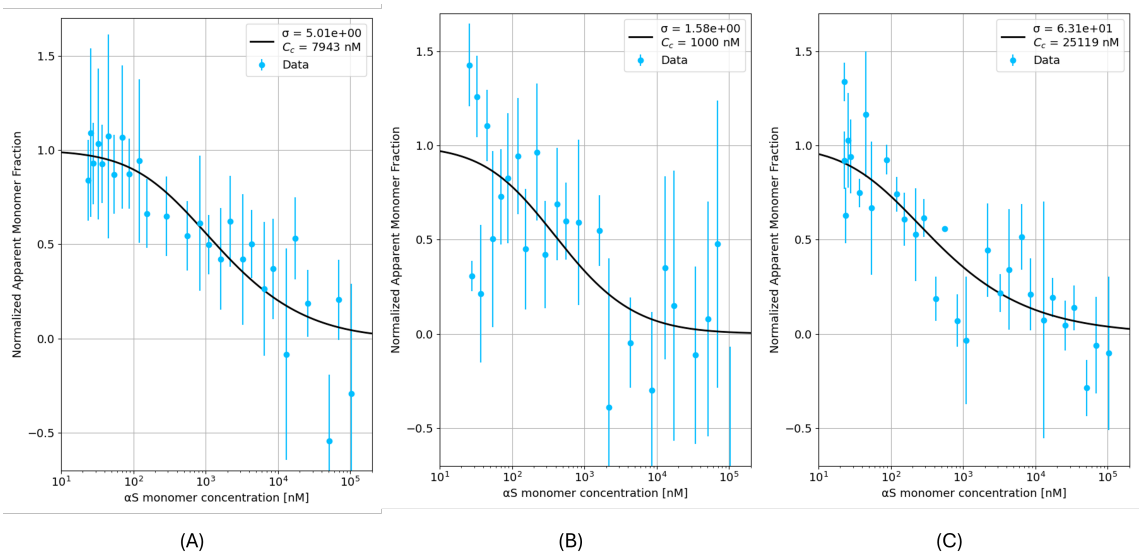

FIGURE 6.1: Normalized apparent monomer fraction for αS multimerization in the presence of the 14-3-3τ isoform, including a fit of the self-assembly model, for concentrations of (A) 0.67 μM, (B) 2 μM, and (C) 5 μM 14-3-3τ.

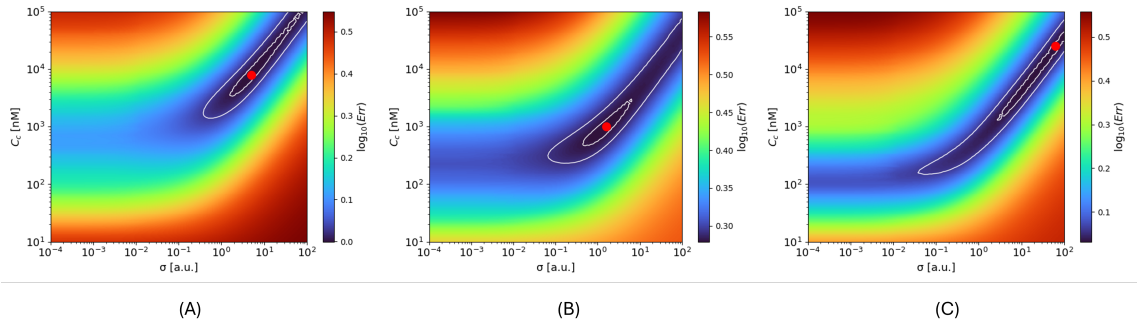

FIGURE 6.2: Error plot for fitting errors of the self-assembly model for the fit of αS multimerization in the presence of (A) 0.67 μM, (B) 2 μM, and (C) 5 μM 14-3-3τ isoform.

The cooperativity is reduced, similarly as for the 14-3-3τ concentration of 0.67 μM. However, the data do not follow the fit well, and the error bars of the data points are quite large, so it can not be said with certainty that the cooperativity is lower in these cases, especially for the concentration of 2 μM.
Based on the difference in ΔF_{norm} corresponding to the normalized apparent monomer fraction, it is clear that this value has decreased from 4‰ (WT-control) to 1.2‰, and 1.9‰ for 14-3-3τ concentrations of 2, and 5 μM, respectively. This may indicate an overall decrease in multimerization events or a decreased size of the multimers, as discussed in previous chapter.
Although there is a significant uncertainty in the fit at a 14-3-3τ concentration of 5 μM, making it difficult to draw strong conclusions, a slight difference is observed between the measurements at 0.67 μM and 5 μM 14-3-3τ concentration in terms of cooperativity. There is a decrease in cooperativity, with an increase in critical concentration. Note that for increased cooperativity, the error region for c_c becomes larger. This is typical for non-cooperative multimerization, which lacks a distinct c_c. There is not a clear difference

visible between the measurements at different 14-3-3τ concentrations in terms of difference in ΔF_{norm}. This may indicate that there is no difference in extent of multimerization or in the size of the multimers formed. In conclusion, a decrease in cooperativity in αS multimerization was observed when 14-3-3τ was added, for all concentrations of 14-3-3τ used. Additionally a decrease in the difference in ΔF_{norm} was observed for all measurements.

6.2 14-3-3γ

MST experiments (32-point, no overlapping concentrations) were performed for αS-WT dilution series were the highest WT concentrations were $\sim$100 μM. Each sample had a 14-3-3γ concentration of 2 μM and a αS-A140C-AF488 concentration of 20 nM. The blue LED was used for excitation. The self-assembly model (equation 2.1) was fitted to the data.

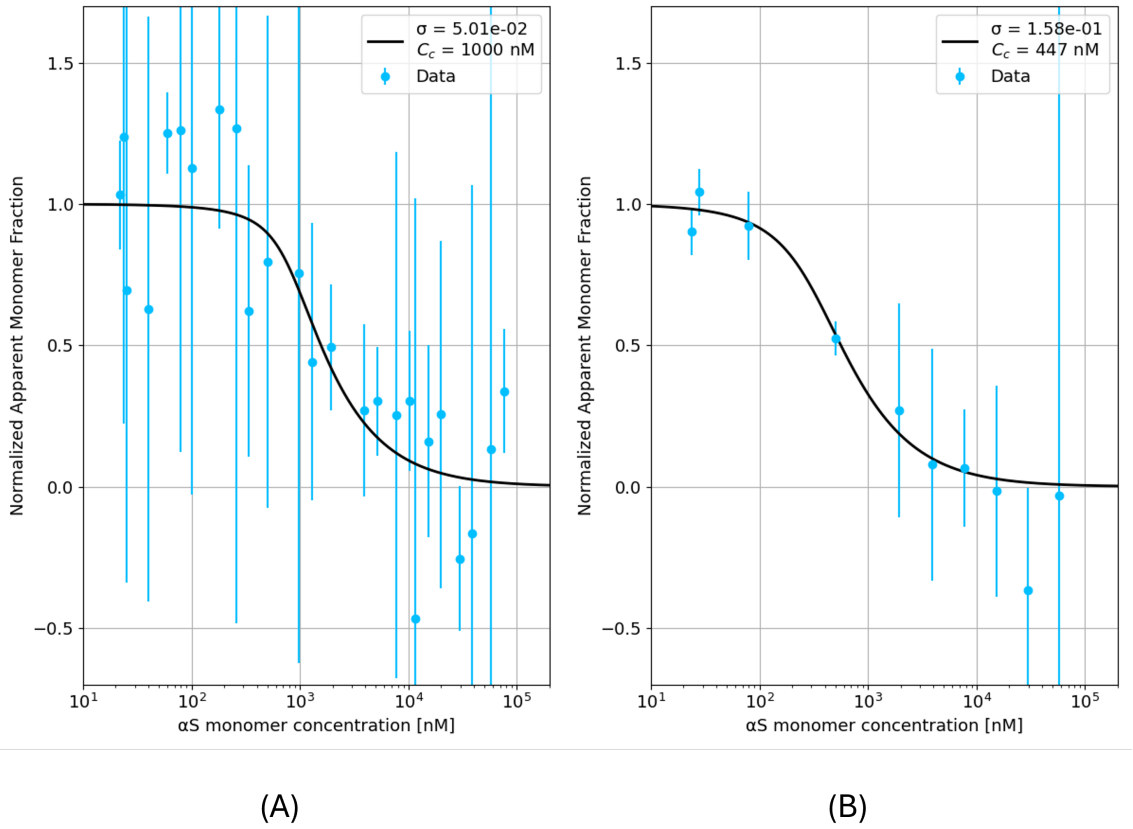

FIGURE 6.3: Normalized apparent monomer fraction for αS multimerization in the presence of 2μM 14-3-3γ isoform, including a fit of the self-assembly model for (A) data with 2 MST runs (32 concentrations) and (B) only for the first MST run (16 concentrations). This run shows much less variation.

Results for 32-points MST are shown in figures 6.3(A) and 6.4(A), no conclusions can be drawn regarding the impact of 14-3-3γ on the cooperativity of αS multimerization, as there is too much variation in the data to get a reliable fit. Inspecting the data of the first 16-point run and the second 16-point run showed that almost all outliers originated from the second run, indicating that something went wrong during the measurement.
The first MST run of the measurement provides data with less outliers, which can be fitted

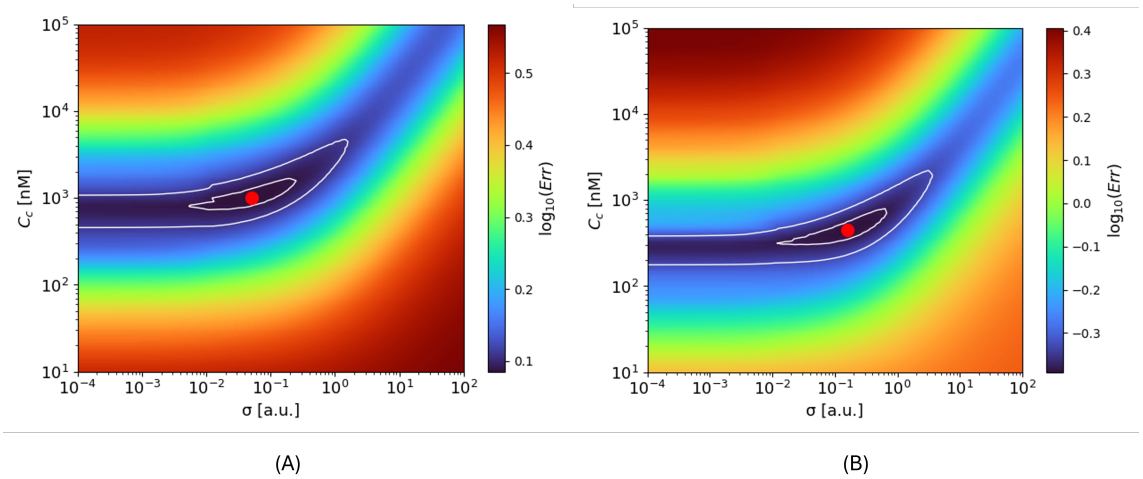

FIGURE 6.4: Error plot for fitting errors of the self-assembly model for the fit of αS multimerization in the presence of 2μM 14-3-3γ isoform for (A) data with 2 MST runs (32 concentrations) and (B) only for the first MST run (16 concentrations).

with the nucleation self-assembly model (figures 6.3(B) and 6.4(B)). This fit shows a slight reduction in the cooperativity compared to αS-WT multimerization (figures 4.12 and 4.13) and a small increase in critical concentration. Unfortunately, there is a limited number of data points, especially in the slope region, resulting is a less reliable fit.

The difference in ΔF_{norm} corresponding to the normalized apparent monomer fraction is 1.7‰. This value shows that something is changing in the multimerization process compared to αS WT multimerization (figures 4.12 and 4.13) in terms of a decreased difference in ΔF_{norm} corresponding to the normalized apparent monomer fraction. This value has decreased from 4‰ (WT-control) to 1.7‰ for a 14-3-3γ concentration of 2 μM. This may indicates an overall decrease in multimerization events or a decreased size of the formed multimers, as discussed in previous chapter.

6.3 14-3-3σ

MST experiments (32-point, no overlapping concentrations) were performed for αS-WT dilution series were the highest WT concentrations were ~100 μM. Each sample had a 14-3-3σ concentration of 2 μM and a αS-A140C-AF488 concentration of 20 nM. The blue LED was used for excitation. The self-assembly model (equation 2.1) was fitted to the data.

Results are shown in figures 6.5 and 6.6. The difference in ΔF_{norm} corresponding to the normalized apparent monomer fraction is 1.9‰. The addition of 14-3-3σ to multimerizing αS shows a change in the multimerization process in terms of cooperativity and difference in ΔF_{norm} value compared to αS-WT multimerization without 14-3-3σ. The difference in ΔF_{norm} corresponding to the normalized apparent monomer fraction has decreased from 4‰ (WT-control) to 1.9‰ for a 14-3-3σ concentration of 2 μM. This may indicate an overall decrease in multimerization events or a decrease in size of the multimers.
Based on figures 6.5 and 6.6, it becomes clear that αS multimerization becomes less cooperative in the presence of 14-3-3σ. This is reflected in the cooperativity factor of 2.51 and a higher critical concentration of 1122 nM with large error regions.

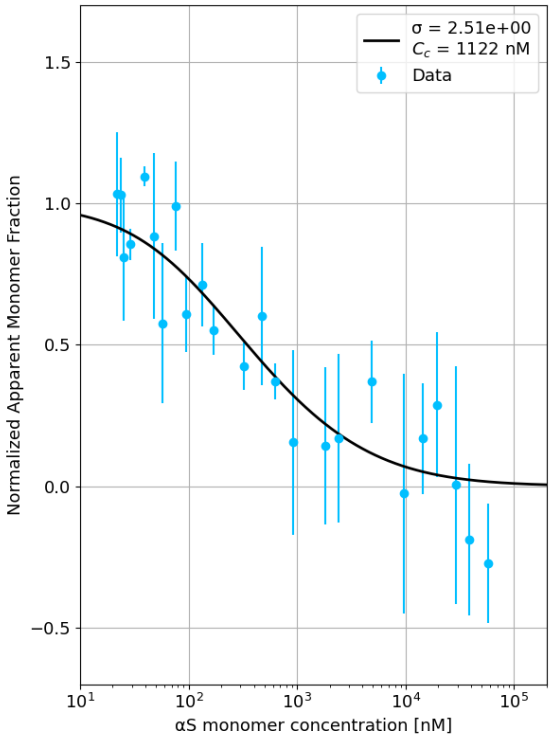

FIGURE 6.5: Normalized apparent monomer fraction for αS multimerization in the presence of 2μM 14-3-3σ isoform, including a fit of the self-assembly model.

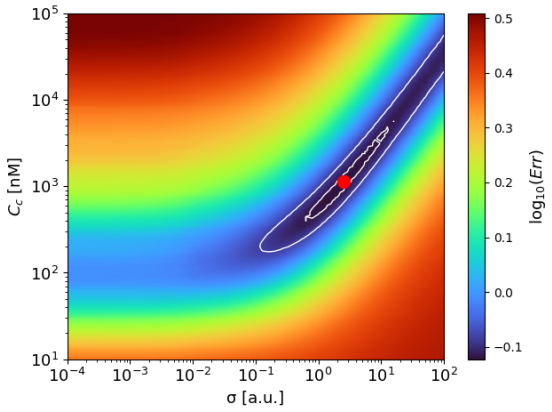

FIGURE 6.6: Error plot for fitting errors of the self-assembly model for the fit of αS multimerization in the presence of 2μM 14-3-3σ isoform.

6.4 Conclusion and Discussion

For the experiments on αS multimerization in the presence of different isoforms of 14-3-3, decreased cooperativity was found for the τ and σ isoforms. This indicates a lowering of the energy barrier for nucleation.
In Chapter 2, it was discussed that the addition of 14-3-3 to multimerizing αS could result in reduced cooperativity, due to the formation of mixed multimers through a non-cooperative mechanism, rather than αS-only multimers formed through a cooperative mechanism. It was mentioned that this could lead to the formation of more multimers, which are smaller

in size. These findings align with the results obtained in this study, which means that the reduced difference in ΔF_{norm} between the initial and final multimerization plateau may be related to the size of the multimers formed.
The results for the 14-3-3τ isoform are consistent with previous research [7], in which a reduction in cooperativity in αS multimerization was also reported upon addition of 14-3-3τ. Although the exact concentration used in that study (3.5 μM) differs from those used here, the critical concentration (c_c)of 1778 nM and cooperativity factor (σ) of 1.26 are of the same order of magnitude as those found in this study.
No prior studies are available on the impact of the σ and γ isoforms on cooperativity. Given the structural similarity among 14-3-3 isoforms, it is expected that the roles of the σ and γ isoforms are similar to that of τ. For 14-3-3σ, a reduction in cooperativity was also observed, with a comparable cooperativity factor and critical concentration. For the γ isoform, however, the measurement was suboptimal. The first run, which included 16 concentrations gave the best indication of the multimerization process. A slight reduction in cooperativity was observed for this measurement. However, due to the limited number of concentrations measured in the transition region, the resulting fit was less reliable, as single data points had a significant influence on the fit. Repeating these measurements may yield more reliable insights.

Chapter 7

14-3-3-τ Interaction with α-Synuclein Oligomers

The αS multimers formed in MST experiments are probably kinetically trapped intermediates, that can develop into amyloid fibrils. In Chapter 6, interaction between αS and 14-3-3 was observed in very early stages of multimerization. This raises the question whether 14-3-3 also interacts with the kinetically trapped intermediates formed in multimerization without 14-3-3 present. Investigating the interaction of 14-3-3 with a kinetically trapped species is complicated. However, the kinetically trapped intermediates are known to be comparable in size to that of a relatively stable oligomer; an αS 30-mer species, which is likely slightly smaller than the kinetically trapped intermediates. This species is also largely unstructured, similar to the kinetically trapped intermediates [7]. It is expected that this species interacts with 14-3-3 in a similar way as the kinetically trapped intermediates. Therefore, it serves as a suitable model for studying such interactions, and it is of interest to determine whether there is an interaction between αS 30-mers and 14-3-3τ.
To investigate this, multiple techniques (MST, FCS and confocal imaging) were used. This chapter discusses the results of each technique separately and ends with an overall conclusion based on all three techniques.

7.1 MST

MST enables investigation of molecular interaction between a target and its ligand. Therefore, this technique is suitable for studying the interaction between αS 30-mers and 14-3-3τ. In the MST experiment, the T-jump region was the primary focus rather than the 5 to 30 seconds region of the MST traces, because the temperature sensitivity of the dye can change in the case when labeled αS 30-mers bind to 14-3-3τ. In this T-jump region, diffusion plays a minor role. Due to stickiness of the dye, identified by looking at the fluorescence intensity profiles across the capillaries (similar fluorescence profile as in figure 4.1(A)), it is expected that this T-jump is less affected by stickiness, since diffusion does not play a role yet.
MST experiments were performed using αS 30-mers (labeled with AF568) and a titration of 14-3-3τ. A 16-point MST was used with 14-3-3τ concentration ranging from $\sim$100 μM and below. The αS 30-mer concentration was 73 nM (monomer equivalent) and the dye concentration was 16 nM AF568 (dye monomer equivalent). The green LED was used for excitation. For the T-jump, the region from -1 to 0 s was compared to the region from 0.5 to 1.5 s. Because the T-jump region was used, it was not possible to calculate standard deviations for the measurement using early, mid, and late regimes, as F_{norm} does not

remain constant during the T-jump, but decreases.

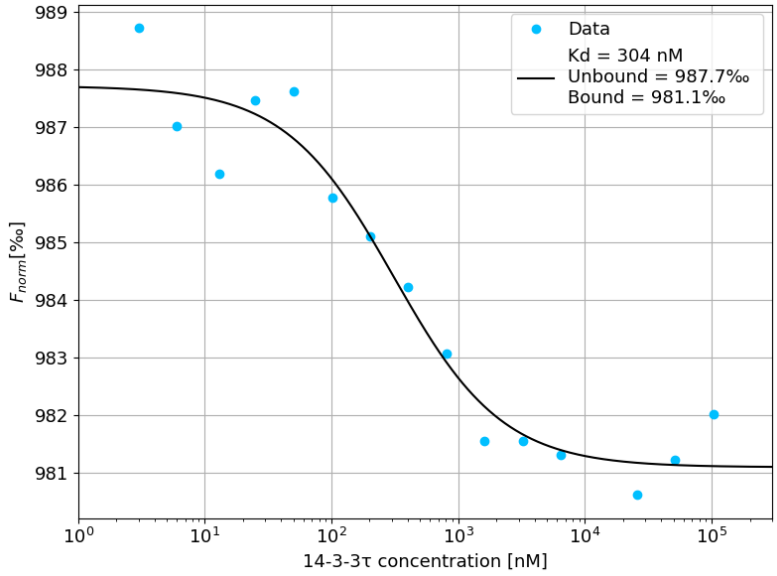

FIGURE 7.1: Normalized bound fraction for αS 30-mers with 14-3-3τ, including a fit of the K_D model.

Results of the MST response for the T-jump are given in figure 7.1. The K_D model is fitted to the data. The Hill model was also fitted, but gave n_{Hill} value of around 1. Therefore, a simple 1:1 binding stoichiometry is assumed and the K_D model is the most suitable. The standard errors of the fit were calculated by taking the covariance matrix of the fit and taking the square root of the diagonal elements. This gave fitted values of K_D = 304 $\pm$ 96 nM and unbound and bound values of 987.7 $\pm$ 0.4‰ and 981.1 $\pm$ 0.3‰.
Based on figure 7.1, it can be concluded that there is interaction between αS 30-mers and 14-3-3τ. This interaction indicates that 14-3-3τ influences the oligomeric phase. Combined with the results of Chapter 6, interactions are observed for 14-3-3τ with other αS multimers as well as 30-mers. This indicates that 14-3-3τ does not interact with a specific αS multimer or size, but rather exhibits a more general interaction pattern. This shows that 14-3-3 could interfere in multiple stages of multimerization and could possibly prevent the formation of a critical nucleus for fibril formation in different early stages.
It should be noted that due to sticking of the αS 30-mers to the capillary walls, the effective concentration 30-mers in the measurement volume is lower than indicated, which may have influenced the results, especially at low concentrations of 14-3-3τ. Furthermore, a false-positive binding curve could have been measured. At low concentrations of 14-3-3, the glass surface could be occupied by (part of) the 30-mers. When increasing the concentration of 14-3-3τ, the 14-3-3τ molecules could replace αS 30 mers at the surface, and changing the 30-mer concentration in solution. This could have lead to a false-positive binding curve. It would be best to prevent this sticky behavior at all, without changing the behavior of αS 30-mers and 14-3-3τ. In this case it would might help to use Monolith Premium capillaries (MO-K025), having a surface that is covalently coated with polymers to prevent protein sticking, and see if the obtained binding curve is similar. Additionally, if the observed sticking of labeled αS 30-mers to the capillary walls is dye-mediated, it is possible that the interaction between 14-3-3τ and αS 30-mers is also (partly) dye-mediated. This possible dye-mediated behavior can be assessed by using αS labeled with alternative dyes and repeating the experiment.

Sample	D_1 $[\mu m^2/s]$	D_2 $[\mu m^2/s]$
14-3-3τ direct	147 ± 19	24 ± 1.4
14-3-3τ after 1h	160 ± 3.1	–
αS 30-mers	26 ± 0.28	–
14-3-3τ and αS 30-mers	11 ± 1.6	73 ± 2.8

TABLE 7.1: Diffusion coefficients and corresponding errors for the measured samples.

7.2 FCS

In previous paragraph, indications for interaction between αS 30-mers and 14-3-3τ chaperones were found in MST. However, it can not be excluded that the obtained binding curve was false-positive due to sticking of labeled proteins to the capillary surface. FCS can measure interaction by mapping diffusion in and out of a confocal volume. The diffusion coefficients determined using this technique do not depend on surface processes. Therefore, this technique is very suitable to validate the interaction between αS 30-mers and 14-3-3τ. FCS could not be performed on the kinetically trapped αS intermediates because they exist in an equilibrium with αS monomers, where the equilibrium lies more toward the monomeric form. As a result, only a very small fraction of αS is present as kinetically trapped αS intermediates, which is not measurable in FCS. In contrast, αS 30-mers are a stable species that can be isolated, making them suitable for FCS measurements.
By fitting FCS autocorrelation curves for samples containing αS 30-mers, 14-3-3τ or both, information can be gathered on the diffusion coefficients of proteins in samples. By comparing samples with one single protein with a sample in which both proteins are present, interactions can be mapped.

For the FCS experiments, 14-3-3τ-AF647 and αS 30-mers labeled with AF568 were used. Fluorescence fluctuation time traces were recorded and analyzed.

The following samples were measured:

- 10 nM 14-3-3τ-AF647, measured with 636 nm laser (measured directly and after 1 hour).
- 2.4 nM αS 30-mers (labeled with AF568), measured with a 560 nm laser, with the sample placed on an αS passivated cover glass.
- 37 nM αS 30-mers (labeled with AF568) and 20 nM 14-3-3τ-AF647, measured with a 636 nm laser, with the sample placed on an αS passivated cover glass.

Experiments for 14-3-3τ were repeated after one hour, due to the presence of numerous high spikes in the fluorescence time trace, observed during measurements, likely caused by larger 14-3-3τ aggregates. Autocorrelation curves were calculated and fitted using the SymPhoTime software. For all samples, a single triplet state was included in the fitting model. Depending on the sample, the model was fitted for one or two diffusing species.

The resulting normalized autocorrelation curves are shown in figure 7.2, along with the corresponding errors and fits using the extended triplet (3D) diffusion model. The resulting diffusion coefficients of the fits are summarized in table 7.1.

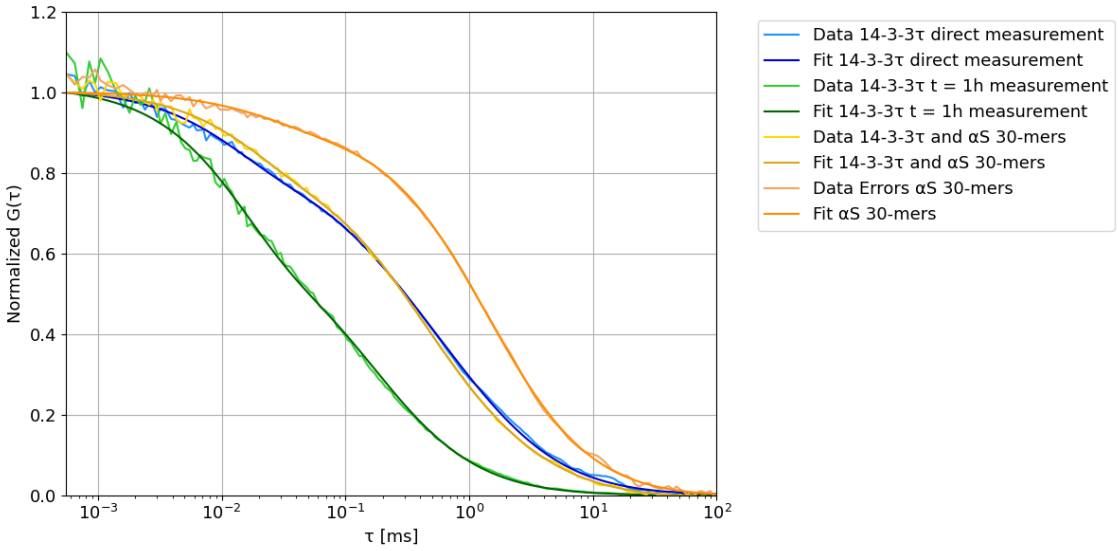

FIGURE 7.2: Normalized autocorrelation curves for αS 30-mers, 14-3-3τ, and the combination of both, including fits using the extended triplet (3D) model.

7.2.1 14-3-3τ

When measuring 14-3-3-τ using FCS, an autocorrelation curve was found that is best fitted by a two-species model with a triplet state, significantly better than a single-species model with a triplet state. This indicates that, in addition to dimeric 14-3-3τ, larger aggregates were also detected.
Furthermore, during the measurements, fluorescent time traces already indicated that the direct measurement of 14-3-3τ showed high-intensity spikes, likely caused by larger 14-3-3τ aggregates. These high peaks correspond to multiple fluorescent molecules passing through the confocal volume at the same time. The high spikes could also potentially be caused by Christmas-tree labeling of 14-3-3τ. However, this is less likely, as the aggregating behavior of 14-3-3 is also reflected in the fit of the autocorrelation curve 7.2, where a two-species diffusion model was fitted. One species has a diffusion coefficient of 24 $\mu m^2/s$, corresponding to a slower diffusing species, likely aggregates of 14-3-3τ. The other species has a diffusion coefficient of 147 $\mu m^2/s$, corresponding to a faster diffusing species, which is probably dimeric 14-3-3τ.
This result is consistent with the measurement of 14-3-3τ taken after 1 hour, where only a single diffusing species with a diffusion coefficient of 160 $\mu m^2/s$ was measured. This value is close to that dimeric 14-3-3τ measured in the direct measurement and likely corresponds to the same dimeric form of 14-3-3τ.
The diffusion coefficient of the 14-3-3τ dimers seems a bit high. An estimation of the diffusion coefficients based on the molecular weight of proteins can be made based on the empirical equation of Young [49] for globular proteins, which is based on the Stokes-Einstein equation:

$$D = 8.34 \times 10^{-8}(\frac{T}{\eta M^{\frac{1}{3}}}) \tag{7.1}$$

With D the diffusion coefficient in cm^2/s, T the absolute temperature in Kelvin, η the dynamic viscosity in centipoise (cP), and M the molecular weight in Daltons (Da). This equation can be used to make an approximation of the diffusion coefficient of 14-3-3τ.

Assuming a room temperature of 20°C, water as solvent, and assuming that 14-3-3τ is present as dimers, with a molecular weight of approximately 60 kDa [50], equation 7.1 gives a diffusion coefficient of approximately 62 $\mu m^2/s$ for 14-3-3τ dimers. This is much lower than the fitted diffusion coefficient. A possible explanation is blinking of the fluorophore, resulting is a lower measured passage time through the confocal volume.
The aggregates measured in the direct measurements have a diffusion coefficient of 24 $\mu m^2/s$. Using equation 7.1, this corresponds to a molecular weight of 1050 kDa, equivalent to 35-mers of 14-3-3.

The presence of aggregates when measured directly, but not after one hour, might be explained by the dissociation of the aggregates over time due to dilution. The 14-3-3τ stock solution has a high concentration ($\sim$ 6 μM) and is therefore more prone to aggregation. The stock solution is diluted immediately before the experiment. This sudden dilution may lead to gradual disassembly of aggregates. This can explain why both dimers and aggregates of 14-3-3τ are present in the direct measurement.

7.2.2 αS 30-mers

For the measurement of αS 30-mers, the autocorrelation curve was fitted with a one-species diffusion model including a triplet state, resulting in a diffusion coefficient of 26 $\mu m^2/s$. This value is lower than that of 14-3-3τ, which is expected, as an αS 30-mer (MW of about 432 kDa [51]) is larger than a 14-3-3τ molecule (MW of about 30 kDa [50]), which results in smaller diffusion coefficients. Furthermore, equation 7.1 can be used to get an estimation of the diffusion coefficient of αS 30-mers. This gives a diffusion coefficeint of 32 $\mu m^2/s$. However, the equation of Young is for globular proteins. Since αS is an IDP, this equation may underestimate the solvent radius and overestimates therefore the diffusion coefficient. The actual diffusion coefficient is probably a bit lower. This matches nicely with the fitted diffusion coefficient of 26 $\mu m^2/s$.

7.2.3 14-3-3τ and αS 30-mers

In measurements where both 14-3-3τ and αS 30-mers were present, the AF647 fluorophore attached to 14-3-3τ was tracked. In this case, the autocorrelation curve was best fitted by a two-species model including a triplet state, significantly better than with a single-species model with a triplet state, which is expected if 14-3-3τ and 30-mers interact. The two-species model gave two diffusion coefficients. The first diffusion coefficient of 11 $\mu m^2/s$ is lower than that of both 14-3-3τ and αS 30-mers when measured individually. This suggests interaction between the two proteins, as a complex formed by their association would diffuse slower than either protein alone. Alternatively, the species with a diffusion coefficient of 11 $\mu m^2/s$ could correspond to large aggregates of 14-3-3τ alone, implying no interaction with αS 30-mers. However, this explanation is less likely, as this diffusion coefficient is substantially lower than that of the aggregates in the direct 14-3-3τ-only-experiment. This would imply that such aggregates are significantly larger, which is improbable under comparable experimental conditions.
When calculating the corresponding molecular weight using equation 7.1, a molecular weight of 10.9 MDa is found. Assuming that the combined complex consists of one αS 30-mer and multiple 14-3-3τ proteins, 349 14-3-3τ molecules are involved. This looks like very much 14-3-3 in comparison to the amount of αS, therefore it may suggest that clusters of multiple αS 30-mers in combination with 14-3-3τ molecules have formed.

The second diffusion coefficient in the combined measurement is 73 $\mu m^2/s$. This value is lower than that measured of 14-3-3τ dimers but higher than that of αS 30-mers, indicating that this species only contains 14-3-3τ. Based on the diffusion coefficient measured in the 14-3-3τ-only experiment, this species would be an aggregate. However, the estimated diffusion coefficient of 14-3-3 dimers using equation 7.1 is close to that observed in this measurement, indicating that this species is likely 14-3-3 dimers. The diffusion coefficient could also represent a mixture of dimers and aggregates of different sizes, resulting in an average diffusion coefficient of 73 $\mu m^2/s$. During the experiments, there was no excess of αS 30-mers. Likely because of this, not all 14-3-3τ is bound to αS 30-mers, and hence two diffusion species were observed. If already about two 14-3-3 molecules were bound to each αS 30-mer, all 14-3-3 would be bound to an αS 30-mer. However, still unbound 14-3-3 is measured, and the diffusion coefficient corresponding to complexes of 14-3-3τ and 30-mers indicates that many more than two 14-3-3τ molecules are bound per αS 30-mer.

This shows that not all αS 30-mers are bound to 14-3-3τ and the part that is bound often has multiple 14-3-3τ molecules attached. This suggests that the initial binding of a 14-3-3τ molecule to an αS 30-mer may facilitate the subsequent binding of additional 14-3-3τ molecules, indicating cooperativity in the binding of 14-3-3τ to αS 30-mers. Alternatively, it is possible that multiple 14-3-3τ molecules bind to a 30-mer, because 14-3-3τ is already present in the form of a cluster prior to binding, and the cluster binds as a whole.

7.3 Confocal Imaging

In the previous sections, indications for interaction between αS 30-mers and 14-3-3τ were obtained. This raises the question whether this interaction could also be observed in confocal imaging by identifying colocalization. Therefore, confocal imaging of 14-3-3τ and αS 30-mers was performed.

The set-up is described in Chapter 3. Captures were made using the 636 nm and 560 nm lasers. Measurements for both wavelengths were performed directly after each other. A laser power of 20k a.u. is used, corresponding to an optical power of approximately 30-40 μW.

For the experiments, very low concentrations of proteins were used to be able to see single molecules. A sample was prepared with a 14-3-3τ concentration of 100 pM and an αS 30-mer concentration of 18 pM. For each sample, a 20 μL droplet was placed on a clean glass microscope slide.

Figure 7.3 shows the resulting confocal images. This images show no clear colocalization of 14-3-3τ and αS 30-mers. Concentration-wise, the 14-3-3τ concentration seems a bit high, as single molecules are difficult to identify in figure 7.3(B). For the few brighter spots in the confocal image of 14-3-3τ, no colocalization with αS 30-mers is visible either.

It could be that, because the experiment operates in such a low concentration range, αS 30-mers and 14-3-3τ molecules are not interacting. This may be related to the MST results, that showed a cooperative interaction above a certain 14-3-3τ concentration. It is also possible that the ratio between the 14-3-3τ and αS 30-mers was too low. In the confocal imaging experiments, the αS 30-mer to 14-3-3τ ratio was 1:5. In MST experiments, the αS 30-mer concentration was about 2.4 nM. Using the ratio 1:5, this corresponds to a 14-3-3τ concentration of about 13 nM in MST. This concentration is located in the initial plateau, where no multimerization is observed. Therefore, the lack of interaction may be due to a too low ratio of proteins for interaction.

Furthermore, the measurement of αS 30-mers alone (figure 7.3(A)) does not show many fluorescence counts. Therefore, it may be useful to capture a negative control measurement

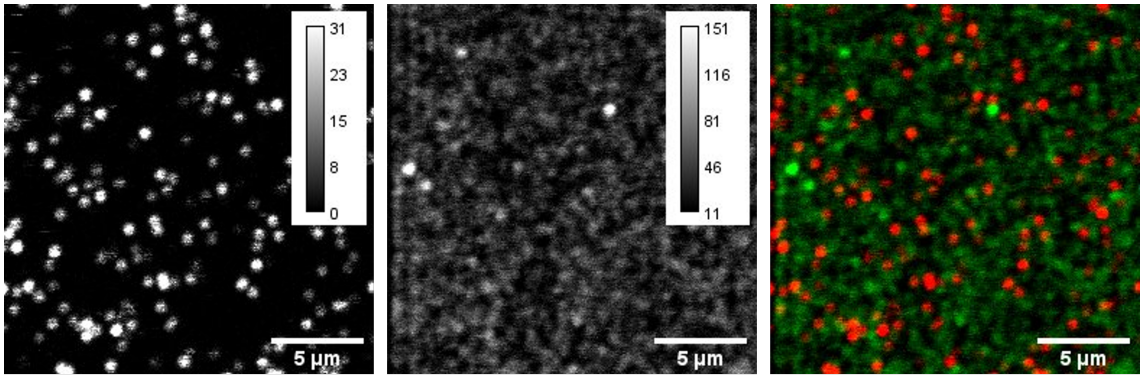

FIGURE 7.3: Confocal images of (A) αS 30-mers, captured with a 560 nm laser, (B) 14-3-3τ, captured with a 640 nm laser, and (C) previous pictures combined, where αS 30-mers are shown in red and 14-3-3τ molecules are shown in green. The intensity scale in (A) and (B) is expressed in fluorescence counts per pixel. The images here are 256x256 pixels.

of a buffer droplet on a glass microscope slide to ensure that the brighter spots observed are not caused by the glass surface or the buffer solution, but represent actual αS 30-mers. In conclusion, no colocalization was observed in this experiment, likely due to the ratio between the proteins or the low concentration regime in which the measurements were performed.

7.4 Conclusion and Discussion

Based on the MST and FCS experiments, it can be concluded that there is an interaction between 14-3-3τ and αS 30-mers. This interaction was not observed in confocal imaging, likely due to the low ratio of proteins or low protein concentrations used in the colocalization experiments.

Chapter 8

14-3-3-τ Interaction with α-Synuclein Fibrils

So far, 14-3-3τ showed an influence on the multimerization of αS monomers. Next to that, interactions between αS 30-mers and 14-3-3τ have been shown. These interactions were with αS species that are in an early stage toward amyloid fibril formation. These interactions may have a role in the prevention of amyloid fibril formation. It is also of interest to see whether 14-3-3τ interacts with fibrils to see if 14-3-3τ possibly plays a role at this level. Therefore, several techniques were used to map these potential interactions.

8.1 MST

In MST, molecular interactions are probed. In this context, MST does not provide a quantitative read-out, but can indicate the presence of possible interactions. In the case of investigating interactions between 14-3-3τ and αS fibrils, the fibrils must be broken into smaller fragments to reach a diffusion coefficient compatible with MST. This is achieved by sonicating the fibril samples using a tip sonicator (10 times for 3 seconds) to generate smaller fibril fragments. MST experiments of 14-3-3τ with an αS fibril titration were performed. A 16-point MST was used. The αS fibril (monomer equivalent) concentration ranged from 50 μM and below. The labeled 14-3-3τ concentration was 15 nM 14-3-3τ-AF568 and the green LED was used for excitation. MST traces were recorded at 60% IR laser power.

Inspecting the results in figure 8.1, it can be observed that the traces at the highest fibril concentrations (above 1250 nM monomer equivalent) display large fluctuations. These bumps in the traces can be explained by 14-3-3τ molecules bound to large αS fibrils passing through the measurement volume. This indicates that there is indeed interaction between 14-3-3τ and the fibrils. It should also be noted that the fibrils likely have some affinity for glass surfaces. Therefore, the actual αS fibril concentration in the measurement volume is probably lower. As a result, the bumpy traces are only observed above a certain concentration threshold, at which the capillary surface is completely saturated by αS fibrils. In summary, MST is not a precise method in this case, but it does provide evidence for interactions between 14-3-3τ and αS fibrils at higher fibril concentrations.

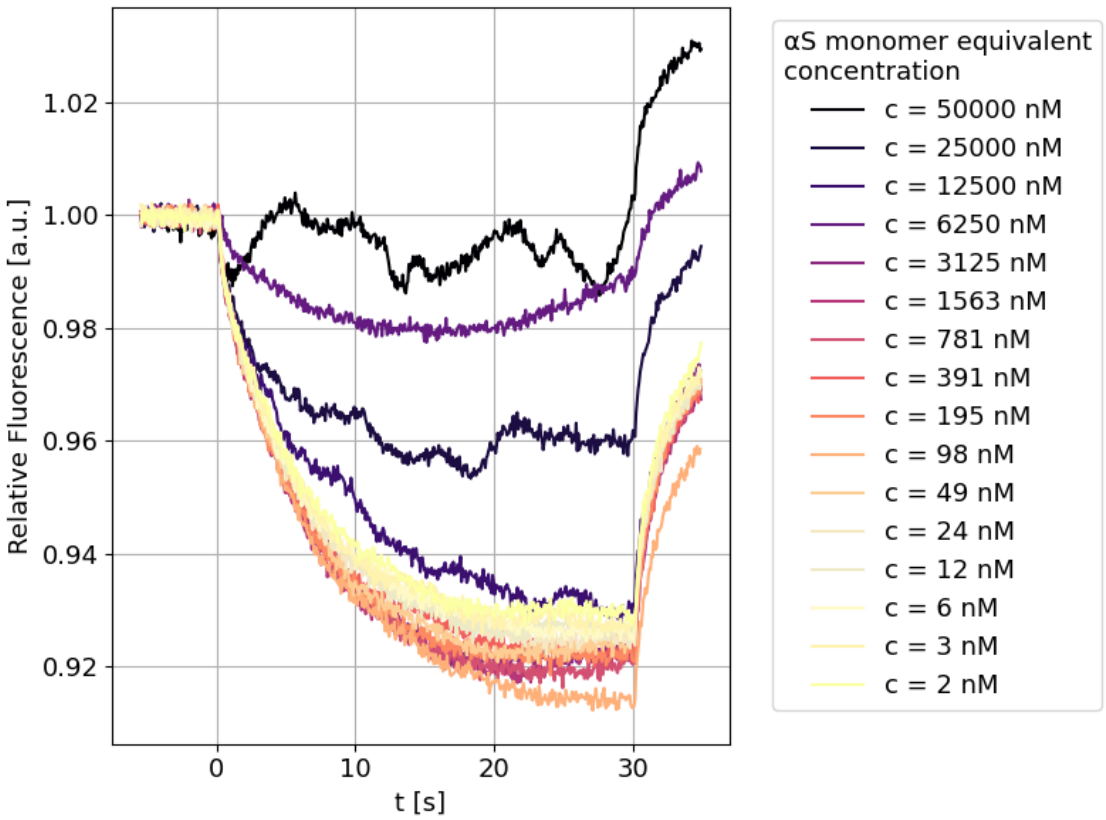

FIGURE 8.1: MST traces of 14-3-3τ with an αS fibril titration. Traces are measured at 60% IR laserpower.

8.2 Confocal Imaging

Performing confocal imaging of αS fibrils and 14-3-3τ directly after each other can reveal whether colocalization occurs. If colocalization is observed, it is likely that 14-3-3τ is bound to the fibrils, indicating an interaction. Therefore, confocal imaging was performed on samples with 14-3-3τ-AF647 and fibrils stained with ThT. First, a 20 μL droplet of αS fibrils in a concentration of 40 μM (monomer equivalent) was placed on the cover glass. After allowing it to settle for half an hour, the surface was washed three times with 20 μL buffer (10 mM Tris, 10 mM EDTA, 0.1 mM EDTA, pH = 7.4), ending with a buffer drop left on the cover glass with αS fibrils on the glass surface. Then, 20 μL of 40 nM 14-3-3τ labeled with AF647 was added. After another half an hour of incubation, the surface was washed again three times with 20 μL buffer, ending with a buffer droplet on the cover glass with αS fibrils at the surface with potentially the labeled 14-3-3τ with AF647.
The sample was imaged using a 636 nm laser (PicoQuant) and a 401 laser (PicoQuant). The laser delivered an optical power of 50 a.u., corresponding to 0.1 μW, in the back focal plane.

The resulting confocal images are shown in figure 8.2. In this figure, the structure of fibrils is clearly visible. There is evident colocalization between αS fibrils and 14-3-3τ. The images captured at 401 nm and 636 nm resemble each other almost perfectly. This indicates that there is interaction between αS fibrils and 14-3-3τ, which is consistent with the MST results. However, it should be noted that there is a possibility that the interaction

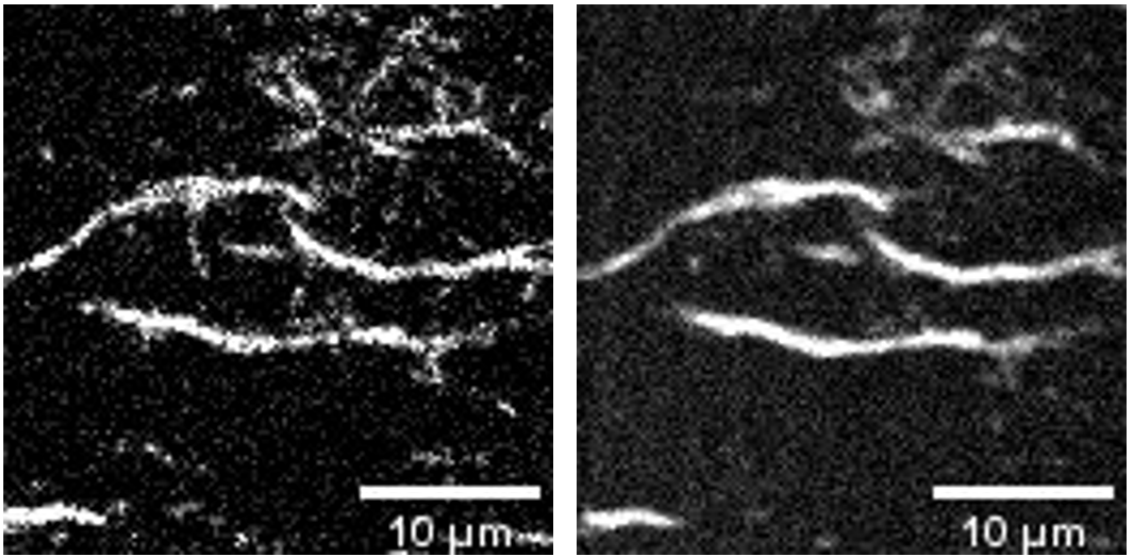

FIGURE 8.2: Confocal images of (A) αS fibrils (ThT stained), captured with a 401 nm laser, (B) 14-3-3τ, captured with a 636 nm laser.

is dye-mediated. AF647 is a zwitterionic dye [52], meaning it has a positive charge as well as a negative charge. The αS fibrils have a core consisting of residues 37 to 99, while the N-terminal and C-terminal remain flexible. These regions are solvent-accessible and form a disordered and dynamic "fuzzy coat" that surrounds the structured fibril core [13]. The N-terminal region (positively charged) and C-terminal region (negatively charged) can both interact with a zwitterionic dye, potentially leading to a dye-mediated interaction. Therefore, it would be prudent to repeat the experiment using a different dye, preferably one without a charge. Furthermore, it should be noted that during the experiments 14-3-3τ "blobs" were observed that were not ThT positive. These blobs could be aggregates of 14-3-3τ.

8.3 Conclusion and Discussion

Both MST experiments and confocal imaging indicated interaction between fibrils and 14-3-3τ. In the possible case that 14-3-3 behaves as an "unhappy" chaperone [31], the interaction of αS fibrils with 14-3-3τ can be explained in the following way: Adding 14-3-3τ to a solution of amyloid fibrils (in dynamic equilibrium with αS monomers), disturbs the dynamic equilibrium of the αS fibrils and monomers. To reduce the system's free energy, 14-3-3τ interacts with the fibrils. Based on the experiments, it is not possible to determine whether the fibrils are merely coated with 14-3-3τ or whether mixed fibrils of αS and 14-3-3τ are formed. Both scenarios may contribute to disaggregation or the prevention of further aggregation.

Chapter 9

14-3-3τ Aggregation

The interaction between αS and 14-3-3τ is a key point of interest in this research. To better understand the interactions between these two proteins, the behavior of 14-3-3τ on its own needs to be examined. Previous chapters have presented observations of 14-3-3τ self-assembly ("14-3-3τ Interaction with αS Oligomers: FCS" and "14-3-3τ Interaction with α-Synuclein Fibrils: Confocal Imaging"). This chapter further explores this using the techniques MST and confocal imaging.

9.1 Confocal Imaging

With confocal imaging it is attempted to visualize how these aggregates look. Confocal imaging is performed on 14-3-3τ-AF647. A droplet with a concentration of 40 nM 14-3-3τ-AF647 was placed on a cover glass. After allowing the sample to settle for 30 minutes, the surface was washed three times with buffer (10 mM Tris, 10 mM EDTA, 0.1 mM EDTA, pH = 7.4), ending with a buffer droplet on the cover glass.
The sample was imaged using a 636 nm laser (PicoQuant). The laser delivered an optical power of 50 a.u., corresponding to 0.1 μW in the back focal plane.

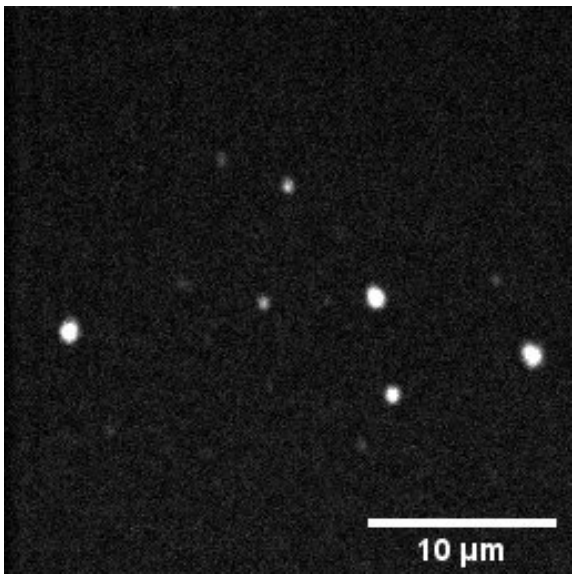

FIGURE 9.1: Confocal image of 14-3-3τ aggregates, captured with a 636 nm laser.

The results are summarized in figure 9.1. It can be observed that some bright spots are present in this image. These spots are enormous in size (approximately 1 μm), so it is not possible that these represent dimers of 14-3-3τ, but these should be large 14-3-3τ aggregates. These aggregates likely adhere to the surface, as they remain there after washing. The aggregates are shaped more like clumps, lacking a defined defined structure like the fibrillar structure of αS fibrils.

9.2 MST

Using MST, interactions between dimers of 14-3-3τ are evaluated. Additionally, more insight is gained into the concentration dependency of the aggregation process.
MST measurements (16-points) were performed for a dilution series of 14-3-3τ with the highest concentration being ~140 μM. The samples had dye concentrations of 15 nM 14-3-3τ-AF568, and the green LED was used for excitation. Due to the use of a dye that sticks to the capillary walls, the T-jump region (0.5 to 1.5 s) was selected for analysis instead of the region from 5 to 30 seconds. With that exception, the data were processed as described in Chapter 3 and fitted using the self-assembly model (equation 2.1). Because the T-jump region was used, it was not possible to calculate standard deviations for the measurement using early, mid, and late regimes, as F_{norm} does not remain constant during the T-jump, but decreases.

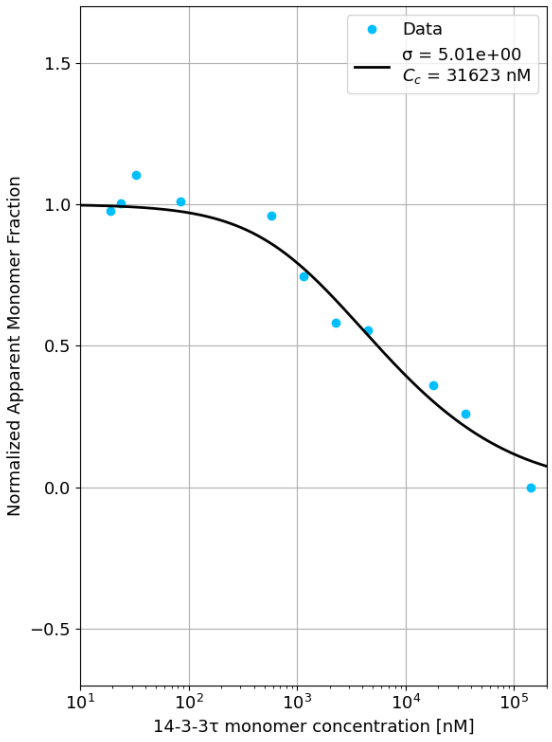

FIGURE 9.2: Normalized apparent monomer fractions for 14-3-3τ multimerization with a fit of the nucleation self-assembly model.

The results of the MST experiments are shown in figures 9.2 and 9.3. These results indicate multimerization or aggregation of 14-3-3τ, which appears to be concentration-dependent. The multimerization follows simple binding kinetics and is non-cooperative. There is no sharp critical concentration from which multimerization occurs, but is a rather

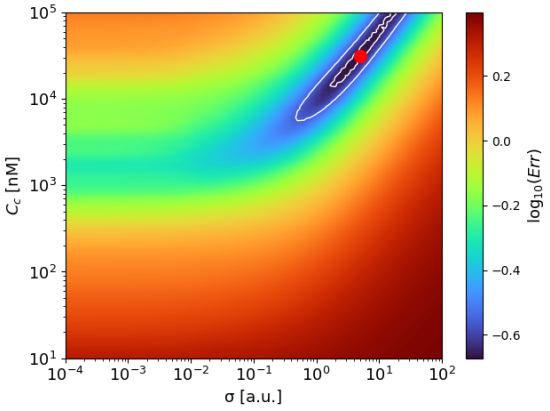

FIGURE 9.3: Error plot for fitting errors of the nucleation self-assembly model for the fit of 14-3-3τ multimerization.

gradual process.
It is important to note that stickiness of the dye could have affected the results. At high concentrations of 14-3-3τ, almost all dye is present in solution, and the capillary surface is primarily saturated with unlabeled 14-3-3τ. However, as the overall concentration of 14-3-3τ decreases while the labeled 14-3-3τ concentration remains constant, an increasing fraction of labeled 14-3-3τ may bind to the capillary surface, resulting in a decreased dye concentration in solution. This effect can create a false-positive binding curve. The trend observed here, differs from that seen in the T-jump results of αS 30-mers, where a similar titration of 14-3-3 was used in the presence of a sticky labeled target. This difference could indicate that the T-jump is indeed not affected as much by stickiness, and what is observed is indeed multimerization or aggregation of 14-3-3τ.
Considering the conclusion and discussion of section "14-3-3-τ Interaction with α-Synuclein oligomers: FCS", it also possible that, due to the dilution from high to low 14-3-3τ concentrations, aggregates take longer to fall apart than the time after which the samples are measured. In this case, the actual binding curve would be shifted more to the right. In the MST experiment, samples were measured from high to low concentrations. This could result in a decrease in the number of aggregates measured as the concentration decreases, potentially leading to a larger measured difference in ΔF_{norm}.

9.3 Conclusion and Discussion

In general, the confocal imaging and MST experiments show that 14-3-3τ forms multimers and aggregates, a phenomenon that is unreported in literature so far. The MST measurements may indicate that 14-3-3 multimerization is concentration-dependent, and the multimers are formed through simple binding kinetics. In the case that 14-3-3 is classified as "unhappy" chaperone [31], the formation of multimers can be explained by a reduction in chemical potential of the multimeric form compared to the dimeric form of the chaperone.
An important consideration is how this behavior influences the combined system of 14-3-3τ and αS. The formation of 14-3-3τ multimers or aggregates may compete with the formation of mixed multimers. The multimerizing behavior of 14-3-3 could potentially be prevented in αS multimerization experiments through the use of detergents. However, such additives are likely to affect not only the multimerization of 14-3-3τ, but also that of αS. Therefore,

careful selection of an appropriate additive is crucial to ensure that it does not interfere with αS multimerization.

Chapter 10

General Conclusion

In this research, interactions between the 14-3-3 chaperone and αS were studied in multiple stages of aggregation. Early αS multimerization and possible interactions with 14-3-3 were studied using an optimized MST measurement procedure. Electrostatic and hydrogen bonds turned out to be important interactions in αS multimerization. When these types of interactions were reduced, the cooperativity of the normally cooperative αS multimerization mechanism was lowered. Interaction of 14-3-3 with early αS multimers was also observed, with a decrease in cooperativity as result. Furthermore, 14-3-3τ showed interaction with αS 30-mers and fibrils. It must be noted that aggregation of 14-3-3τ was also observed, likely affecting the interaction between αS and 14-3-3τ. The insights about the possible interference of 14-3-3 proteins in controlling aggregation of αS could lead to the development of new treatment strategies.

Chapter 11

General Discussion

In this chapter, the findings of this research will be discussed in a broader context, with links between different experiments and results.

Effect of Adding TCEP During Labeling

For MST experiments, the most suitable dye was selected, αS-AF488 (labeled in the presence of TCEP), which showed minimal sticking to the capillary walls and the highest fluorescence intensity among the dyes tested. However, it is not exactly clear what impact TCEP has on αS.

TCEP plays a catalytic role during labeling of αS-A140C [53]. It can activate the cysteine to form a phosphonium intermediate, which is much more reactive than the thiolate formed in the reaction without TCEP (Michael Addition [53]). After this, the reaction proceeds as usual: the protein is attached to the dye, and TCEP is released. Assuming that all TCEP is removed by filtering the sample with Zebaspins, there should be no difference between the labeled αS with and without TCEP during labeling. However, a difference is observed in terms of stickiness to a glass surface. Therefore, it is likely that some TCEP remained in the sample.

Glass is slightly acidic, resulting in a slightly negative charge on the glass surface [54]. Combining this with the hydrophobic nature of the water-glass interphase, amphiphilic proteins like αS tend to stick to the surface. This behavior may change if TCEP is still present. TCEP is a highly polar molecule with a net charge of -3 in solution [55]; when oxidized it becomes zwitterionic. Due to its high polarity, it is not surprising if TCEP may adhere to the αS molecules and is not completely removed after filtering. This increases the solubility of αS. TCEP may surround αS like a coat and screens its charges, resulting in fewer ionic interactions with glass or other molecules. This may also influence interactions between αS monomers and affect multimerization. In experiments where extra salt was added to reduce electrostatic interactions, a reduction in cooperativity was observed in early-phase αS multimerization. This may suggest that in the absence of TCEP, αS multimerization could be even more cooperative.

To test whether the presence of TCEP reduces the stickiness of the αS-AF488 dye, an experiment was conducted in which TCEP was added after labeling, incubated for two hours, and then filtered out of the sample using a Zebaspin twice. Following this protocol, the dye still showed stickiness to the glass surface of capillaries, similar to the dyes shown in figure 4.1(A). This experiment suggests that either TCEP had an effect on the structure of the labeled protein formed during labeling, or that TCEP may undergo changes during labeling (possibly due to oxidation other modifications).

Interactions between 14-3-3 Chaperones and αS Multimers, Oligomers and Fibrils

In this research, the effect of different isoforms of 14-3-3 on αS WT multimerization was investigated. All isoforms influenced multimerization, which was shown by a decrease in the difference in ΔF_{norm} between the initial and final plateaus of the binding curves. This is likely due to the formation of mixed multimers, which alters the multimerization process [7]. Additionally, a clear reduction in cooperativity was observed for 14-3-3τ (figure 6.1, as well as for 14-3-3σ (figure 6.5). For 14-3-3γ, only a slight reduction was observed. However, this was based only on 16-point MST, which is less reliable.

The interactions between 14-3-3 chaperones and αS multimers can be partially explained by the structural similarities between them. Amino acids 8 to 61 of αS (Located mostly in the N-terminal domain) share over 40% sequence homology with amino acid 45 to 104 of 14-3-3 [56]. This region has an α-helical structure and is positively charged. These regions can interact via hydrogen bonds.

In addition to influencing early-phase αS multimerization, 14-3-3τ also interacts with αS 30-mers and fibrils. Interaction with αS 30-mers suggests that αS oligomers may form mixed multimers, potentially outcompeting the pathway to amyloid fibril formation [7]. Interaction of 14-3-3τ with fibrils may contribute to disaggregation or prevention of further aggregation.

Furthermore, interactions of 14-3-3 with the N-terminal of αS were shown for 14-3-3ζ in amyloid fibril formation [57]. These interactions are transient and weak, resulting in no interaction between αS monomers and 14-3-3. In case of multimers, the multivalent interactions may be strong enough to bind 14-3-3, like shown for interaction between 14-3-3 and Tau protein [58]. Similar interactions are likely for other 14-3-3 isoforms, as the structures of human 14-3-3 protein isoforms are in general very similar. Subtle differences exist among them, including variations in the angle between the two subunits of the dimer, the lengths of certain loop regions, and the lengths of specific α-helices [59]. Similar behavior of the 14-3-3 isoforms is also reflected in their influence on early αS multimerization in MST, where a decrease in cooperativity was observed.

As mentioned above, 14-3-3 is believed to interact with the N-terminal of αS. 14-3-3 is an acidic protein and has many negatively charged regions on its surface [58]. The negatively charged regions of 14-3-3 may screen the charges of the positively charged N-terminal region of αS, which may reduce the charges of this region and limit the availability of hydrogen bonding sites. By reducing the electrostatic interactions and options for hydrogen bonds, the cooperativity of αS multimerization can be decreased as shown in the experiments with salt and GuHCl added to αS multimerization. This is also consistent with the experimental results showing reduced cooperativity when 14-3-3τ (0.67 μM) and 14-3-3σ (2 μM) were added to multimerizing αS.

Hydrophobic interactions are reported to play an important role in αS aggregation [57]. The NAC region plays a significant role in these hydrophobic interactions [10][60]. If the NAC region would interact with 14-3-3, the hydrophobic interactions between αS molecules would also be altered, influencing αS multimerization. However, no evidence for this was found in the experiments where 1,6-hexanediol (5% v/v and 10% v/v) was added to multimerizing αS. This is not in line with expectations, as literature reports that the hydrophobic interactions between the NAC domain and C-terminal of αS play a critical role in aggregation [60][61]. Therefore, reducing these interactions is expected to result in altered aggregation.

Furthermore, hydrophobic parts of the αS fibril structure contribute to the stabilization of αS fibrils through mechanisms such as hydrophobic packing of aromatic and methyl-containing aromatic residues (I88, A91, and F94), and steric zippers formed by hydrophobic side chains (e.g., V49, V77, and V82) [62]. These stabilizing hydrophobic interactions may also play a role in early multimerization and are reduced in the case where 1,6-hexanediol is added. This would likely result in less stability of the formed multimers, which is expected to change the early multimerization process.
That there is no influence of the addition of 1,6-hexanediol observed in α S multimerization, may also be due to the MST measurement procedure. From this technique, only a few parameters of the multimerization mechanism can be derived, but parameters such as multimer stability, multimerization rate, and extend of multimerization are not measured. It could be that electrostatic and hydrogen bonds are strong enough for the formation of multimers without hydrophobic interactions, but that these multimers are not stable or the number of multimers is lower.

Influence of 14-3-3 Aggregates in Various Measurements
Aggregation of 14-3-3τ was observed in multiple experiments. This aggregating behavior of 14-3-3 is not described in existing literature. In FCS, the aggregates were detected in measurements taken immediately after placing the sample on the cover glass. Aggregates were also visible in confocal images and multimerization was identified in MST measurements. It is expected that the aggregates of 14-3-3 function differently from its dimers. Therefore, these aggregates probably have influenced many of the measurements involving 14-3-3 in some way.
14-3-3 aggregates could also have influenced αS multimerization in the presence of 14-3-3 during MST measurements. As shown in figures 6.1(B) and (C), higher concentrations of 14-3-3τ (2 μM and 5 μM) were associated with significant variation in ΔF_{norm} values, resulting in poor fits of the data to the nucleation self-assembly model. These variations may be linked to increased aggregation of 14-3-3τ at higher concentrations. Figure 9.2 shows that with increasing concentrations, the normalized apparent monomer fraction decreases. The aggregates may interact with αS in a less predictable manner than the 14-3-3τ monomers, thereby influencing the formation of mixed multimers. This results in a greater variability in MST response, as reflected in the MST curves. In contrast, for 14-3-3σ (2 μM), the binding curve (figure 6.5) is well-defined and shows a reduction in cooperativity. This may indicate that 14-3-3σ is less prone to aggregation at this 14-3-3 concentration.

Chapter 12

Recommendations

Stoichiometry of 14-3-3τ and α-Synuclein Oligomer Interaction
To better understand the stoichiometry of the 14-3-3 interaction with αS oligomers, it is useful to determine how many 14-3-3 molecules bind to each oligomer. This information can provide insight into the binding mechanism. For example, if multiple 14-3-3 dimers bind to a fraction of αS oligomers but none are bound to the rest, this indicates cooperative binding. Furthermore, measurements of early αS multimerization with 14-3-3 indicated co-assembly of αS and 14-3-3, with likely multiple 14-3-3 molecules per multimer. If αS 30-mers co-assemble with 14-3-3, it is also expected to identify multiple 14-3-3 dimers per αS 30-mer.
The number of 14-3-3 molecules bound to each oligomer can be investigated by single molecule photobleaching. For this experiment, αS 30-mers and 14-3-3 can be diluted to a low concentration in a PVA solution. These proteins in solution can be immobilized by spincoating the PVA solution on a cover slip, which results in the proteins being embedded in a thin layer of PVA. Low concentrations of proteins are recommended to be used to ensure that the proteins are well separated in space. Using the fluorescence label of the αS 30-mers, αS 30-mers can be located. At these spots, single molecule photobleaching experiments can be performed by bleaching the fluorescent labels of 14-3-3, and the number of photobleaching steps can be counted. This number corresponds to the number of 14-3-3 molecules bound to an αS 30-mer (assuming a DOL of 1 for 14-3-3).
In addition, an excess of 14-3-3 molecules is desired. However, concentrations can not be very high, because no single molecules can be measured in that case. Therefore, it might be interesting to use small DOLs and use the DOL to determine the actual number of molecules bound to αS 30-mers.
During the research project, some trials were performed using this measurement technique, but to be able to see single photobleaching steps, the glass surface and the PVA solution need to be clear of any other fluorescence. This condition is difficult to obtain. In figure 12.1, a few results of these trials are shown. Based on this figure, it can be concluded that even the glass surface of the cover slip was not clean enough and shows similar fluorescence as the cover glass with PVA and AF488, indicating that figure 12.1(A) mainly shows fluorescence of the glass surface and not of AF488. Therefore, care must be taken in cleaning the glass surface of the cover slip.

Influence of Molecular Interactions in Early α-Synuclein Multimerization
To better understand the cooperative multimerization mechanism of αS, different types of interactions were examined; electrostatic interactions, hydrophobic interactions and hydrogen bonds. Reducing electrostatic interactions and hydrogen bonds decreased the

cooperativity in αS-WT multimerization, indicating that these type of interactions play a role in the cooperativity of the multimerization process. No clear effect for hydrophobic interactions was found.
To investigate hydrophobic interactions in early αS multimerization, 1,6-hexanediol was added to multimerizing αS at concentrations up to 10% v/v, with no observable change in multimerization behavior of αS. This raises the question whether the concentration was too low to produce a clear effect. Literature reports that 5 to 10% v/v 1,6-hexanediol can dissolve or weaken liquid-liquid phase separation driven by hydrophobic interactions [63]. Therefore, it is expected that at least at the concentration of 10% v/v 1,6-hexandiol a noticeable difference would be observed in αS multimerization, as a consequence of reduced hydrophobic interactions. Consequently, it is recommended to repeat the measurements. Testing higher concentrations of 1,6-hexanediol may reveal whether a more pronounced effect can be observed.
To investigate the influence of hydrogen bonds in αS multimerization, guanidine hydrochloride (GuHCl) was used in MST experiments. However, the experiments were performed for unknown concentrations of GuHCl. It is therefore good to repeat the experiment with multiple concentrations and see what the concentration-dependency is.

Dye-mediated Interactions
In the experiments performed, indications of interaction between 14-3-3 and αS multimers, oligomers, and fibrils were found. It is necessary to be a bit careful with these results, because most experiments were conducted using one dye, and dye-mediated interactions could play a role. It would be good to test other possible dyes next.

Getting more Quantitative Results on 14-3-3τ Interaction with Fibrils
For the interaction between 14-3-3τ and fibrils, no quantitative results were obtained. MST experiments involving a fibril titration in the presence of 14-3-3τ provided only a preliminary indication of interaction. Therefore, it is of interest to perform FCS experiments on labeled 14-3-3τ with fibril seeds at varying concentrations. Using this technique, a binding curve of the interaction between fibrils and 14-3-3τ can likely be obtained, which was not possible using MST. These experiments should be conducted using cover glasses with PEG passivated surfaces. Such surfaces minimize sticking of the sample sticking to the cover glass and allow for more accurate determination of protein concentrations in solution.

Reducing 14-3-3 Aggregation in Stock Solutions
In multiple experiments, the presence of 14-3-3 multimers or aggregates was observed. These aggregates may have formed in the high-concentration stock solutions. To prevent aggregation in these stock solutions, it is recommended to add TCEP to reduce disulfide bonds between 14-3-3 molecules [64]. This would help ensure that the starting point for experiments is dimeric 14-3-3, rather than pre-formed aggregates that may or may not disaggregate under experimental conditions. Using this method, key experiments to repeat include FCS measurements of 14-3-3τ and 14-3-3τ in combination with αS 30-mers. Additionally, MST measurements with different 14-3-3 isoforms should be repeated to determine whether improved binding curves can be obtained, especially for high 14-3-3 concentrations.

More Research on 14-3-3σ
This research primarily focused on the interaction between αS and 14-3-3τ. However, based on the results from different isoforms in Chapter 6, the σ isoform also shows promising effects reducing both cooperativity and the difference in ΔF_{norm} between the two plateaus.

Therefore, this isoform is worth further investigation.

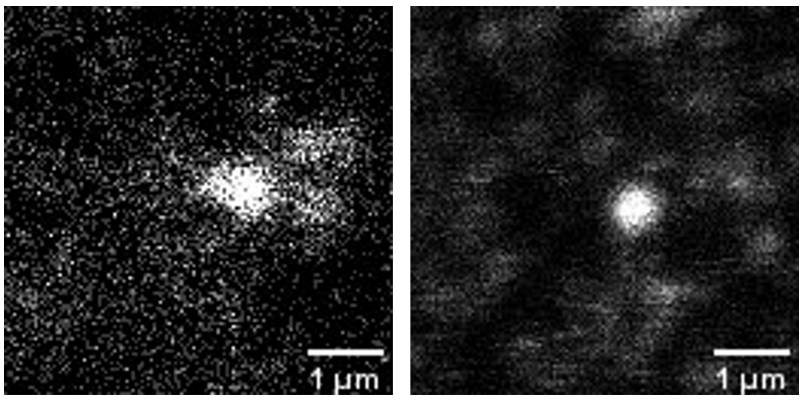

FIGURE 12.1: Confocal images of (A) AF488 immobilized by spinocoating a PVA solution on a cover slip, captured with a 483 nm laser, and (B) the cover slip surface without a sample, captured with a 483 nm laser.

Influence of TCEP on α-Synuclein Conformation
It would be interesting to test how TCEP can change αS conformation. This will provide more insight on the effect TCEP can have on αS multimerization. Experiments using the technique single-molecule fluorescence resonance energy transfer (smFRET) can be performed to study molecular conformation. Experiments described in [65] can be repeated in the presence of TCEP. When the αS molecule is found to be in a more extended form than without TCEP, the protein is probably completely covered with TCEP molecules. This gives the complex a negative charge, and hence no sticking to glass surfaces was observed in this research.

Measurement Environment
It could be interesting to repeat experiments in environments that more closely resemble cells. Interactions can differ based on conformation and because αS is a disordered protein which changes its conformation based on its surroundings, this could be of great relevance. MST measurements can be performed under conditions that more closely resemble the cytosol. For example, crowding in cells can be mimicked using a crowding agent such as PEG [66]. Furthermore, instead of using only NaCl at a low concentration, salt concentrations could be increased and extended with other ions, such as potassium and bicarbonate ions [47], to better resemble the conditions in the cytosol.

Chapter 13

Acknowledgments

I would like to sincerely thank my daily supervisor, Gobert Heesink, for his guidance throughout the entire project. Thank you for teaching me various measurement techniques, for engaging in discussions about the meaning of my results, and for providing valuable critical feedback. This greatly helped me during the thesis process. Thank you for your willingness to help and for always being there when I needed support.

I would also like to thank Mireille Claessens and Christian Blum for their guidance and support, especially during what was also a difficult period of reorganization. Thank you for the insightful discussions, and for helping to shape the direction of my research. I would also like to thank Michel Versluis for being my external supervisor, and for thinking along with me during the uncertain times of the reorganization.

Many thanks to all the NBP members. Thank you for making me feel welcome and for creating a pleasant and open atmosphere. I would especially like to thank Kirsten Leijenhorst-Groener and Robert Molenaar for their support in the biochemical and optical labs, respectively.
I would also like to thank the other students I shared this period with. It would have been much less fun without them. A special thank you to Bente for all the tea breaks and good conversations.

And last but not least, I am deeply grateful for the support I received from my family and friends. Thank you for listening and for always being there for me.

Bibliography

1. Erkkinen, M. G., Kim, M.-O. & Geschwind, M. D. Clinical neurology and epidemiology of the major neurodegenerative diseases. *Cold Spring Harbor perspectives in biology* **10,** a033118 (2018).
2. Koo, E. H., Lansbury Jr, P. T. & Kelly, J. W. Amyloid diseases: abnormal protein aggregation in neurodegeneration. *Proceedings of the National Academy of Sciences* **96,** 9989–9990 (1999).
3. Migliore, L. & Coppedè, F. Genetics, environmental factors and the emerging role of epigenetics in neurodegenerative diseases. *Mutation Research/Fundamental and Molecular Mechanisms of Mutagenesis* **667,** 82–97 (2009).
4. Davis, A. A., Leyns, C. E. & Holtzman, D. M. Intercellular spread of protein aggregates in neurodegenerative disease. *Annual review of cell and developmental biology* **34,** 545–568 (2018).
5. Wong, Y. C. & Krainc, D. α-synuclein toxicity in neurodegeneration: mechanism and therapeutic strategies. *Nature medicine* **23,** 1–13 (2017).
6. Beissinger, M. & Buchner, J. How chaperones fold proteins. *Biological chemistry* **379,** 245–259 (1998).
7. Heesink, G. *et al.* 14-3-3τ as a modulator of early α-synuclein multimerization and amyloid formation. *ACS chemical neuroscience* **15,** 1926–1936 (2024).
8. Burré, J., Sharma, M. & Südhof, T. C. Cell biology and pathophysiology of α-synuclein. *Cold Spring Harbor perspectives in medicine* **8,** a024091 (2018).
9. Saraiva, M. A. & Florêncio, M. H. Early α-synuclein aggregation is overall delayed and it can occur by a stepwise mechanism. *Biochemical and Biophysical Research Communications* **635,** 30–36 (2022).
10. Emamzadeh, F. N. Alpha-synuclein structure, functions, and interactions. *Journal of Research in Medical Sciences* **21,** 29 (2016).
11. Meade, R. M., Fairlie, D. P. & Mason, J. M. Alpha-synuclein structure and Parkinson's disease–lessons and emerging principles. *Molecular neurodegeneration* **14,** 1–14 (2019).
12. Villar-Piqué, A., Lopes da Fonseca, T. & Outeiro, T. F. Structure, function and toxicity of alpha-synuclein: the Bermuda triangle in synucleinopathies. *Journal of neurochemistry* **139,** 240–255 (2016).
13. Vidović, M. & Rikalovic, M. G. Alpha-synuclein aggregation pathway in Parkinson's disease: current status and novel therapeutic approaches. *Cells* **11,** 1732 (2022).
14. Bertoncini, C. W. *et al.* Release of long-range tertiary interactions potentiates aggregation of natively unstructured α-synuclein. *Proceedings of the National Academy of Sciences* **102,** 1430–1435 (2005).

15. Ramalingam, N., Haass, C. & Dettmer, U. Physiological roles of α-synuclein serine-129 phosphorylation–not an oxymoron. *Trends in neurosciences* (2024).

16. Zhang, S. *et al.* LK6/Mnk2a is a new kinase of alpha synuclein phosphorylation mediating neurodegeneration. *Scientific reports* **5,** 12564 (2015).

17. Chau, K.-Y., Ching, H. L., Schapira, A. H. & Cooper, J. M. Relationship between alpha synuclein phosphorylation, proteasomal inhibition and cell death: relevance to Parkinson's disease pathogenesis. *Journal of neurochemistry* **110,** 1005–1013 (2009).

18. Ghanem, S. S. *et al.* α-Synuclein phosphorylation at serine 129 occurs after initial protein deposition and inhibits seeded fibril formation and toxicity. *Proceedings of the National Academy of Sciences* **119,** e2109617119 (2022).

19. Paleologou, K. E. *et al.* Phosphorylation at Ser-129 but not the phosphomimics S129E/D inhibits the fibrillation of α-synuclein. *Journal of Biological Chemistry* **283,** 16895–16905 (2008).

20. Gracia, P., Camino, J. D., Volpicelli-Daley, L. & Cremades, N. Multiplicity of α-synuclein aggregated species and their possible roles in disease. *International journal of molecular sciences* **21,** 8043 (2020).

21. Zhao, D. & Moore, J. S. Nucleation–elongation: a mechanism for cooperative supramolecular polymerization. *Organic & biomolecular chemistry* **1,** 3471–3491 (2003).

22. Bukau, B., Weissman, J. & Horwich, A. Molecular chaperones and protein quality control. *Cell* **125,** 443–451 (2006).

23. Witt, S. N. Hsp70 molecular chaperones and Parkinson's disease. *Biopolymers: Original Research on Biomolecules* **93,** 218–228 (2010).

24. Nachman, E. *et al.* Disassembly of Tau fibrils by the human Hsp70 disaggregation machinery generates small seeding-competent species. *Journal of Biological Chemistry* **295,** 9676–9690 (2020).

25. Huang, X. *et al.* 14-3-3 proteins are potential regulators of liquid–liquid phase separation. *Cell Biochemistry and Biophysics* **80,** 277–293 (2022).

26. Segal, D. *et al.* A central chaperone-like role for 14-3-3 proteins in human cells. *Molecular cell* **83,** 974–993 (2023).

27. Cornell, B. & Toyo-Oka, K. 14-3-3 proteins in brain development: neurogenesis, neuronal migration and neuromorphogenesis. *Frontiers in molecular neuroscience* **10,** 318 (2017).

28. Shimada, T., Fournier, A. E. & Yamagata, K. Neuroprotective function of 14-3-3 proteins in neurodegeneration. *BioMed research international* **2013,** 564534 (2013).

29. Plotegher, N. *et al.* The chaperone-like protein 14-3-3η interacts with human α-synuclein aggregation intermediates rerouting the amyloidogenic pathway and reducing α-synuclein cellular toxicity. *Human molecular genetics* **23,** 5615–5629 (2014).

30. Yacoubian, T. A. *et al.* Differential neuroprotective effects of 14-3-3 proteins in models of Parkinson's disease. *Cell death & disease* **1,** e2–e2 (2010).

31. Linse, S., Thalberg, K. & Knowles, T. P. The unhappy chaperone. *QRB discovery* **2,** e7 (2021).

32. López-Méndez, B., Uebel, S., Lundgren, L. P. & Sedivy, A. Microscale Thermophoresis and additional effects measured in NanoTemper Monolith instruments. *European Biophysics Journal* **50,** 653–660 (2021).

33. Duhr, S. & Braun, D. Why molecules move along a temperature gradient. *Proceedings of the National Academy of Sciences* **103,** 19678–19682 (2006).

34. Dhont, J. K., Wiegand, S., Duhr, S. & Braun, D. Thermodiffusion of charged colloids: Single-particle diffusion. *Langmuir* **23,** 1674–1683 (2007).

35. Elson, E. L. Fluorescence correlation spectroscopy: past, present, future. *Biophysical journal* **101,** 2855–2870 (2011).

36. Kilpatrick, L. E. & Hill, S. J. The use of fluorescence correlation spectroscopy to characterize the molecular mobility of fluorescently labelled G protein-coupled receptors. *Biochemical Society Transactions* **44,** 624–629 (2016).

37. Semerdzhiev, S. A., Dekker, D. R., Subramaniam, V. & Claessens, M. M. Self-assembly of protein fibrils into suprafibrillar aggregates: bridging the nano-and mesoscale. *ACS nano* **8,** 5543–5551 (2014).

38. Visser, E. J. *et al.* From Tethered to Freestanding Stabilizers of 14-3-3 Protein-Protein Interactions through Fragment Linking. *Angewandte Chemie International Edition* **62,** e202308004 (2023).

39. Vaneyck, J., Segers-Nolten, I., Broersen, K. & Claessens, M. M. Cross-seeding of alpha-synuclein aggregation by amyloid fibrils of food proteins. *Journal of Biological Chemistry* **296** (2021).

40. Van Rooijen, B. D., Claessens, M. M. & Subramaniam, V. Lipid bilayer disruption by oligomeric α-synuclein depends on bilayer charge and accessibility of the hydrophobic core. *Biochimica et Biophysica Acta (BBA)-Biomembranes* **1788,** 1271–1278 (2009).

41. Macháň, R. & Hof, M. in *Practical Manual for Fluorescence Microscopy Techniques* 24 (PicoQuant GmbH, 2016).

42. Tarasov, S. G., Dyba, M., Yu, J. & Tarasova, N. Design and Generation of Self-Assembling Peptide Virus-like Particles with Intrinsic GPCR Inhibitory Activity. *Polypeptide Materials: Methods and Protocols,* 135–148 (2021).

43. López-Méndez, B. *et al.* Reproducibility and accuracy of microscale thermophoresis in the NanoTemper Monolith: a multi laboratory benchmark study. *European biophysics journal* **50,** 411–427 (2021).

44. Al-Jubair, T. *et al.* Characterization of human aquaporin protein-protein interactions using microscale thermophoresis (MST). *STAR protocols* **3,** 101316 (2022).

45. Entzian, C. & Schubert, T. Studying small molecule–aptamer interactions using MicroScale Thermophoresis (MST). *Methods* **97,** 27–34 (2016).

46. Baumgartner, R., Fu, H., Song, Z., Lin, Y. & Cheng, J. Cooperative polymerization of α-helices induced by macromolecular architecture. *Nature Chemistry* **9,** 614–622 (2017).

47. Hall, J. E. & Hall, M. E. *Guyton and Hall Textbook of Medical Physiology E-Book: Guyton and Hall Textbook of Medical Physiology E-Book* (Elsevier Health Sciences, 2020).

48. Narimoto, T. *et al.* Conformational stability of amyloid fibrils of β2-microglobulin probed by guanidine-hydrochloride-induced unfolding. *FEBS letters* **576,** 313–319 (2004).

49. Young, M., Carroad, P. & Bell, R. Estimation of diffusion coefficients of proteins. *Biotechnology and bioengineering* **22,** 947–955 (1980).

50. Gu, Q., Cuevas, E., Raymick, J., Kanungo, J. & Sarkar, S. Downregulation of 14-3-3 proteins in Alzheimer's disease. *Molecular neurobiology* **57,** 32–40 (2020).

51. Bartels, T., Choi, J. G. & Selkoe, D. J. α-Synuclein occurs physiologically as a helically folded tetramer that resists aggregation. *Nature* **477,** 107–110 (2011).

52. Fan, S. *et al.* Observing the reversible single molecule electrochemistry of Alexa Fluor 647 dyes by total internal reflection fluorescence microscopy. *Angewandte Chemie* **131,** 14637–14640 (2019).

53. Ahangarpour, M., Kavianinia, I. & Brimble, M. A. Thia-Michael addition: the route to promising opportunities for fast and cysteine-specific modification. *Organic & Biomolecular Chemistry* **21,** 3057–3072 (2023).

54. Fowkes, F. M., Dwight, D. W., Cole, D. A. & Huang, T. C. Acid-base properties of glass surfaces. *Journal of Non-Crystalline Solids* **120,** 47–60 (1990).

55. Krivoshiev, B. V., Beemster, G. T., Sprangers, K., Blust, R. & Husson, S. J. A toxicogenomics approach to screen chlorinated flame retardants tris (2-chloroethyl) phosphate and tris (2-chloroisopropyl) phosphate for potential health effects. *Journal of Applied Toxicology* **38,** 459–470 (2018).

56. Ostrerova, N. *et al.* α-Synuclein shares physical and functional homology with 14-3-3 proteins. *Journal of Neuroscience* **19,** 5782–5791 (1999).

57. Williams, D. M. *et al.* The amyloid fibril-forming β-sheet regions of amyloid β and α-synuclein preferentially interact with the molecular chaperone 14-3-3ζ. *Molecules* **26,** 6120 (2021).

58. Hochmair, J. *et al.* 14-3-3 binding regulates Tau assembly and microtubule association. *BioRxiv,* 2024–03 (2024).

59. Obsilova, V. & Obsil, T. Structural insights into the functional roles of 14-3-3 proteins. *Frontiers in molecular biosciences* **9,** 1016071 (2022).

60. Loureiro, J. A. *et al.* (De) stabilization of alpha-synuclein fibrillary aggregation by charged and uncharged surfactants. *International journal of molecular sciences* **22,** 12509 (2021).

61. Jha, N. N. *et al.* Complexation of NAC-derived peptide ligands with the C-terminus of α-synuclein accelerates its aggregation. *Biochemistry* **57,** 791–804 (2018).

62. Tuttle, M. D. *et al.* Solid-state NMR structure of a pathogenic fibril of full-length human α-synuclein. *Nature structural & molecular biology* **23,** 409–415 (2016).

63. Düster, R., Kaltheuner, I. H., Schmitz, M. & Geyer, M. 1, 6-Hexanediol, commonly used to dissolve liquid–liquid phase separated condensates, directly impairs kinase and phosphatase activities. *Journal of Biological Chemistry* **296** (2021).

64. Wu, Q. Development of chemical tool compounds for 14-3-3 PPIs: stabilizers and crosslinkers (2025).

65. Heesink, G. *et al.* Exploring Intra-and Inter-Regional Interactions in the IDP α-Synuclein Using smFRET and MD Simulations. *Biomacromolecules* **24,** 3680–3688 (2023).

66. Semmeq, A., Del Galdo, S., Chiarini, M., Daidone, I. & Casieri, C. Macromolecular vs molecular crowding in aqueous solutions: A comparative study of PEG400 and ethylene glycol. *Journal of Molecular Liquids* **394,** 123713 (2024).